

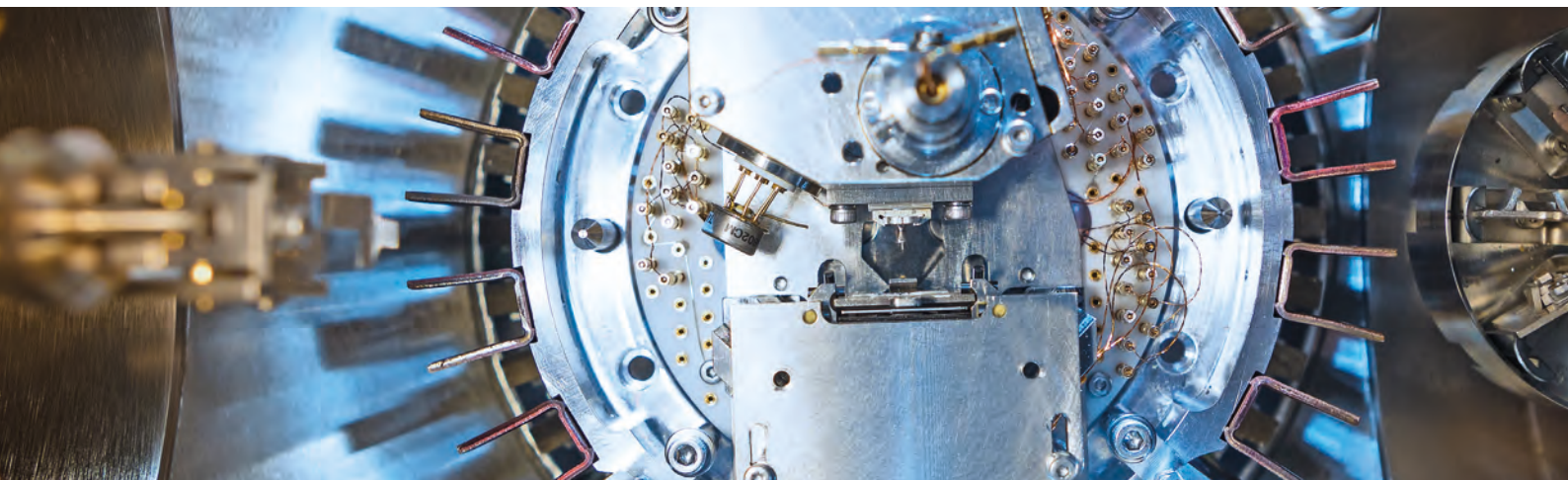
Jahresbericht Annual Report

2019



Leibniz-Institut
für Festkörper- und
Werkstoffforschung
Dresden

Jahresbericht Annual Report 2019



Leibniz-Institut
für Festkörper- und
Werkstoffforschung
Dresden

Impressum Imprint

Herausgeber/ Publisher

Leibniz-Institut für Festkörper- und
Werkstoffforschung Dresden
Vorstand/ Executive Board:
Prof. Dr. Bernd Büchner
Dr. Doreen Kirmse

Helmholtzstraße 20
01069 Dresden

www.ifw-dresden.de

Redaktion/Editing

Satz/Layout

Patricia Bäuchler

Druck/Print

ARNOLD group, Großbeeren

Fotos/Photos

Alle IFW, wenn nicht anders angegeben.
All IFW, unless otherwise indicated.

Dresden, Januar 2020

Liebe Leserinnen und Leser,

wir freuen uns sehr, Ihnen unseren Jahresbericht 2019 zu präsentieren. Er wartet mit einigen Änderungen auf, mit denen wir künftig ein breiteres Publikum ansprechen wollen, ohne den wissenschaftlichen Tiefgang aufzugeben. Wohl wissend, dass Quantenphysik, Materialchemie und Nanotechnologie sehr komplexe Themen sind, hoffen wir, dass Sie das neue Erscheinungsbild einlädt, sich näher mit dem IFW Dresden und seinen neuesten Forschungsergebnissen zu befassen. Das IFW war auch im Jahr 2019 sehr erfolgreich, so dass hier nur einige Highlights vorgestellt werden können. Wir wünschen eine spannende Lektüre und danken allen Partnern und Unterstützern.

Herzlichst / With best wishes



Prof. Dr. Bernd Büchner, Wissenschaftlicher Direktor (links) und Dr. Doreen Kirmse, Administrative Direktorin (rechts). Foto: Jürgen Lösel
Prof. Dr. Bernd Büchner, Scientific Director (left) and Dr. Doreen Kirmse, Administrative Director (right). Photo: Jürgen Lösel



Dear readers,

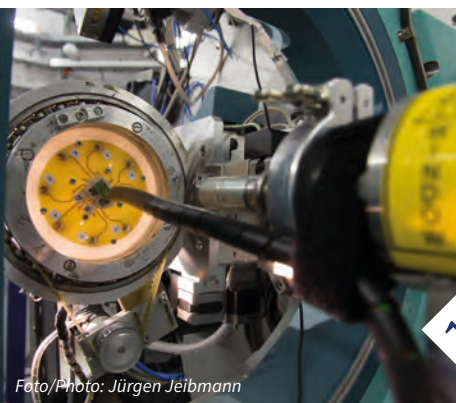
we are very pleased to present you our Annual Report 2019. It comes up with some changes and a new optical appearance. These aim for addressing a wider audience, without giving up the scientific depth. Knowing well that quantum physics, materials chemistry and nanotechnology are very complex topics, we hope very much that you feel invited to explore the IFW Dresden and its latest research results. The IFW was very productive in 2019, so only a few highlights can be presented in the scope of this report. The success of our work is not least the result of reliable funding and intensive cooperation with many partners. We would like to use this opportunity to sincerely thank you for this.

Inhalt Contents

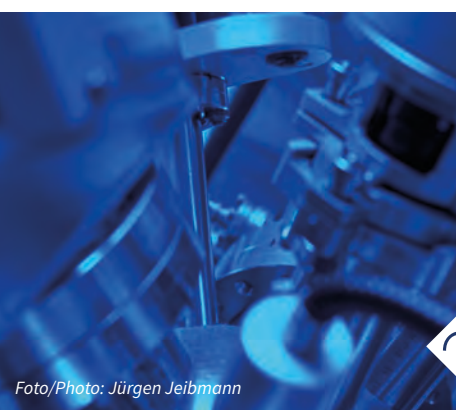
- 6 **Jahresrückblick 2019**
Review 2019
- 12 **Unser Forschungsprogramm**
Our Research Program
- 14 **Schwerpunkt 2019: Wissenschaftlicher Nachwuchs**
Focus 2019: Junior Research Groups
- 16 **Forschungsgebiet 1: Funktions-Quanten-Materialien**
Research Area 1: Functional Quantum Materials
- 18 *Metamagnetic Textures*
- 22 *Energy harvesting near room temperature using a thermomagnetic generator with pretzel-like magnetic field topology*
- 26 *Structure-property relationship of Co_2MnSi thin films in response to He^+ -irradiation*
- 30 **Forschungsgebiet 2: Funktion durch Nanoskaligkeit**
Research Area 2: Function through size
- 32 *Medical imaging of micromotors through scattering tissues*
- 36 *3D self-assembly for high performance shapeable microelectronic origami*
- 40 *Thermoelectric properties of recycled silicon sawing waste*



14



16

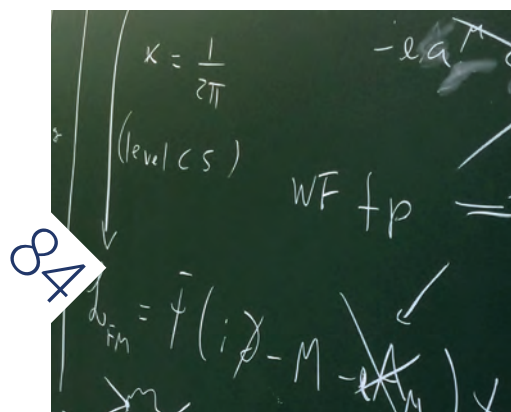
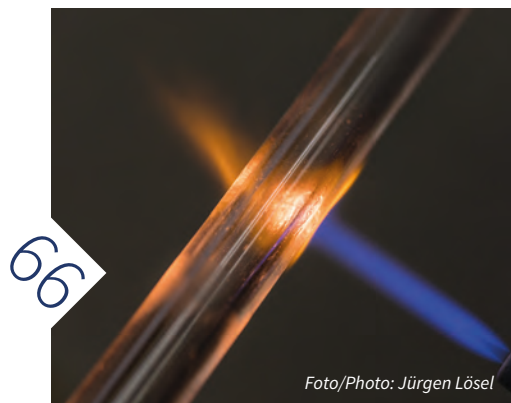
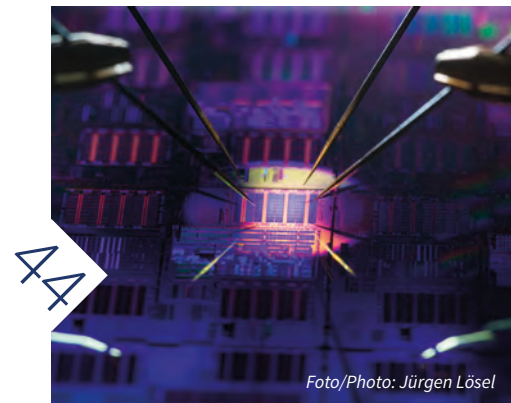


30

Foto/Photo: Jürgen Jeibmann

Foto/Photo: Jürgen Jeibmann

- 44 **Forschungsgebiet 3: Quantenphänomene im Nanomaßstab**
Research Area 3: Quantum Effects at the Nanoscale
- 46 *Entanglement swapping with semiconductor-generated photons violates Bell's inequality*
- 50 *Nernst Effect in Quantum Materials*
- 54 *Dual topology in jacutingaite Pt_2HgSe_3*
- 58 *Layered α -TiCl₃: Microsheets on Substrates for Ethylene Polymerization with Enhanced Activity*
- 62 *First intrinsic magnetic topological insulator*
- 66 **Forschungsgebiet 4: Vom Material zum Produkt**
Research Area 4: Towards Products
- 68 *Manipulation of complex biological fluids with microacoustic waves*
- 72 *Superconducting magnetic bearings for turbo ring spinning applications*
- 76 *Bioabsorbable Fe-Mn-based alloys for medical applications*
- 80 *Novel anti-perovskites (Li_2M)SO as bi-functional cathodes for Lithium-ion batteries*
- 84 **Zahlen und Fakten**
Facts and Figures
- 96 **Organigramm**
Organization Chart



Jahresrückblick 2019

Das Jahr 2019 war ein arbeitsreiches und produktives Jahr. Es war schon von der Vorbereitung auf die Leibniz-Evaluation im Jahr 2021 geprägt und brachte neue strategische Maßnahmen, Personalentscheidungen und Programmfokussierungen mit sich.

Das IFW ist Teil des neuen Exzellenzclusters „Complexity and Topology in Quantum Matter“ an der TU Dresden und der Universität Würzburg (ct.qmat), das im Januar 2019 an den Start gegangen ist. Im Fokus steht die fundamentale Erforschung von topologischen Quantenmaterialien und ihr enormes Anwendungspotential. Unser großes Engagement in diesem Cluster stärkt die strategische Position des IFW, sowohl regional als auch international. Für das geplante gemeinsame Nanomembrane-Lab mit der TU Dresden entsteht auch am IFW zusätzlicher Platzbedarf, der im bestehenden Gebäude nicht geschaffen werden kann. Im Sommer 2019 haben wir deshalb einen Neubau beantragt, der in den nächsten Jahren in fußläufiger Entfernung vom Hauptgebäude entstehen könnte. Wir bedanken uns für die Unterstützung in dieser Angelegenheit durch unsere Gremien, das Ministerium und die Landeshauptstadt und freuen uns auf eine positive Entscheidung.

Im März 2019 kamen alle verantwortlichen WissenschaftlerInnen des IFW zur jährlich stattfindenden Programm Klausur zusammen, um ihre jüngsten Ergebnisse und weiteren Pläne zu diskutieren. Auf diese Weise entsteht das IFW-Forschungsprogramm, dessen gemeinsames Fundament die Untersuchung noch unerforschter Eigenschaften neuartiger Materialien ist, mit dem Ziel, neue Funktionen und Anwendungen zu etablieren. Mit den drei Säulen *Quantum – Nano – Funktion* bietet das IFW-Forschungsprogramm einen bewährten Rahmen für interne Vernetzung, flexible Projekte und strategische Justierungen. Als neue strategische Maßnahme zur Verbesserung der organisationsübergreifenden Zusammenarbeit wurden 2019

Review 2019

Looking back to 2019, it was a busy and productive year. It was already marked by the preparation for the Leibniz Evaluation in 2021, including new strategic measures, personnel decisions and program focusing.

The IFW is part of the new Cluster of Excellence - Complexity and Topology in Quantum Matter at TU Dresden and University of Würzburg (ct.qmat) which has been established in January 2019. It is a unique research platform for comprehensive studies of the fundamental physics of topological quantum materials and their vast application potential. The strong and broad involvement of IFW in the ct.qmat cluster strengthen our strategic position in the scientific landscape both locally and internationally. At the same time, it creates a need for additional space, especially for the IFW part of a joint nanomembrane laboratory. In summer 2019 we therefore applied for a new building to be built within walking distance of the main building. We are very happy to get strong support in this matter from both Boards, the ministry and the municipal administration and look forward to a positive decision.

Once a year, all responsible Scientists of IFW meet for a three-day Program retreat and discuss their recent results and further plans. The IFW Research Program with the three pillars of *Quantum – Nano – Function* provides a proven framework for strategic discussions. It is well focused on the investigation of yet unexplored properties of novel materials with the aim to establish new functionalities and applications. At the same time it is flexible enough to include new developments and upcoming topics. In 2019,



vier IFW-Projekte auf den Weg gebracht:

- (1) *X-Stream TEM* mit Schwerpunkt auf neuen Modulations- und Lock-In-Techniken zur Verbesserung des Phasenkontrasts und zur Rauschreduzierung in der Transmissionselektronenmikroskopie.
- (2) *Sensoren für Hochtemperaturanwendungen*. Ziel ist es, mikrostrukturierte drahtlose Bauelemente für Hochtemperaturanwendungen zu entwickeln.
- (3) *SmartBio Stent* bringt unsere Expertisen in den Bereichen Implantatmaterialien, Oberflächendesign und Zellsortierung zusammen.
- (4) *Maschinelles Lernen für funktionale Quantenmaterialien*. Das Projekt kombiniert berechnete und gemessene Eigenschaften mit Methoden der künstlichen Intelligenz.

we introduced four IFW projects as a new strategic measure to enhance the cross-organizational cooperation. These are:

- (1) *X-Stream TEM* with a focus on new modulation and lock-in techniques to improve phase contrast and reduce noise in Transision Electron Microscopy.
- (2) *Sensor devices for high temperature applications*. The aim is to develop microstructured wireless sensor devices for high temperature applications.
- (3) *SmartBio Stent* combines experiences in materials development for biomedical applications, including surfaces design, implant materials and cell sorting.
- (4) *Machine Learning for Functional Quantum Materials*. The project combines calculated and measured properties with methods of artificial intelligence.

Das IFW ist auch regelmäßig ein Ort für wissenschaftliche Veranstaltungen. Im Juni 2019 tagte die Gemeinsame Wissenschaftskonferenz in unserem Hörsaal.
Foto: Hans-Günther Lindenkreuz

The IFW is also a regular venue for scientific events. In June 2019 the Gemeinsame Wissenschaftskonferenz took place in our lecture hall. Photo: Hans-Günther Lindenkreuz



Ein Indikator für die Leistungs- und Wettbewerbsfähigkeit des IFW ist die Einwerbung von Drittmittelprojekten. In dieser Hinsicht war das IFW 2019 sehr erfolgreich. Insbesondere ist hier die Bewilligung von drei neuen ERC Grants hervorzuheben: ein Advanced Grant für Prof. Oliver Schmidt und ein ERC Starting Grant für Dr. Mariana Medina-Sanchez, beide auf dem Gebiet der Mikrorobotik für biomedizinische Anwendungen (Seite 32), sowie ein ERC Consolidator Grant für Dr. Gabi Schierning. Des Weiteren war das IFW 2019 im europäischen Marie-Sklodowska-Curie-Programm für Innovative Training Networks (ITN) mit zwei Anträgen erfolgreich. Im neuen ITN BIOREMIA zu bioresistenten Implantatmaterialien übernimmt Prof. Dr. Mariana Calin vom IFW die Koordinatorenrolle. Darüber hinaus sind wir Teil des neuen ITN BeMAGIC, das sich mit energieeffizienten magnetoelektrischen Nanomaterialien beschäftigt wird. Das IFW ist weiterhin mit mehreren Teilprojekten im Sonderforschungsbereich „Korrelierter Magnetismus: Von der Frustration zur Topologie“ (SFB 1143) beteiligt, der 2019 in eine neue Förderperiode gestartet ist.

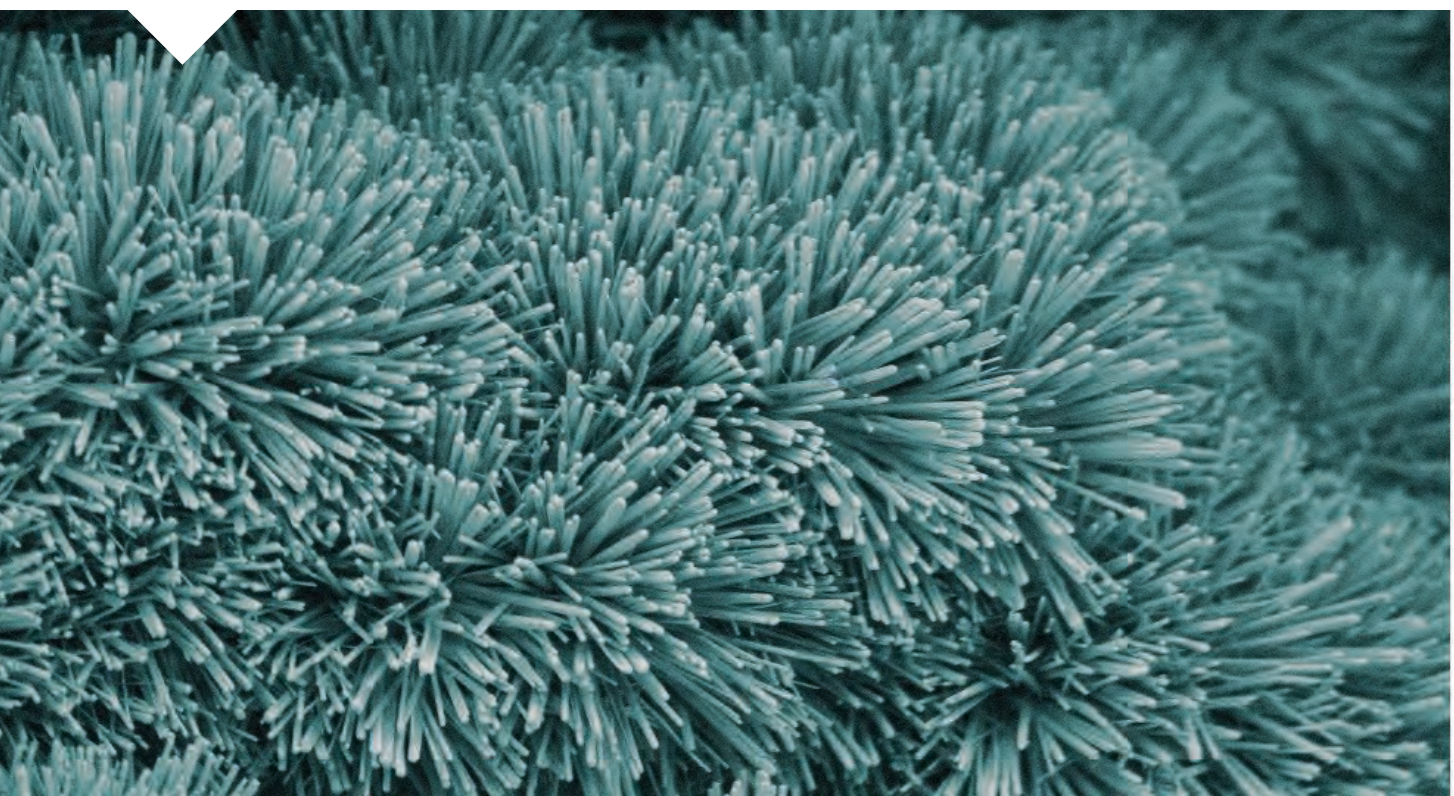
Das IFW koordiniert zwei DFG-Schwerpunktprogramme, eines zu Hochtemperatursupraleitung in Eisenpniktiden (SPP 1458) und eines zu Kalorien-

An important measure for the quality and competitiveness of IFW is the success of third party funding proposals in its core fields. In this respect the IFW was very successful in 2019. A big achievement was the approval of three new ERC Grants for IFW scientists: the ERC Advanced Grant of Prof. Oliver Schmidt and of the ERC Starting Grant of Dr. Mariana Medina-Sanchez, both in the field of microrobotics for biomedical applications (page 32), and the ERC consolidator Grant for Dr. Gabi Schierning. In addition, the IFW was successful in the 2019 call for Marie Skłodowska Curie Actions – Innovative Training Networks (ITN) with the approval of two proposals. The ITN BIOREMIA on resistant materials for hard tissue Implant Applications (BIOREMIA) will be coordinated by Prof. Dr. Mariana Calin from IFW. Further, we are part of the new ITN BeMAGIC on energy-efficient magnetolectric nanomaterials.

The IFW is strongly involved in the Collaborative Research Centre „Correlated Magnetism: From Frustration to Topology“ (SFB 1143) which started in a new funding period in 2019. It consists of 19 subprojects four of them based at IFW. In 2019, the IFW continues the strong engagement in DFG Priority Programs. The IFW coordinates two DFG Priority Programs, one on high temperature superconductivity in Iron

Hydroxylapatit auf poröser Titan-Niob-Legierung - European Training Network BIOREMIA.

Electrodeposited hydroxyapatite on porous Titan Niobium alloy - European Training Network BIOREMIA.



effekten in ferroischen Materialien (SPP 1599). An weiteren fünf Schwerpunktprogrammen beteiligen wir uns mit mehreren Projekten. Auch innerhalb der Leibniz-Gemeinschaft gibt es wettbewerblich vergebene Fördermittel. Im Januar 2019 hat Dr. Oleg Janson am IFW eine Leibniz-Nachwuchsgruppe zu korrelierten Materialien aus ersten Prinzipien ins Leben gerufen. Es wird für fünf Jahre von der Leibniz-Gemeinschaft mitfinanziert. Ebenfalls im Jahr 2019 wurde ein weiterer Vorschlag des IFW für den Leibniz-Wettbewerb bewilligt: Wir erhalten Mittel für die Realisierung des Leibniz-Transferprojekt MicroRes, um einen produktnahen Demonstrator für tragbare Miniaturresonatoren im Mikromaßstab für Kern- und Elektronenspinresonanzspektroskopie zu entwickeln.

Viel Energie haben wir 2019 in zwei Berufungsverfahren aufgewendet. Eines davon konnte erfolgreich zu Ende gebracht werden und hat zur Erhöhung des Frauenanteils in wissenschaftlichen Führungspositionen geführt. In einem sehr schnellen und kooperativen Verfahren mit der TU Bergakademie Freiberg wurde Prof. Dr. Julia Hufenbach als Professorin für Materialfunktionalisierung berufen. Gleichzeitig wird sie im IFW eine Forschungsgruppe leiten. Für das IFW-Institut für Komplexe Materialien werden aktuell neue Strukturen geschaffen.

Auch 2019 war das IFW wieder sehr engagiert bei der Organisation von Workshops und Konferenzen. Die größte Veranstaltung dieser Art war die „European Conference on Applications of Surface and Interface Analysis“ (ECASIA '19) im September in Dresden mit etwa 375 Teilnehmern. Darüber hinaus organisierten wir zwei internationale Workshops, einen im März zum Thema „Quantendynamik, Transport und exotische Ordnungen“ und einen im Mai gemeinsam mit dem Weizmann-Institut zum Thema „Topologie trifft Materialien“. Bereits zum fünften Mal veranstaltete das IFW eine Internationale Sommerschule für Spektroelektrochemie. Aufgrund der besonderen Kompetenzen und apparativen Möglichkeiten des IFW auf diesem Gebiet ist diese Veranstaltung sehr nachgefragt. Ein weiterer Höhepunkt war der Besuch des Präsidenten des Europäischen Forschungsrates (ERC), Prof. Jean-Pierre Bourguignon, im Frühsommer, als er sich in unserem Haus mit ERC-Stipendiaten aus Sachsen und Vertretern der Hochschulen und

pnictides (SPP 1458) and one on caloric effects in ferroic materials (SPP 1599). In further five priority programs we participate with several projects.

Another field of competition and source of funding is the Leibniz Association. In January 2019, Dr. Oleg Janson launched a Leibniz Junior Research Group on correlated materials from first principles. It will be co-funded by the Leibniz Association for five years. Also in 2019, a further IFW proposal in the Leibniz competition has been approved: We get funding for the Leibniz Transfer Project MicroRes to develop a close-to-product demonstrator of a miniature portable Micro-scale resonators for nuclear and electron spin resonance spectroscopies.

Two appointment procedures kept us busy in 2019. Our engagement for more female leadership in science was successful in one of them. In a very quick and cooperative procedure Prof. Dr. Julia Hufenbach has been appointed as temporary professor for materials functionalization at the TU Bergakademie Freiberg. For the IFW Institute for Complex Materials we are currently defining new structures.

The IFW was also very active in organizing workshops and conferences. The largest one in 2019 was the European Conference on Applications of Surface and Interface Analysis (ECASIA '19) in September in Dresden with about 375 participants. Further, we organized two international workshops, one in March on “Quantum Dynamics, Transport, and Exotic Orders“ and one in May on “Topology meets materials“ together with the Weizmann Institute. The outstanding competencies and facilities in the field of electrochemistry is the base for the 5th Summer School on Spectroelectrochemistry which we offer every other year for one week in September. Another highlight in 2019 was the visit of the President of the European Research Council (ERC), Prof. Jean-Pierre Bourguignon in June at IFW to meet with ERC grantees from Saxony. During the Materials Week in September in Dresden we presented some of our application-related topics such as thermoelectrics, selective Laser melting and surface acoustic waves' technology.

Essentially publicly funded, we are obliged to make our research results public. In 2019, IFW scientists have published about 399 articles in scientific journals and conference proceedings. 185 invited talks

Ministerien traf. Im September 2019 fand in Dresden die Werkstoffwoche statt, zu der wir einige unserer anwendungsbezogenen Themen wie Thermoelektrik, selektives Laserschmelzen und Oberflächenwellen-Technologie präsentiert haben.

Als öffentlich finanzierte Forschungseinrichtung veröffentlichen wir unsere wissenschaftlichen Ergebnisse und stellen sie selbstverständlich in den Dienst der Gesellschaft. Im Jahr 2019 haben IFW-WissenschaftlerInnen 399 Artikel in wissenschaftlichen Fachzeitschriften und Tagungsbänden veröffentlicht. IFW-WissenschaftlerInnen waren 185 mal zu Vorträgen auf Konferenzen, Workshops, Seminaren und anderen Anlässen auf der ganzen Welt eingeladen. Wir haben für fünf neue Erfindungen Patentanmeldungen eingereicht und 21 nationale und internationale Patente erteilt bekommen.

Neben dieser Kommunikation im wissenschaftlichen Bereich und mit den direkten Anwendern machen wir unsere Arbeit auch der breiten Öffentlichkeit zugänglich. Ein besonderes Anliegen ist es auch, junge Menschen für ein Studium der Natur- oder Ingenieurwissenschaften zu begeistern. Hierfür engagieren wir uns im Dresdner Netzwerk von Hochschulen

were presented by IFW scientists at conferences, workshops, seminars and other occasions around the world. In 2019, we received 21 national and international granted patents and five priority patent applications were filed for new inventions.

Apart from these scientific communications the IFW continued its large efforts to make scientific work accessible for the general public and to inspire young people to study science or engineering. The IFW has been engaged in joint events of the Dresden network of universities and research institutions. The most prominent event in this respect is the Dresden Long Night of Sciences which takes place once a year before the summer vacancies. In 2019, we again offered an ample program which attracted about 3500 visitors. Another activity of the network is the event "Junior-doctor". The IFW contributed not only with an experimental lecture for about 80 kids on low temperature physics in January but also with hands-on workshops for kids in the cleanroom.

Besides these big events we organized almost weekly lab-tours for various visitor groups, from school classes through official representatives to guests of foreign organizations.



und Forschungseinrichtungen. Im Verbund mit den Dresdner Partnern organisieren wir die Dresdner Lange Nacht der Wissenschaften, die einmal im Jahr vor den Sommerferien stattfindet. Das umfangreiche Programm des IFW hat 2019 ca. 3500 Besucher angezogen. Eine weitere Aktivität des Netzwerks ist die Veranstaltung „Juniordoktor“, an dem sich das IFW mit einem Experimentalvortrag für etwa 80 Kinder zur Physik bei tiefen Temperaturen und mit Workshops im Reinraum beteiligte. Neben diesen großen Veranstaltungen organisierten wir fast wöchentlich Laborbesichtigungen für verschiedene Besuchergruppen, von Schulklassen über Rahmenprogramme für Tagungen bis hin zu Gästen ausländischer Organisationen.

Vieles, was wir 2019 angestoßen haben, wird uns auch 2020 weiter beschäftigen: zum Beispiel die Neubaupläne, das Vorhaben der strategischen Erweiterung, die Vorbereitung der Leibniz-Evaluierung 2021 sowie die Besetzung einer vakanten Direktorenstelle. Wir sind optimistisch, dass wir diese Herausforderungen meistern werden, nicht zuletzt durch die Mitwirkung der Belegschaft und durch die Unterstützung von Kooperationspartnern, Gremien und Förderern. Hierfür möchten wir uns nochmals herzlich bedanken.

Much of what we initiated in 2019 will continue to occupy us in 2020: for example, the plans for the new building and the strategic expansion, the preparation of the Leibniz Evaluation in 2021 and the filling of a vacant director's position. We are optimistic that we will master these challenges, not least because we can rely on engaged staff as well as on the support of co-operation partners, boards and sponsors. We would like to cordially thank you for this.



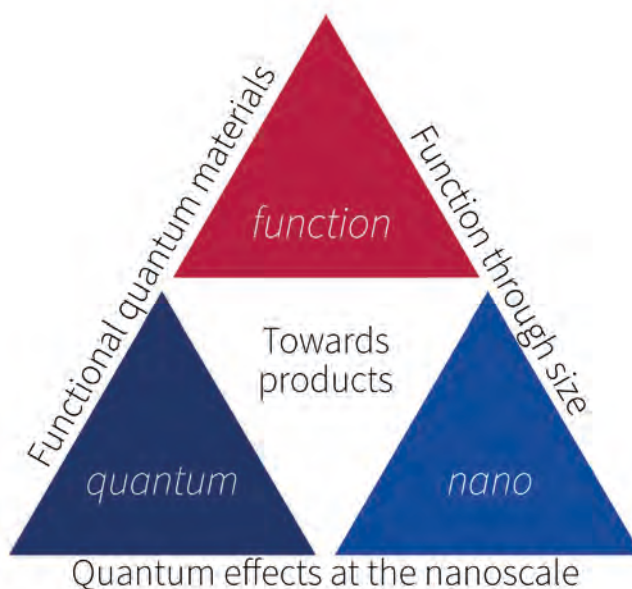
Unser Forschungsprogramm

Unser Forschungsprogramm bringt die fünf IFW-Institute in einer Matrixstruktur zusammen. In vier Forschungsgebieten verbindet es die Kompetenzen Theorie, experimentelle Physik, Chemie, Charakterisierung und Materialentwicklung der einzelnen Institute.

Bei aller Breite und Interdisziplinarität gilt für alle Forschungsaktivitäten des IFW, dass sich die WissenschaftlerInnen mit noch unerforschten Eigenschaften neuer Materialien beschäftigen, mit dem Ziel, neue Funktionalitäten und Anwendungen zu erschließen.

QUANTUM - NANO - FUNKTION

Die Verknüpfung der drei Felder Quantenmaterialien - Nanoskalige Materialien - Funktionsmaterialien ist das Alleinstellungsmerkmal des IFW. Entlang der Verbindungen dieser Felder haben wir drei Forschungsgebiete definiert, die wir strategisch von den Grundlagen bis zu Funktionalitäten bearbeiten. Das vierte Forschungsgebiet in der Mitte des Dreiecks beinhaltet Forschung zu Materialien und Systemen, die bereits Anwendungsreife erreicht haben.



Our Research Program

Our Research Program brings together the five IFW Institutes. It combines theory, experiments, synthesis, characterization and materials and device development in four Research Areas.

Despite its diversity and interdisciplinarity, all IFW research activities have in common that scientists are investigating still unexplored properties of matter with the aim of developing new functionalities and applications.

QUANTUM - NANO - FUNCTION

The junction of the three fields Quantum matter – Nanoscale materials – Functional materials is the unique feature of the IFW. Along the junctions of these fields we have defined three Research Areas where we cover the range from fundamentals to functionalities in a strategic manner.

The fourth Research Area binds together materials science research that is already at the threshold to prototypes or products.

Das Forschungsdreieck zeigt die Verknüpfung unserer Forschungsfelder Quantenmaterialien - Nanoskalige Materialien - Funktionsmaterialien. Aus den Verbindungen dieser Felder ergeben sich unsere Forschungsgebiete. Das vierte Forschungsgebiet in der Mitte des Dreiecks beinhaltet Forschungsthemen mit Bezug zur Anwendung.

The research triangle illustrates the junction of our research fields Quantum matter - Nanoscale materials - Functional materials. Our Research Areas result from the junctions between these fields. The fourth Research Area in the middle of the triangle contains research topics related to application.

Fünf Institute des IFW Five IFW Institutes

Institut für Festkörperforschung - Institute for Solid State Research (IFF)

Director: Prof. Dr. B. Büchner

Das IFF beschäftigt sich mit materialorientierter Festkörperforschung mit den besonderen Schwerpunkten Quantenmaterialien und nanoskaligen Substanzen.

The IFF does research in the field of material-oriented experimental solid state physics with a special focus on quantum materials and nanoscale substances.

Institut für Metallische Werkstoffe - Institute for Metallic Materials (IMW)

Director: Prof. Dr. K. Nielsch

Die Themen des IMW sind thermoelektrische, magnetische und supraleitende Materialien, funktionelle Dünnschichten sowie Metallphysik.

Main research topics of IMW are thermoelectric, magnetic and superconducting materials, functional thin films and metal physics.

Institut für Komplexe Materialien - Institute for Complex Materials (IKM)

Director: Prof. Dr. B. Büchner (temp.)

Die Forschungsaktivitäten des IKM fokussieren sich auf Legierungsdesign und Prozesstechnologien, Chemie funktionaler Materialien sowie Strukturanalytik.

The research activities of the IKM focus on alloy design and processing, chemistry of functional materials and structural analysis.

Institut für Integrative Nanowissenschaften - Institute for Integrative Nanosciences (IIN)

Director: Prof. Dr. Prof. h.c. O. G. Schmidt

Das IIN beschäftigt sich mit modernen Themen der Nanowissenschaften von Photonik über flexible Elektronik bis hin zu Mikro-/Nano-Robotern.

The IIN deals with a variety of modern nanoscience topics from photonics to flexible electronics to micro/nano-robots.

Institut für Theoretische Festkörperphysik - Institute for Theoretical Solid State Physics (ITF)

Director: Prof. Dr. J. van den Brink

Die Forschung am ITF konzentriert sich auf die theoretischen Aspekte der Physik der kondensierten Materie und der Materialwissenschaften.

The ITF focusses on theoretical aspects of condensed matter physics and materials science.

Schwerpunkt 2019: Wissenschaftlicher Nachwuchs

Die Förderung des wissenschaftlichen Nachwuchses ist eine satzungsgemäße Aufgabe des IFW Dresden, der wir uns mit großem Einsatz und vorzeigbaren Erfolgen widmen. Sie beginnt bei der Vergabe von Themen für studentische Arbeiten, geht über die Betreuung und Beschäftigung von DoktorandInnen bis hin zur Förderung der frühen wissenschaftlichen Selbständigkeit als PostdoktorandIn und NachwuchsgruppenleiterIn. Das IFW bietet StudentInnen die Möglichkeit, in Forschungsprojekten mitzuwirken und ihre Ergebnisse für Abschlussarbeiten zu nutzen. 2019 wurden im IFW 22 abgeschlossene Master- bzw. Diplomarbeiten betreut.

DoktorandInnen machen ca. ein Drittel aller am IFW tätigen WissenschaftlerInnen, einschließlich Stipendiaten und Gästen, aus. Nahezu jedes Drittmittelprojekt bindet DoktorandInnen ein und trägt so auch zur Nachwuchsförderung bei. Die durchschnittliche Anzahl der am IFW beschäftigten bzw. betreuten DoktorandInnen beträgt 140. Im Jahr 2019 wurden 20

Focus 2019: Junior Research Groups

The promotion of young scientists is a statutory task of the IFW Dresden, which we address with great dedication and remarkable success. This includes the assignment of topics for student graduation theses, the employment and intensive supervision of doctoral students and the promotion of early scientific independence as a postdoc and junior research group leader. The IFW offers students the opportunity to participate in research projects and to use their results in their graduation theses. In 2019, 22 master and diploma theses were supervised and completed at IFW.

Doctoral students account for about one third of all IFW researchers, including scholarship holders and guests. Almost every third-party funded project involves doctoral students and thus also contributes to the promotion of young researchers. The average number of doctoral students employed or supervised at the IFW is 140. In 2019, 20 PhD theses were successfully completed, five of which with the best possible grade summa cum laude.

Doktorandengruppe des Innovativen EU-Netzwerks BIOfilm-REsistant Materials for hard tissue Implant Applications (BIOREMIA).

PhD group of the EU-Network on BIOfilm-REsistant Materials for hard tissue Implant Applications (BIOREMIA).



Professorin Julia Kristin Hufenbach (rechts) mit Dr. Josephine Zeisig (links) im Gießlabor. Seit dem 1. November ist Frau Julia Kristin Hufenbach Professorin für Werkstofffunktionalisierung an der Technischen Universität Bergakademie Freiberg.
Foto: Jürgen Lösel

Professor Julia Kristin Hufenbach (right) with Dr. Josephine Zeisig (left) in the casting laboratory. Since November 1, Julia Kristin Hufenbach is professor for materials functionalization at the Technische Universität Bergakademie Freiberg.
Photo: Jürgen Lösel



Promotionen erfolgreich abgeschlossen, fünf davon mit dem bestmöglichen Prädikat *summa cum laude*. Neben der themenspezifischen Betreuung bietet das IFW den DoktorandenInnen zahlreiche Möglichkeiten, sich in Seminaren und Doktorandenklausuren im wissenschaftlichen Diskurs zu üben, an wissenschaftlichen Tagungen im In- und Ausland teilzunehmen, Methoden- und Managementkompetenzen sowie Soft-Skills zu erwerben. Dazu gehören die jährlich stattfindende IFW-Sommerschule sowie der alle zwei Jahre stattfindende Doktorandentag mit Angeboten zum wissenschaftlichen Schreiben, Projektmanagement und Medienkompetenz.

In den vergangenen Jahren hat das IFW viele Anstrengungen unternommen, besonders qualifizierten jungen WissenschaftlerInnen bereits früh Verantwortung für selbständige Nachwuchsgruppen zu übertragen. 2019 waren 11 der insgesamt 42 wissenschaftlichen Arbeitsgruppen bzw. Abteilungen selbständige Nachwuchsgruppen. Ein Großteil davon wird von Drittmitteln finanziert, die die NachwuchsgruppenleiterInnen selbst eingeworben haben. So gab es fünf ERC-Gruppen, eine Emmy-Noether-Gruppe und eine Leibniz Nachwuchsgruppe. Ein besonderer Erfolg, auch in Richtung Gleichstellung, war 2019 die Besetzung von zwei Professorenstellen mit jungen Wissenschaftlerinnen. Frau Prof. Dr. Isaeva wurde gemeinsam mit der TU Dresden auf eine Juniorprofessur berufen und leitet am IFW eine Nachwuchsgruppe. Frau Prof. Dr. Hufenbach wurde gemeinsam mit der TU Bergakademie Freiberg auf eine befristete Professur nach Thüringer Modell berufen und ist als Forschungsgruppenleiterin am IFW tätig.

2019 haben vier Nachwuchswissenschaftler am IFW einen Ruf auf eine Universitätsprofessur erhalten, was Zeugnis unserer erfolgreichen Nachwuchsförderung ist.

In addition to individual scientific support, the IFW offers numerous opportunities for doctoral students to practice the academic discourse in seminars and scientific workshops, to participate in scientific conferences in Germany and abroad, to acquire methodological and management skills as well as soft skills. These include the annual summer school for IFW doctoral students and the biennial IFW PhD Day with seminar offers for academic writing, project management and media literacy.

In the past few years, the IFW has made large efforts to establish independent junior research groups and to identify them in the organizational chart of the institute. High potential and qualified young scientists should be assigned responsibility already in an early stage of their career. In 2019, eleven of the 42 scientific working groups or departments were independent junior research groups. A large part of them is financed by third-party projects, which the junior research group leaders have raised themselves in a highly competitive manner. In 2019, five ERC groups, one Emmy Noether group and one Leibniz junior research group has been active at IFW. A particular success, also in the sense of gender equality, was the appointment of two professorships with young female scientists in 2019. Prof. Isaeva was appointed to a junior professorship together with the TU Dresden and leads a junior research group at the IFW. Prof. Hufenbach was appointed to a temporary professorship together with the TU Bergakademie Freiberg in accordance with the Thuringian Model and is working as a research group leader at the IFW.

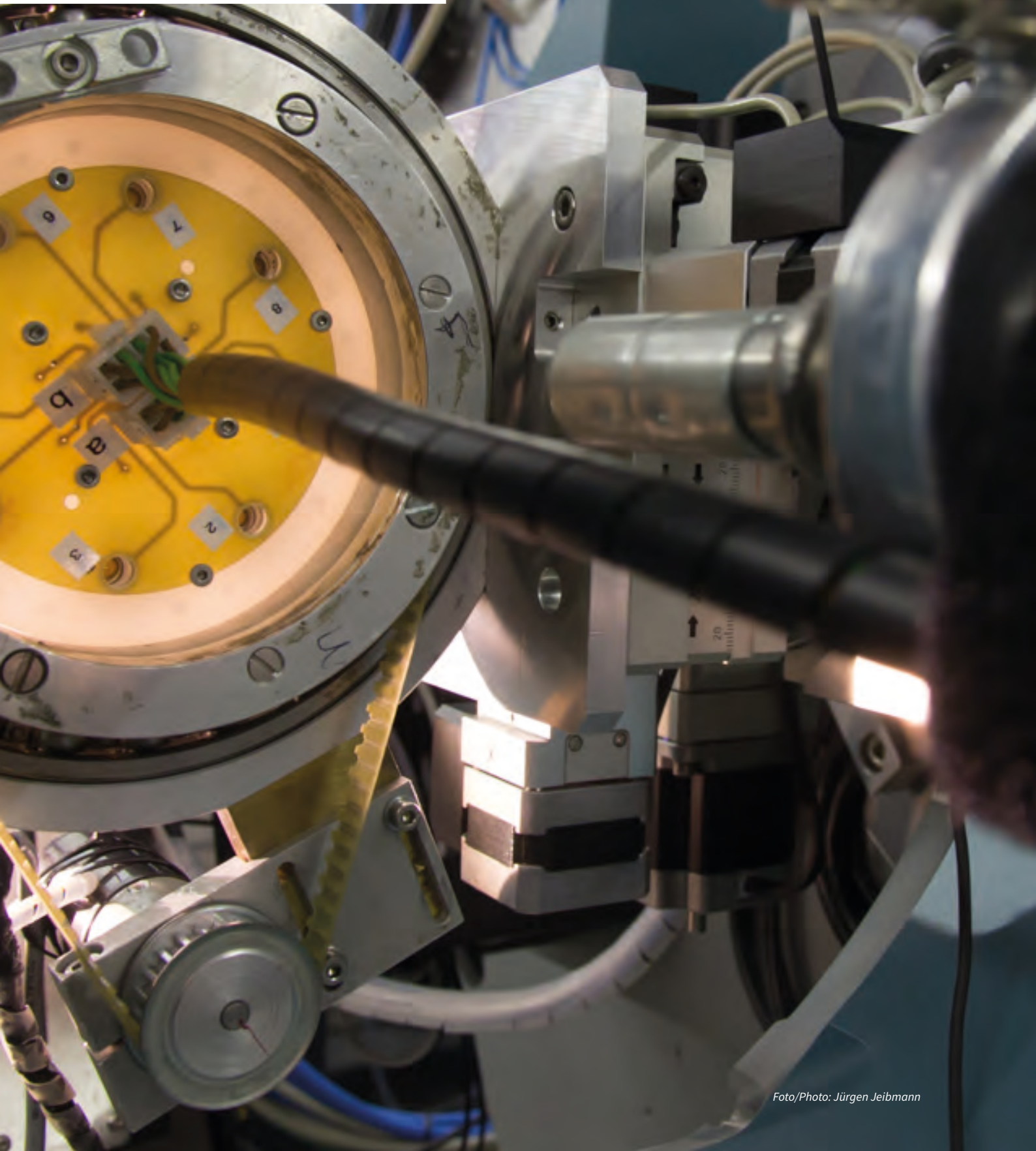
In 2019, four young scientist at IFW got a call on a professorship at a university, which is a nice proof successful promotion of young talents at IFW Dresden.

FORSCHUNGSGEBIET 1:

Funktions-Quanten-Materialien

RESEARCH AREA 1:

Functional Quantum Materials



Funktions-Quanten-Materialien

Im Forschungsgebiet 1 erforschen wir Materialien, deren elektronische Eigenschaften zu neuen Funktionalitäten mit interessantem Anwendungspotential führen können. Die physikalischen Eigenschaften manifestieren sich in einer Reihe von Materialklassen: in bestimmten Übergangsmetalloxiden, in molekularen Feststoffen und in intermetallischen Materialien. All diese Systeme weisen ein vielseitiges Zusammenspiel auf von lokalisierten und delokalisierten elektronischen Freiheitsgraden. Das unterscheidet diese Materialien sowohl praktisch als auch konzeptionell sehr deutlich von einfachen Metallen und Halbleitern mit gut verstandener elektronischer Struktur. Häufig führt das quantenmechanische Wechselspiel verschiedener elektronischer Freiheitsgrade zu anormalen Ladungstransporteigenschaften, beispielsweise aufgrund von Metall-Isolator-Übergängen, und zu außergewöhnlichen Ordnungsphänomenen wie unkonventionelle Formen der Supraleitung und Quantenmagnetismus. Hieraus resultierende und nutzbare Funktionalitäten sind z.B. große magnetokalorische Effekte, Hochtemperatursupraleitung, Magnetismus mit sehr starker Anisotropie und der Riesenmagnetowiderstand.

Functional Quantum Materials

Research Area 1 is focused on bulk materials in which a potential for applications emerges from their complex, quantum mechanical electronic properties. These physical material's properties manifest themselves in a number of material classes: in certain families of transition-metal oxides, in molecular solids and in a range of intermetallic materials. What sets these systems apart is that their valence and conduction electrons typically retain to some extent their atomic character, resulting in a rich interplay of localised and delocalised electronic degrees of freedom. This renders these materials both practically and conceptually very different from simple metals and semiconductors with well-understood itinerant quasi-particles. Often the quantum mechanical interplay between the localised and delocalised electronic degrees of freedom leads to anomalous charge transport properties, for instance due to the presence of metal-insulator transitions, and exceptional types of ordering phenomena, such as unconventional forms of superconductivity and quantum magnetism. Functionalities that arise from this are for instance large magnetocaloric effects, high temperature superconductivity, magnetism with very strong anisotropy and giant magnetoresistance.

Metamagnetic Textures

Ulrich K. Rößler, Dmitry A. Sokolov¹

Zusammenfassung

Ein neuartiger Typ eines magnetischen Zustands wurde in magnetischen Kristallen von $\text{Ca}_3\text{Ru}_2\text{O}_7$ gefunden. Diese Schichtkristalle besitzen einen einfachen antiferromagnetischen Grundzustand. In einem angelegten Feld und einem bestimmten Temperaturintervall wandelt sich diese antiferromagnetische Ordnung in eine äußerst komplexe Textur um, in der ferromagnetische und antiferromagnetische Konfigurationen über Längenskalen von wenigen zehn Nanometern ineinander verwoben sind. Theoretische Vorstellungen, die am IFW Dresden entwickelt wurden, haben zur Entdeckung und Erklärung dieser sogenannten metamagnetischen Textur geführt. Der Mechanismus zur Bildung gemischter Texturen aus zwei Ordnungstypen kann durch fundamentale Einsichten in ihre Symmetrien erklärt werden. Dies unterstreicht die Bedeutung unserer Entdeckung: die

metamagnetische Textur ist ein erstes Beispiel für eine weite Klasse von Systemen, wo ähnlich exotische, räumlich oszillierende Muster aus verschiedenen geordneten Zuständen existieren können.

Abstract

A novel type of magnetic state has been found in a magnetic crystal of $\text{Ca}_3\text{Ru}_2\text{O}_7$. This layered material has a simple antiferromagnetic ground-state. Under applied field and in a certain temperature range this antiferromagnetism transforms into a texture of unprecedented complexity, where ferromagnetic and antiferromagnetic configurations are interwoven on length scales of a few ten nanometers. Finding and understanding this so-called metamagnetic texture has been guided by theoretical concepts developed at IFW. The mechanism for forming mixed textures combining two types of order can be explained by fundamental symmetry considerations. This underlines the significance of our discovery: The metamagnetic texture is a first example for a vast class of systems, where similar exotic, spatially oscillating patterns between different orders states can exist.



Abb. 1: Im Inneren eines Kristalls mit metamagnetischer Textur. Ein Blick in Modulationsrichtung zeigt periodisch abwechselnd Abschnitte mit lokal antiferromagnetischer links-rechts Konfiguration und mit ferromagnetischer senkrechter Konfiguration der magnetischen Momente. Das angelegte magnetische Feld zeigt senkrecht aufwärts. Der Bildhintergrund ist ein Detektorbild des Kleinwinkel-Neutronendiffraktionsexperiments im metamagnetischen Zustand. Satelliten um das Zentrum signalisieren ferromagnetische Beiträge zu der magnetischen Modulation.

Fig. 1: Inside a crystal with a metamagnetic texture. Looking down the modulation direction, sections alternate periodically between local antiferromagnetic left-right configuration and ferromagnetic up-up direction of magnetic moments. The applied magnetic field is pointing in upwards direction. The background shows a detector image from the small-angle neutron diffraction experiment in the metamagnetic state. Satellite peaks around the center signal the presence of a ferromagnetic contribution to the magnetic modulation.

Simple ideas about magnetic order in crystals have a solid foundation. Ferromagnetic order sets in, if magnetic moments point all in one direction. If the crystal hosts several sublattices, moments can be anti-parallel or form even more complex spin configurations. If the total magnetic moment of the different lattices sums up to zero, then the material orders as an antiferromagnet, otherwise a ferrimagnetic state is found. These atomic patterns of ordered moments can be understood using fundamental principles. The magnetically ordered phases are distinct, because they break certain symmetries of the crystal, and the phases are separated by phase transitions at certain temperatures, pressures or external fields, where the qualitative properties of the material are drastically changed. While some rotations are able to map a paramagnetic crystal onto itself, these symmetries are lost in the ferromagnetic phase. In an antiferromagnet, the equivalence of different sublattices is broken. For a long time, some magnetic materials have been known where an antiferromagnetic ground state is transformed into a ferromagnetic configuration. These transformations can be driven by an applied magnetic field. These transitions usually are jump-like. The phenomenon is called metamagnetism, as it mediates between two opposing types of magnetic order – ferromagnetism and anti-ferromagnetism. Since Néel's explanations of antiferromagnetism and the invention of neutron scattering methods that are able to detect configurations of magnetic moments in crystals, a detailed understanding of such magnetic phase transitions has been achieved. The different phases in these classical magnetic systems are homogeneous, and therefore simple.

In our work, we show that much more complex types of ordering can exist giving rise to exotic behavior. In an antiferromagnet under an applied magnetic field, we find a static magnetic state, where the local spin configuration alternates on very small scales of a few ten nanometers between the antiferromagnetic and the ferromagnetic configuration. We call this state a metamagnetic texture, because it represents an inhomogeneous fabric of different interwoven magnetic orders. Its complexity is clear from the underlying symmetries. Such a texture combines different states and simultaneously breaks several of the symmetries of the paramagnetic crystal. The discovery has been achieved by a joint effort between theoretical work, performed at IFW Dresden, and experimental in-

vestigations guided by the Max Planck Institute for Chemical Physics of Solids and collaborations with several neutron scattering centers.

Research on ferromagnetic or other textures has been cultivated at IFW since the early prediction of skyrmion lattices and their properties [1]. The basic mechanism for the creation of these textures are chiral couplings between magnetic moments and their resulting twisted configurations. At present, chiral magnetic systems of this type are actively investigated by many groups worldwide, in part for fundamental interest, but also with a perspective of applications in spintronics [2]. At IFW Dresden, current research in this area pursues magnetic properties, behavior, and imaging of such chiral textures, both in experiment and theory [3,4].

These chiral ferromagnets illustrate a simple modification of a basic magnetic state into a texture. The ferromagnetic spin configuration is rotating as a spiral over larger lengths in space. A few antiferromagnets are known to display similar antiferromagnetic spirals. In a skyrmion lattice, the spiraling takes place in several spatial directions. Although skyrmion lattices are sometimes termed the most complex magnetic phases known, the local configuration of the magnetic moments is the simple parallel ferromagnetism. The novel metamagnetic textures add another layer of complexity, as they combine different local configurations of moments into one modulated state.

The metamagnetic texture has been detected by a concerted investigation on a magnetic oxide $\text{Ca}_3\text{Ru}_2\text{O}_7$, a perovskite-like bilayer structure. Its magnetic ground-state in zero field is antiferromagnetic. Bilayers of ruthenium atoms are ferromagnetically ordered. In the long c -axis direction, they stack alternately pointing up or down in a certain direction (Fig. 2). The metamagnetism of this material was known from a steep anomaly of the magnetization curves under applied field in certain temperature ranges (Fig. 3). The crystal structure of this material stands out, because it is polar. This means that $\text{Ca}_3\text{Ru}_2\text{O}_7$ has no inversion center and certain chiral couplings do exist which can cause twisted configurations of the magnetic moments. Relying on this information about the symmetries of the ground-state and of the lattice combined with the metamagnetic phenomenon, we set out on a search for the underlying magnetic structure. The work required high-quality single crystals of this complex oxide and detailed characteriza-

tion of its magnetic phase diagram with a multitude of methods. As the chiral couplings stem from the microscopic spin-orbit couplings, we also measured spin and orbital moments and used electron theoretical calculations to ascertain that these effects should be large in this magnetic system. The crucial technique used to reveal the metamagnetic texture then was neutron scattering in the small angle range. This technique is able to detect magnetic modulations on length scales above the atomic scale. A detailed investigation on $\text{Ca}_3\text{Ru}_2\text{O}_7$ in the range of the metamagnetic transition uncovered a unique type of modulation, which involves both the ferromagnetic and the antiferromagnetic order. It was also found that the modulation period of this texture depends remarkably on temperature. This indicates that it is forming under influence of several competing effects with differing temperature dependence. In the present experimental data, the qualitative picture of the metamagnetic texture was confirmed, as expected from the symmetry-based qualitative theory. However, the detailed anatomy of such a complex state is still a task for future research.

The insights into the magnetic phase diagram of this specific material can have wider consequences. The state found here violates some of the basic tenets about simple magnetic ordering and the underlying broken symmetries. While the symmetry method for

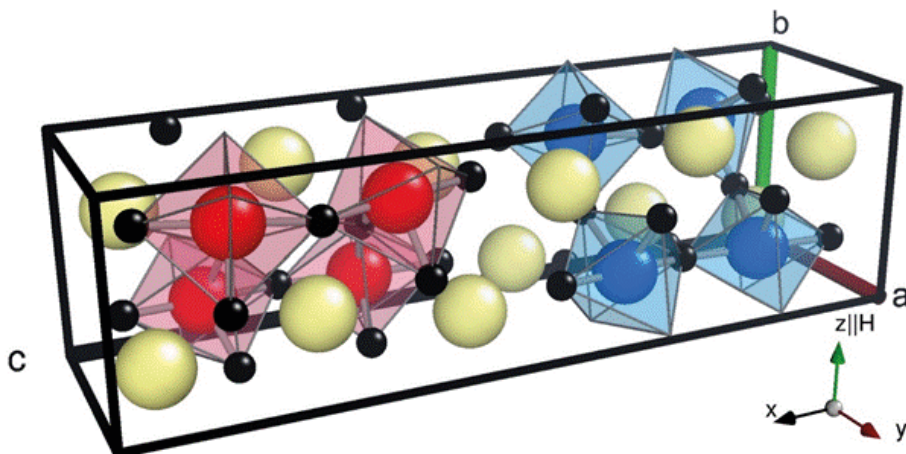
analysing ordered phases, known as Landau theory, allows to predict where to search for such exotic textures, their properties do not obey this theory for exactly this reason. That textures of ordered states are violating the criteria of the elementary Landau theory was described by Dzyaloshinskii in the 1960s. Chiral helimagnetic textures, therefore, now have been termed Dzyaloshinskii spirals or Dzyaloshinskii textures. They belong to a class of states where only one type of order is spatially twisted.

In our original publication on this metamagnetic texture [5], the term improper Dzyaloshinskii texture is proposed. This emphasizes that they are twisted textures of a mixed type, where different basic orders co-exist in one twisted configuration, here the ferromagnetic and antiferromagnetic arrangement of moments. The basic concepts for these states have been developed theoretically at IFW. They open a vast area of new possibilities to create patterns in magnetic materials, which typically should exist at the nanoscale. The underlying principles suggest that similar states can also exist in other ferroic materials, like ferroelectrics and ferroelastics, or even in materials with other lattice instabilities.

From a practical side, the approach taken to predict existence of the novel metamagnetic textures naturally can be extended to find other experimental realizations. Whole classes of non-centrosymmetric

Abb.2: Kristallstruktur des $\text{Ca}_3\text{Ru}_2\text{O}_7$. In der Einheitszelle sind die ferromagnetisch gekoppelten Ruthenium-Doppellagen durch rote und blaue Kugeln in ihren RuO_6 -Oktaedern dargestellt. Im magnetischen Grundzustand zeigen die magnetischen Momente der Doppellagen in antiparalleler Richtung.

Fig. 2: Crystal structure of $\text{Ca}_3\text{Ru}_2\text{O}_7$. In the unit cell, the two ferromagnetically coupled ruthenium bilayers are depicted by red and blue balls inside their RuO_6 -octahedra. In the magnetic ground-state the bilayer moments point in antiparallel directions.



antiferromagnets now are candidate materials, where applied fields can drive a metamagnetic transition into the ferromagnetic state. If the twisting of magnetic states takes place in several spatial directions, more complex states may be found. Such states can be visualized as analogues to skyrmions in the chiral helimagnets. E.g., in a chiral metamagnet, a small two-dimensionally localized tube or even a three-dimensionally localized ball of ferromagnetic spin-configuration may become stable, immersed in a background of antiferromagnetic order. We believe that future research on further magnetically ordered crystals will reveal such textures.

References

- [1] Rößler, Bogdanov and Pfleiderer, Nature 442 (2006) 797
- [2] Kiselev et al., J. Phys.D: Appl. Phys. 44 (2011) 392001
- [3] Schneider et al., Phys. Rev. Lett. 120 (2018) 217201
- [4] Kravchuk et al. Phys. Rev. B 99 (2019) 184429
- [5] Sokolov et al., Nature Phys. 15 (2019) 671

Cooperations

- ¹Max Planck Institut für Chemische Physik fester Stoffe, Dresden, Germany.
- National Institute for Materials Science, Tsukuba, Japan.
- Institut Laue–Langevin, Grenoble, France.
- Laboratory for Neutron Scattering and Imaging, Paul Scherrer Institute, Villigen, Switzerland.
- Université Grenoble Alpes, CEA, INAC-MEM, Grenoble, France.
- NIST Center for Neutron Research National Institute of Standards and Technology, Gaithersburg, USA.
- Department of Materials Science and Engineering, University of Maryland, USA.
- ESRF, Grenoble, France.
- Scottish Universities Physics Alliance, School of Physics and Astronomy, University of St Andrews, St Andrews, UK.

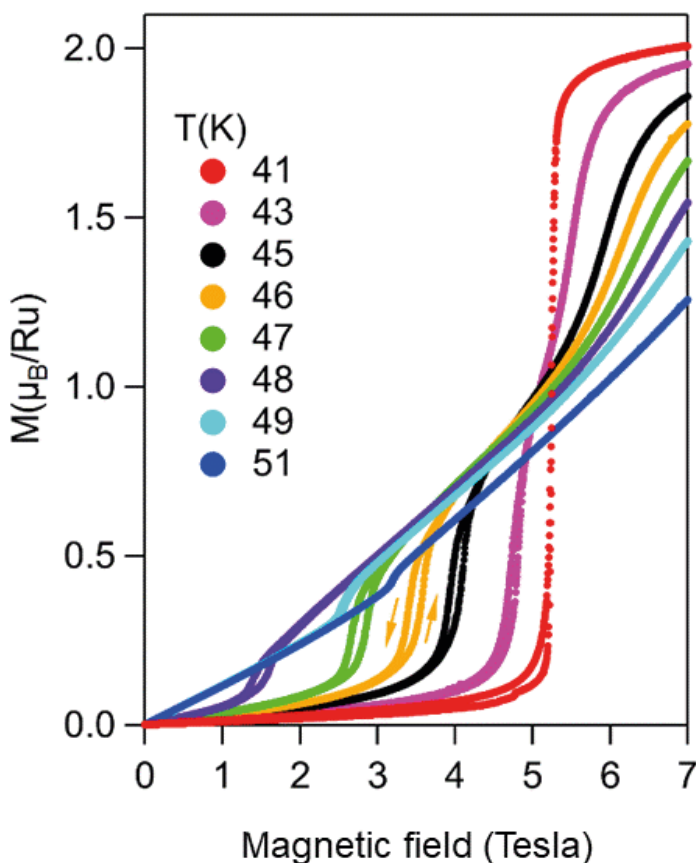


Abb. 3: Magnetisches Moment in $\text{Ca}_3\text{Ru}_2\text{O}_7$ in Abhängigkeit vom angelegten Magnetfeld bei verschiedenen Temperaturen zeigt die sogenannten metamagnetischen Anomalien als zwei scharfe Anstiege mit Hysterese.

Fig. 3: Magnetic moment versus applied field in $\text{Ca}_3\text{Ru}_2\text{O}_7$ at various temperatures show the so-called metamagnetic anomalies as two sharp rises with hysteresis.

Energy harvesting near room temperature using a thermomagnetic generator with pretzel-like magnetic field topology

Anja Waske, Daniel Dzekan, Kai Sellschopp, Dietmar Berger, Alexander Stork, Kornelius Nielsch, Sebastian Fähler

Zusammenfassung

Für die Umwandlung von Niedertemperatur-Abwärme in elektrische Energie stehen bislang nur wenige Technologien zur Verfügung. Bereits vor mehr als einem Jahrhundert wurden thermomagnetische Generatoren vorgeschlagen, die auf einer Änderung der Magnetisierung mit der Temperatur beruhen. Dabei wird ein Magnetfluss geschaltet, der entsprechend dem Faradayschen Gesetz eine Spannung induziert. Hier zeigen wir, dass eine Brezel-förmige Topologie des Magnetkreises die Kennwerte von thermomagne-

tischen Generatoren um Größenordnungen verbessert. Durch eine Kombination von Experimenten und Finite Elemente -Simulationen zeigen wir, dass diese Topologie zu einer Vorzeichenumkehr des Magnetflusses führt, Hysterese sowie magnetische Streufelder vermeidet und ein vielseitiges Design ermöglicht.

Abstract

To date, there are only few technologies available for the conversion of low temperature waste heat to electricity. More than a century ago, thermomagnetic generators were proposed, which are based on a change of magnetisation with temperature, switching a magnetic flux, which according to Faraday's law induces a voltage. Here we demonstrate that a pretzel-like topology of the magnetic circuit improves the performance of thermomagnetic generators by orders of magnitude. By a combination of experiments and finite element simulations, we show that this topology results in sign reversal of the magnetic flux, avoids hysteresis as well as magnetic stray fields, and allows for versatile device design.

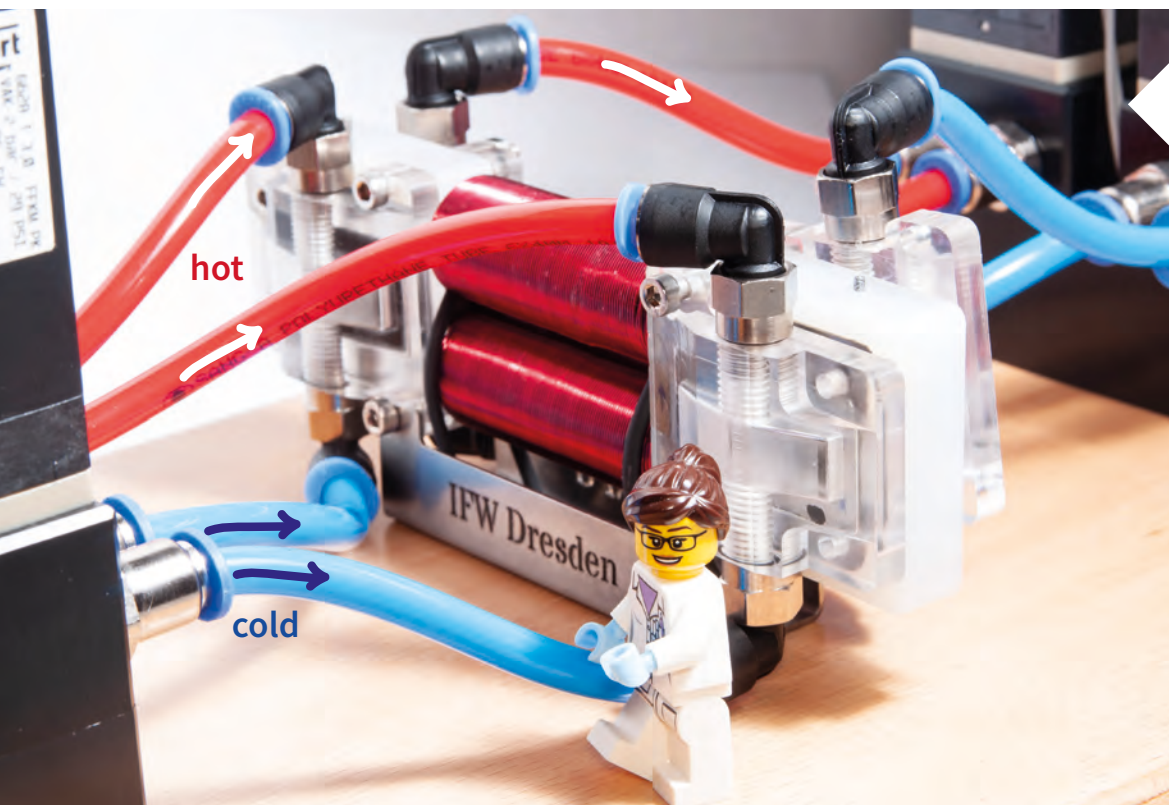


Abb. 1: Foto unseres thermomagnetischen Generators (TMG), der Niedertemperatur-Abwärme in elektrische Energie umwandelt. Als aktives Material wird ein thermomagnetisches Material basierend auf La-Fe-Co-Si verwendet, das eine hohe und abrupte Änderung der Magnetisierung knapp oberhalb von Raumtemperatur aufweist. Das thermomagnetische Material wird durch Wasser abwechselnd aufgeheizt und gekühlt.

Fig. 1: Photo of our thermomagnetic generator (TMG), which converts low temperature waste heat to electric energy. As active material a thermomagnetic material based on La-Fe-Co-Si is used, which exhibits a steep and sharp change of magnetization just above room temperature. The thermomagnetic material is alternately subjected to hot and cold water.

In a finite world, the sources of primary energy are limited and thus they have to be used as efficiently as possible. This includes the need to recover waste heat produced by industrial processes and residential heating. A recent analysis reveals that the amount of available heat peaks just above room temperature [1]. To convert this low temperature waste heat to electricity, to date only very few technologies are available. The advanced technology is thermoelectric power generation. Apart from this solid state technology, only complex discrete systems, like e.g. the classical Stirling motor, are available.

In our paper [2] we developed the concept of a thermomagnetic generator (TMG) with the help of an advanced magnetic field topology towards a promising device for converting low temperature waste heat to electricity. Energy conversion at these low temperatures is enabled by the recent development of magnetocaloric materials, which is the functional material used for the reverse energy conversion process: creating a temperature difference using electric energy [3]. We sketch why these materials are also good thermomagnetic materials and how they are used in a TMG. Then we classify the topology of TMGs by the number of holes of the magnetic circuit or, using mathematical terms, by their genus. We show that a TMG with genus = 3 has significant advantages compared to those with a lower genus because they allow for flux reversal within the magnetic circuit. This design improvement leads to a factor of four larger power output, avoids hysteresis losses and gives more flexibility in realizing the heat exchange with the thermomagnetic material. In order to quantify the advantages of this topology, we experimentally realize a TMG with genus = 3, characterize the dependency of the electrical output power on the key operation parameters, and compare them with TMGs with lower genus. We discuss why this development paves the way for TMGs to become competitive with thermoelectric generators for waste heat recovery near room temperature.

Thermomagnetic generators with genus = 0, 1 and 2

To illustrate the role of topology for TMGs we start with the first concepts, proposed already by Tesla and Edison in two patents more than hundred years ago. The functional material used within a TMG is a thermomagnetic material, which changes its magnetisa-

tion in dependence of temperature. In the ideal case the magnetisation changes abruptly by ΔM within a narrow temperature range ΔT around the materials transition temperature T_c . This allows considering a thermomagnetic material as a thermal switch. The thermomagnetic material is part of a magnetic circuit. This circuit additionally contains one permanent magnet as source of magnetic flux Φ and two ferromagnetic yokes to guide the flux. Within this magnetic circuit the thermomagnetic materials are used as a thermal switch for the magnetic flux. At temperatures below T_c , the thermomagnetic material is in the ferromagnetic state and thus guides the flux. When the thermomagnetic material is hot, it becomes paramagnetic and the flux switch opens. To convert the thermal energy required to heat the thermomagnetic material into electric energy, an induction coil is wound around the flux switch material. Following Faraday's law $V = -N d\Phi/dt$, this flux change with time $d\Phi/dt$ through a coil with N windings induces an electric voltage V .

The topology of the magnetic circuit proposed by Tesla [4] and Edison [5] is simple: it has one hole, and thus we will classify it by a genus of 1. Despite its simplicity, this donut like topology has one major drawback. When the flux switch opens, the magnetic flux lines created by the permanent magnet must still close. This is not possible anymore through a ferromagnetic material, but only through the ambient air. Presumably this is the reason why in literature there are no reports on a successful experimental realization of a TMG with genus = 1. More than a century later, Srivastava et al. [6] reinvented the TMG. In their setup no yoke is used to close the magnetic circuit, and thus their topology is of genus = 0. However, they were first to propose using first-order magnetocaloric materials also for thermomagnetic generators. For this energy conversion application, the functional material must exhibit a strong and steep change of magnetisation in a narrow temperature range [3]. The strong change in magnetisation allows switching a large magnetic flux, and the narrow temperature range needed for this reduces the thermal energy required for switching. Thus, first order magnetocaloric materials are also excellent thermomagnetic materials, as they come very close to an ideal on/off flux switch. A few years later, Christiaanse and Brück [7] realized the first TMG with genus = 2. They use two thermomagnetic materials, which are alternatingly

cooled and heated. Thus, the magnetic flux, created by the permanent magnet, is always guided through one of the thermomagnetic materials. This avoids magnetic stray fields.

Topology of a thermomagnetic generator with genus = 3 exhibiting flux reversal

Starting point for our TMG with genus = 3 (Fig. 2a) is the TMG with genus = 2, where two thermomagnetic materials are heated and cooled alternately. This pretzel-type topology allows keeping the advantage of magnetic stray field minimization. Instead of a single permanent magnet, we now introduce two, which both point towards the same direction. Consequently, a third magnetic circuit occurs between both permanent magnets. This additional circuit allows for sign reversal of the magnetic flux within both yokes when alternating the temperature of both thermomagnetic materials. This has decisive advantages for a TMG, as described in the following.

First, it is favourable to place the induction coils around the yokes within the new, third magnetic circuit. Whereas in the old positions the flux within the induction coils varied from zero to maximum flux, now the flux varies between negative and positive maximum flux. As the induced power scales with the square of the flux change, [8] flux reversal gives an increase of power by a factor of four. Moreover, the maximum flux is not anymore limited by the low

saturation magnetisation of the thermomagnetic material of about 1 T, but by the significantly higher saturation magnetisation of the soft magnetic iron yoke of 2.2 T. Second, flux reversal minimizes hysteretic effects, which are present also in soft magnetic materials. Even in good soft magnetic materials, the remanent magnetisation can reach up to 50% of saturation magnetisation, which substantially reduces the usable flux change. Third, removing the induction coils from the thermomagnetic materials significantly facilitates the design of a TMG. It is not anymore necessary to realize a complex geometry [7], in which induction and thermal switching takes place in the same thermomagnetic material.

Realization of a thermomagnetic generator with genus = 3

For the TMG with genus = 3, we realize the thermomagnetic material as two sets of parallel plates. This geometry is ideal for a TMG, as it allows for a non-interrupted flow of the magnetic flux within the plate, as well as for a fast heat exchange perpendicular to the plate due to its high surface-to-volume ratio. As particular thermomagnetic material we chose La-Fe-Co-Si due to its high change in magnetisation, high abundance and low environmental impact, which makes it also one of the most promising magnetocaloric materials [3]. Last, but not least, plates with a size of 10 mm x 10 mm x 0.5 mm with $T_c = 300$ K are

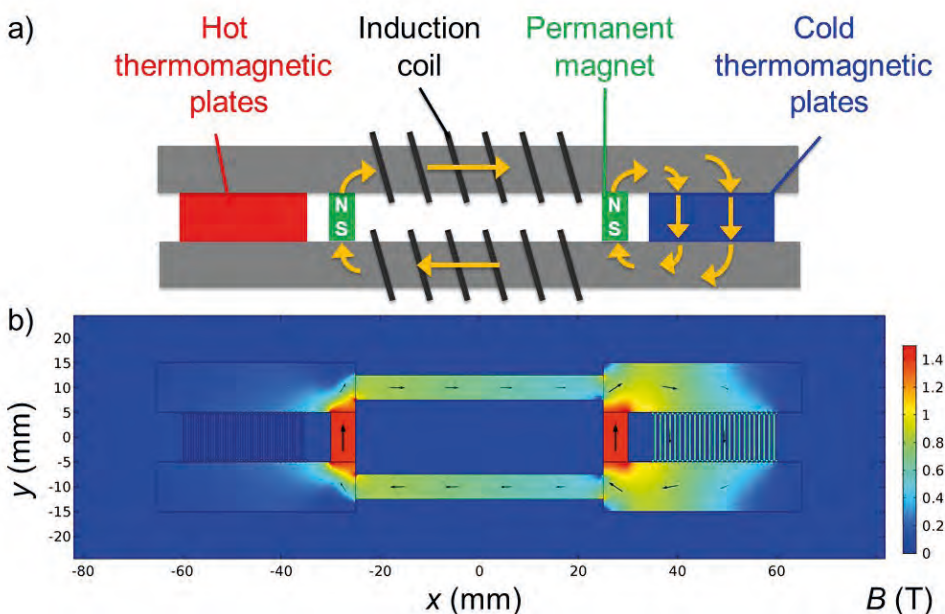


Abb. 2: Thermomagnetischer Generator mit Genus = 3 (3 Löcher im Magnetkreis).
 a) Der Aufbau besteht aus zwei Permanentmagneten, die den magnetischen Fluss erzeugen, zwei weichmagnetischen Jochs, die den Fluss leiten, und zwei Sätzen von thermomagnetischen Platten, die den Fluss schalten. Jedes Mal, wenn die Temperatur der thermomagnetischen Platten auf beiden Seiten zwischen heiß und kalt geändert wird, kehrt sich die Richtung des Magnetflusses um, wodurch in den Spulen eine Spannung induziert wird. b) zeigt das Ergebnis von Finite-Elemente-Berechnungen der magnetischen Flussdichte B für diesen Aufbau.

Fig. 2: Thermomagnetic generator with genus = 3 (3 holes within the magnetic circuit).
 a) The setup consists of two permanent magnets which create the magnetic flux, two soft magnetic yokes which conduct the flux and two sets of thermomagnetic plates which switch the flux. Each time the temperatures of the thermomagnetic plates on both sides is exchanged between hot and cold, the direction of the magnetic flux is reversed, which induces a voltage in the coils. b) shows the result of finite element calculations of the magnetic flux density B for the same setup.

available off the shelf from Vaccumschmelze, and we build our TMG with these boundary conditions. The sketch of our TMG is shown in Fig. 2a and a photo in Fig. 1. Upstream of the thermomagnetic plates, a mixing chamber for the heat exchange fluids is placed. This allows switching between the hot fluid coming from top, and cold fluid coming from bottom. The B -field distribution obtained by finite element calculations is shown in Fig. 2b, which illustrates that only little magnetic stray field leaves the magnetic circuit.

Summary

The impact of topology on thermomagnetic generators (TMG) is summarised in Fig. 3, where the key operational parameters are shown in dependency of their genus, i.e. the number of holes within the magnetic circuit. For all parameters, i.e. induced voltage, electrical output power, optimum frequency, and ratio between experiment and theory, a logarithmic scale is necessary to cover the orders of magnitude in improvement when using a topology with genus = 3. This pretzel-like topology allows for sign reversal of the magnetic flux, avoids hysteresis losses and magnetic stray fields. Ongoing research at the IFW focuses on increasing the thermodynamic efficiency by reducing thermal losses and minimizing the heat required for switching the thermomagnetic material. In another project together with KIT Karlsruhe we examine thermomagnetic films for thermomagnetic micro-oscillator, which uses a similar approach at the microscale.

References

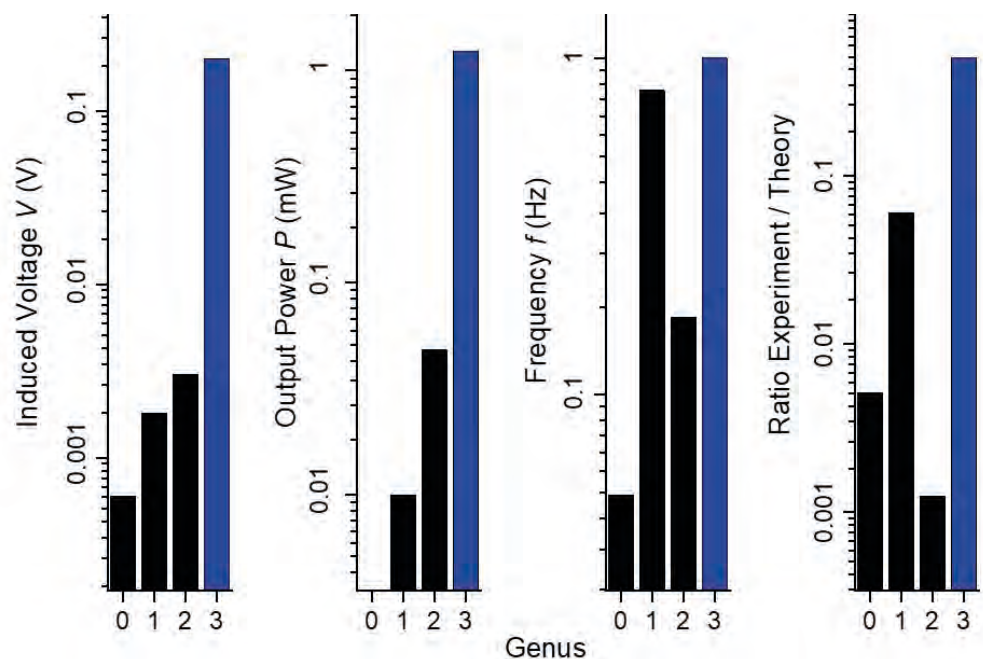
[1] G. Schierning, Nat. Energy 3 (2018) 92
 [2] A. Waske et al., Nat. Energy 4 (2019) 68
 [3] A. Waske et al., MRS bulletin 43 (2018) 269
 [4] N. Tesla, Pyromagneto Electric generator, US Patent 428,057 (1890)
 [5] T. A. Edison, Pyromagnetic Generator, US Patent 476,983 (1892)
 [6] V. Srivastava et al., Adv. Energy Mat. 1(1) (2011) 97
 [7] T. Christiaanse et al., Met. Mat. Trans. E 1(1) (2014) 36
 [8] L. Brillouin, H. P. Iskenderian, El. Com. 25(3) (1984) 300

Cooperations

Bundesanstalt für Materialforschung und -prüfung (BAM), Berlin
 TU Dresden
 KIT Karlsruhe.

Abb. 3: Vergleich der wichtigsten Eigenschaften von thermomagnetischen Generatoren mit unterschiedlichen Topologien, sortiert nach ihrem Genus (d.h. Anzahl der Löcher im Magnetfeldkreis). Die induzierte Spannung ist die maximale Spannung, die in Experimenten erreicht wurde, und die gesamte elektrische Ausgangsleistung sowie die Frequenz sind die angegebenen optimalen Werte. Das Verhältnis zwischen Experiment und Theorie gibt an, wie nahe die experimentellen Werte den theoretischen Werten kommen. Genus = 3 ist die in dieser Arbeit vorgestellte neuartige Topologie.

Fig. 3: Comparison of key properties of thermomagnetic generators with different topologies, categorized by their genus (i. e. number of holes in the magnetic circuit). The induced voltage is the maximum voltage reached in experiments, and total electrical output power as well as frequency are the optimum values reported. The ratio between experiment and theory indicates how close the experimental values approach the theoretical values expected from the design of the thermomagnetic generator. Genus = 3 is the novel topology introduced in this work.



Structure-property relationship of Co_2MnSi thin films in response to He^+ -irradiation

Franziska Hammerath, Rantej Bali¹, René Huebner¹, Mira R. D. Brandt, Steven Rodan, Kay Potzger¹, Roman Boettger¹, Yuya Sakuraba², Sabine Wurmehl, Patrizia Fritsch

Zusammenfassung

Die gezielte Bestrahlung mit He^+ Ionen kann die (lokale) Struktur von Materialien und damit auch deren funktionale Eigenschaften verändern. Als Modellsystem zur Untersuchung der Struktur-Eigenschaftsbeziehungen diente ein dünner Film der Heusler Verbindung Co_2MnSi , die vor allem wegen ihrer magnetischen Eigenschaften interessant ist. Die Veränderung der Kristallstruktur mit zunehmender Ionenfluenz in Co_2MnSi wurde mittels Kernspin-

resonanzspektroskopie (NMR) und Transmissions-elektronenmikroskopie (TEM) untersucht und mit den entsprechenden makroskopischen Änderungen der magnetischen Eigenschaften in Bezug gesetzt.

Abstract

The irradiation with He^+ ions allows to deliberately change the (local) structure of materials and, thus, allows to concomitantly modify their functional properties. The model system used to study its structure-property relationship was a thin film of the Heusler compound Co_2MnSi , which is of particular interest for its magnetic properties. The change in crystal structure with increasing ion fluence in Co_2MnSi was investigated by nuclear magnetic resonance spectroscopy (NMR) and transmission electron microscopy (TEM) and correlated with the corresponding macroscopic changes in magnetic properties.



Abb. 1: Doktorandin bei der Vorbereitung einer Untersuchung mit Kernspinresonanzspektroskopie (NMR)

Fig. 1: PhD student preparing for nuclear magnetic resonance spectroscopy (NMR) measurements.

Ion irradiation as tool to alter structure and properties of functional materials

The macroscopic properties of (functional) materials are inherently linked to their (local) structure. Hence, structure-property relationships need to be taken into account when a specific functionality is envisaged. There are different approaches to alter the structure of a material with annealing at elevated temperatures the most common technique. A more exotic but efficient way to deliberately change the (local) structure of materials is their irradiation with light ions, e.g., with He^+ [1]. During the irradiation process, energetic He^+ ions clash with individual atoms within the target material displacing them from their original atomic sites. This displacement of atoms caused by the incident ion beam creates vacancies in the crystallographic lattice, which will stochastically recombine with thermally diffusing atoms and, hence, modifies the (local) structure of the irradiated material.

Co_2MnSi Heusler compound as model system

The Heusler compound Co_2MnSi is a promising candidate for showing full spin polarization of the conduction electrons [2]. Fully spin polarized materials are considered relevant as functional layer in spintronic devices, for instance in magnetic tunnel junctions (MTJ) or giant magnetoresistance (GMR) devices. However, full spin polarization is predicted only for specific crystallographic structures among those the fully ordered so-called $\text{L}2_1$ type structure. In that context, full order refers to a well-defined arrangement of the Co, Mn and Si atoms on the crystallographic lattice. In contrast, a disordered structure denotes presence of atomic site disorder, viz, that the arrangement of atoms on the crystallographic sites is not well-defined anymore, but atoms are randomly swapping sites. Such a disordering may involve only certain fractions and types of atoms leading to different structure types. In the extreme case of all atoms mixing up on all crystallographic sites, we are dealing with the so-called A2 type structure. Disorder has strong impact on the macroscopic and, in particular, on the magnetic properties of Co_2MnSi [2]. Hence, Co_2MnSi represents an ideal model system to study the structure-property relationship in response to ion irradiation.

Complementary methods

To study the structure changes in response to ion irradiation, we need a method that allows to probe the local atomic environment. Structure analysis by zero-field ^{59}Co solid-state nuclear magnetic resonance (NMR) allows determination of local atomic environments on an integral scale [3] and even enables a quantitative analysis of structural phase fractions. We complement the NMR results with transmission electron microscopy (TEM) studies since TEM enables imaging down to the atomic scale. A similar combination of NMR and TEM was already successfully used to study the chemical composition of multi-element nanostructures [4]. The degree of spin polarization of Co_2MnSi is monitored by changes in magnetic properties measured by magnetometry.

Identification of changes in local structure of Co_2MnSi induced by He^+ irradiation

A set of Co_2MnSi films with same properties were prepared. One was used as non-irradiated reference, the remaining ones were irradiated with different fluences of He^+ . We now compare the ^{59}Co NMR spectrum of the non-irradiated sample (grey dots in Fig. 2) with the spectra of those films that have been exposed to different fluences of He^+ ions. Obviously, even the lowest fluence is sufficient to alter the (local) structure of the Co_2MnSi film. This structural change manifests in both an increasing width of the NMR line compared to the pristine sample and in the observation of an additional very broad line. This additional line gains spectral weight with increasing fluence. We refer to the resonance line observed in the non-irradiated samples as $\text{L}2_1$ line and to the additional line as A2 line. Please note that this assignment reflects the specific local environments and that the notation of the two lines follows the Strukturbericht designation. Remarkably, one identifies three regimes:

(i) for fluences between 10^{13} – 10^{14} cm^{-2} the spectrum broadens slightly, compared to the non-irradiated sample; concomitantly, the broad additional A2 line is a minority but non-negligible contribution to the overall spectrum reflecting an increasing structural disorder.

- (ii) For higher fluences (5×10^{14} – 10^{15} cm⁻²), the fraction of the A2 line further increases. Concomitantly, the L2₁ line width increases significantly and its resonance frequency shifts to lower values.
- (iii) The spectrum of the sample irradiated with the highest fluence (5×10^{15} cm⁻²) is completely smeared out over the whole measured frequency range and no distinct peak can be identified (pink dots in Fig. 2). Such a broad NMR resonance line is typical for a stochastic distribution of all atoms on all crystallographic sites. This situation is typically referred to as fully disordered structure.

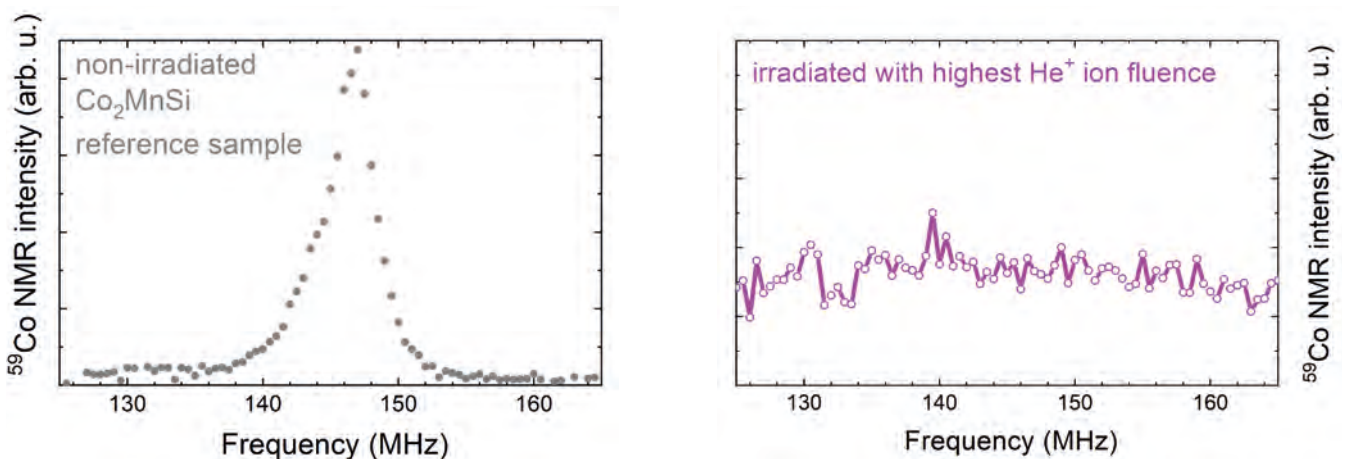
While we are probing the full volume of the film without any losses due to film thickness, the NMR method does not reveal from which position in the samples a certain NMR signal is excited, e.g., from Co atoms at the top or at the bottom of the film. Hence, we complemented the NMR results with TEM which can provide spatially resolved information about the local structure at a specific sample position. According to our HRTEM results, there is a depth-dependent structural order in the irradiated samples: regions next to the surface are mainly disordered, while regions next to the substrate still retain the original L2₁ structure (for details, see original publication).

Structure-property relationships in Co₂MnSi altered by ion irradiation

We now turn to the relation between (local) structure and macroscopic magnetic properties. We see a clear trend of decreasing moment in saturation (M_{sat} right axis in Fig. 4) with increasing ion fluence. We also see a linear trend of increase in disorder upon irradiation with increasing He⁺ fluence. Both trends have opposite sign, viz. with increasing disorder induced by ion irradiation, we decrease the moment in saturation. Hence, ion-irradiation can subtly vary or even fully disorder the local structure. This modification of the structure in turns impacts on the macroscopic magnetic properties, as a manifestation of the strong structure-property relationships in Heusler compounds.

Abb. 2: Zunehmende Unordnung durch die Bestrahlung mit He⁺ Ionen sichtbar in der Veränderung der lokalen Struktur
 normalisiertes ⁵⁹Co NMR Spektrum der unbestrahlten Co₂MnSi Referenzprobe: graue Punkte (links)
 normalisiertes ⁵⁹Co NMR Spektrum der mit der höchsten Fluenz an He⁺ Ionen bestrahlten Probe: pinkfarbene Punkte (rechts)

Fig. 2: Increasing disorder upon irradiation with He⁺ ions as evident from the measurement of the local structure
 normalized ⁵⁹Co NMR spectrum of the non-irradiated Co₂MnSi reference sample: grey dots (left)
 normalized ⁵⁹Co NMR spectrum of the sample irradiated with the highest fluence of He⁺ ions used in the study at hand: pink dots (right)



Published in
Structure-property relationship of Co_2MnSi thin films in response to He^+ -irradiation, F. Hammerath, et al., Scientific reports 9, 2766 (2019)

References

- [1] J. Fassbender et al., J. Phys. D: Appl. Phys. 37, R179 (2004).
- [2] T. Graf et al., Prog. Solid State Chem. 39, 1(2011); M. Jourdan et al., Nature Comm. 5, 3974 (2014)
- [3] S. Wurmehl, J. T. Kohlhepp, Spin 4, 1440019 (2014).
- [4] M. Gellesch et al., J. Nanoparticle Res. 19, 307 (2017).

Funding

Deutsche Forschungsgemeinschaft (DFG) through Sonderforschungsbereich SFB 1143, and Grants No. WU595/3-3 and WU595/14-1.

Cooperations

- 1) Helmholtz-Zentrum Dresden-Rossendorf (HZDR), Germany.
- 2) National Institute of Materials Science, Japan. Universität Bielefeld, Germany. TU Darmstadt, Germany. TU Dresden Germany. TU Eindhoven, Netherlands.



Abb. 3: Probe für NMR-Messungen verpackt in weißer Teflon-Folie und mit einer Kupferspule zum Senden und Empfangen von Radiofrequenzsignalen umwickelt. Die Probe wird in einer durchsichtigen Plastikdose aufbewahrt. Im Hintergrund sieht man weitere NMR Proben.

Fig. 3: Sample for NMR measurements enclosed in Teflon foil (white) for protection and enwind with a copper coil allowing to send and receive radio-frequency signals. Sample is stored in transparent plastic box. Background shows a selection of other NMR samples.

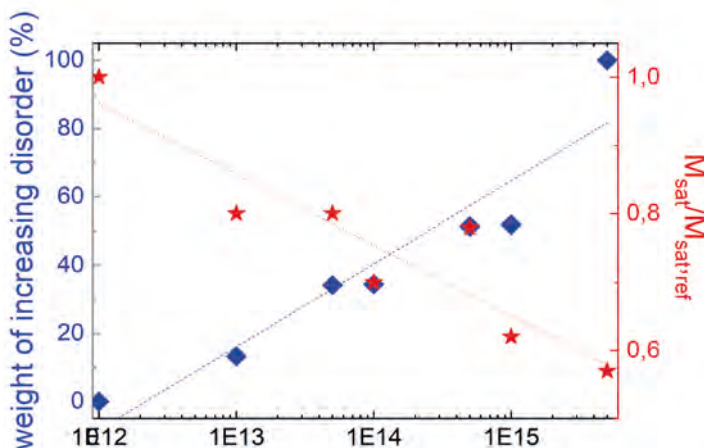


Abb. 4: Beiträge der Unordnung (blaue Rauten, linke Achse) und das magnetische Moment (rote Sterne, rechte Achse) jeweils als Funktion der zunehmenden Bestrahlung. Die gepunkteten Linien entsprechen einer linearen Anpassung an die Daten.

Fig. 4: Irradiation-dependent weight of the increasing disorder (blue diamonds, left axis), and the corresponding change in the saturation moment (red stars, right axis). The dotted lines represent linear fits to the data.



FORSCHUNGSGEBIET 2:

Funktion durch Nanoskaligkeit

RESEARCH AREA 2:

Function through size

Funktion durch Nanoskaligkeit

Dieses Forschungsgebiet befasst sich mit Materialien, deren Eigenschaften aus strukturellen Anordnungen im Nanomaßstab resultieren: Dazu gehören Nichtgleichgewichts- und nanostrukturierte Legierungen, aufgerollte Nanomembranen und Mikromotoren sowie thermoelektrische Materialien. Die Funktionalität dieser Materialien hängt entscheidend von der Größe ihrer Partikel und von Oberflächeneffekten ab. Viele Materialeigenschaften ändern sich beim Übergang vom makroskopischen über den mikroskopischen zum nanoskopischen Maßstab. Das wird in nanostrukturierten Legierungen deutlich, die für Anwendungen als Biomaterialien und als hochfeste Werkzeuge entwickelt werden. Ein weiterer Schwerpunkt sind elastische oder aufgerollte Nanomembranen, die in einer neuen Generation von flexiblen und kompakten On- und Off-Chip-Bauelementen eingesetzt werden. Im Forschungsgebiet 2 befassen wir uns außerdem mit der Entwicklung neuer thermoelektrischer Materialien. Durch Nanostrukturierung und den Einsatz spezieller Legierungen soll die Effizienz thermoelektrischer Bauelemente erhöht werden, um das Anwendungspotential zu erweitern. All diese Themen beleuchten die Struktur, die chemische Zusammensetzung und die physikalischen Eigenschaften von Materialien auf unterschiedlichen Längenskalen. Die Forschung wird von der Vernetzung interdisziplinärer Teams aus Material- und Elektroingenieuren, Physikern und Chemikern getragen.

Function through size

This Research Area comprises research on materials with properties arising from structural arrangements at nanoscale. These are non-equilibrium and nanostructured alloys, rolled-up nanomembranes and micromotors, as well as thermoelectric materials. The functionality of these materials decisively depends on the size of their particles and on interfaces. This is evident in nanostructured alloys that are developed for applications as biomaterials and as high-strength tools. Another focus is on elastic or rolled-up nanomembranes which will be exploited in conceptually new generations of flexible and compact on- and off-chip devices. Shape, size and interfaces also determine the fundamental properties of nanomagnets, which may find use in magnetic probes and data storage elements. We also address the improvement of new thermoelectric materials, e.g. special alloys, and the various capabilities of nanostructuring show enhanced efficiency and promise new applications. All research efforts are cross-linked by common methodological approaches and interests, which shed light on the structure, chemical composition and physical properties of materials at different length scales. The research area relies on the expertise of an interdisciplinary team of materials and electrical engineers, physicists and chemists and deals with the unique mechanical and functional properties of materials as they or their constituents change from macro-, to micro- and nanoscopic sizes.

Medical imaging of micromotors through scattering tissues

Azaam Aziz, Mariana Medina-Sánchez, Nektarios Koukourakis, Jing Claussen, Jiawei Wang, Hannes Radner, Robert Kuschmierz, Jürgen W. Czarske, and Oliver G. Schmidt

Zusammenfassung

Mikroroboter, die sich selbständig durch den Körper bewegen und am Zielort Medikamente freisetzen oder gar Operationen durchführen, sind keine Utopie mehr sondern ein erklärtes Ziel der Forschung. Eine der Herausforderungen, die es auf dem Weg dahin noch zu meistern gilt, ist die zuverlässige Navigation der winzigen Roboter. Hierzu ist es nötig, die Mikroobjekte bei ihrer Arbeit in Echt-Zeit sichtbar zu machen. Bisher wurden verschiedene Bildgebungsverfahren untersucht, welche jedoch aufgrund der Lichtstreuung im Gewebe nicht die nötige Auflösung erreichten. Im IFW wurde auf diesem Gebiet ein wichtiger Fortschritt erreicht. Es ist gelungen, ein Infrarot-Bildge-

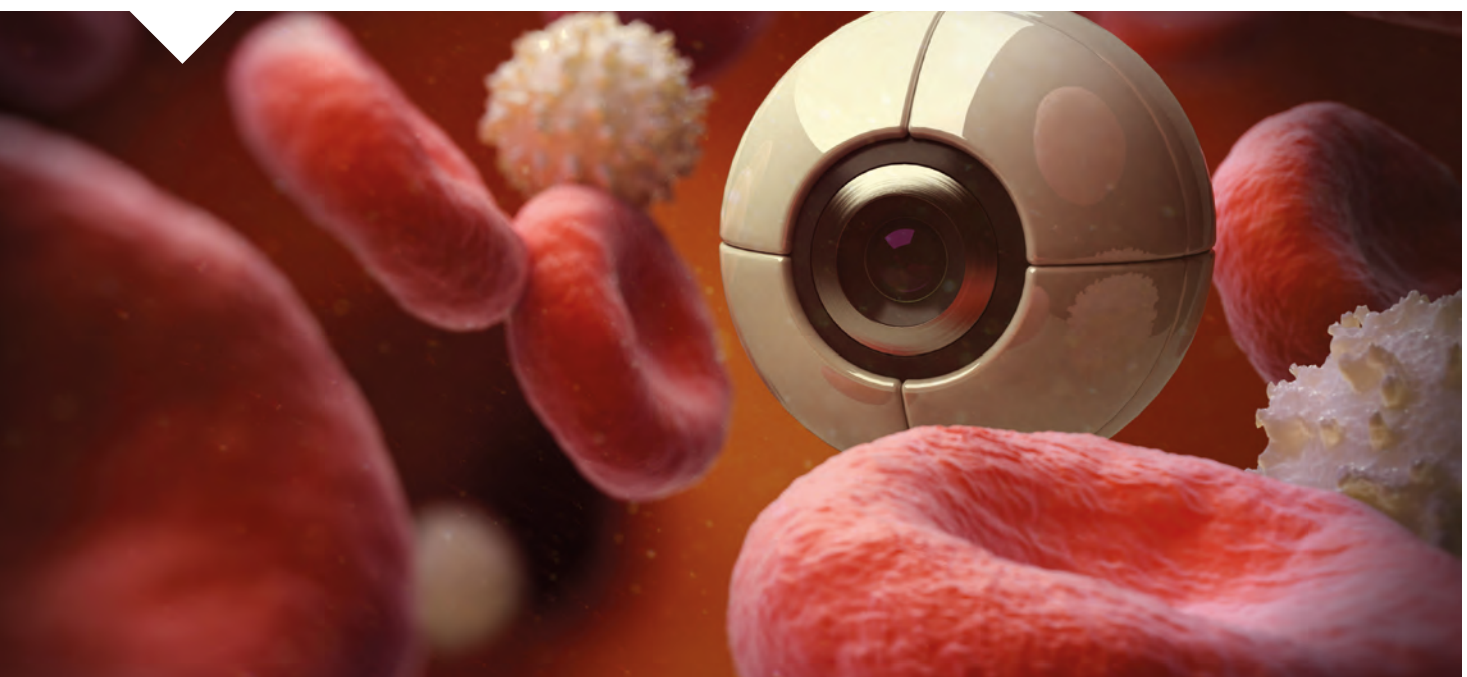
bungsverfahren so weiterzuentwickeln, dass 20 und 100 Mikrometer große Objekte abgebildet werden. In einem zweiten Ansatz konnten wir mittels sogenannter optoakustischer Tomografie einzelne 100 Mikrometer große Röhrchen unter einer ein Zentimeter starken Gewebeschicht in Echt-Zeit lokalisieren.

Abstract

Micromotors have the potential to revolutionize the medicine and offer the potential to operate in biological environments, performing assigned functions. However, to transfer this technology to the clinic, one of the major challenges is to be able to see them through deep tissues with high spatiotemporal resolution [1]. So far, different imaging techniques have been explored, but they are still too coarse for single microbot imaging. We explored the use of a simple IR imaging setup to visualize the mobile microbots (20 and 100 μm in size) under scattering tissues using the principle of light reflection. The second approach, optoacoustic imaging, was used to track single microtubes (100 μm in length) in 3D and in real-time below ~ 1 cm ex vivo chicken breast tissue.

Abb. 1: Visionen zur minimalinvasiven Mikrochirurgie – mit der erstmaligen Echtzeitortung von beweglichen Mikroobjekten tief im Gewebe ist ein wichtiger Schritt dorthin gelungen. Bildquelle: Science Picture Co / Alamy Stock Photo

Fig. 1.: Visional minimal invasive microsurgery - with the first-time real-time tracking of mobile micro-objects deep in the tissue, a decisive step has been taken. Credit: Science Picture Co / Alamy Stock Photo



IR Tracking of Single Reflective Micromotors through Scattering Tissues

We report the fabrication of reflective micromotors (100 and 20 μm in diameter) by using half-coated transparent silica particles with thin metal layers (50 nm Au, 10 nm Ti, 30 nm Fe and 50 nm Au). The magnetic actuation was realized by incorporating an iron layer and the gold layer exhibits high reflectivity [2] and was chosen as a reflective layer in both sides of the motor. The micromotors were illuminated by an IR LED 970 nm light source. Fig. 2a shows that the incident light, reaching the gold-coated surface of the micromotor, reflects back towards the light source. SEM image shows the hemispherical part of the particle indicating the gold and silica regions (Fig. 2b). This reflector configuration of the motor makes it easy to detect in comparison to a small spot obtained by a gold particle (Fig. 2c). In case of a gold particle, incident light will scatter in all directions with lower amounts returning to the detector.

The reflective micromotors were imaged with and without the scattering phantoms and the mouse skull tissues. The phantoms were fabricated using a mixture of polydimethylsiloxane (PDMS) and glycerol as described previously [3]. The micromotors were tracked in real-time in an enclosed channel driven by an external magnetic field. The signal strength collected by the camera depends on the thickness of the phantom tissues. The used phantoms had thicknesses from 0.8 mm to 2.2 mm, and the maximum power was used ~ 350 mW for 2.2 mm thickness. The strength of the micromotors in 'reflector' configuration strongly increases the signal coming from the particle and thus shifts the limiting tissue thickness. In this work, the limitation of the approach is the saturation of the camera. Meaning that if background intensity is enough to saturate the camera at a certain exposure time, we have no chance to get any information. If the signal of the particle is strongly enhanced by the reflector, we can decrease the exposure time and thus decrease the integrated background intensity. Initially, the micromotor can be clearly distinguished in the processed images up to 1.8 mm. It was possible to track the small micromotors (20 μm) through 1.8 mm phantom (Fig. 2d). As the bigger micromotors (100 μm) have a larger cross-section, the amount of back reflected light is much higher, leading to signals through up to 2.2 mm phantoms.

In second set of experiments, we replaced the phantoms by 8- and 14-days old mice skull tissues. First, the micromotors were imaged below the parietal bone of the skull with an approx. thickness of ~ 80 μm for the 8th day and ~ 90 μm for the 14th day old mouse. It was possible to clearly distinguish the characteristic shape of the 100 μm reflective micromotor (Fig. 2e). The skull of the 14th day old mouse was shifted to frontal bone part with an estimated thickness of ~ 110 μm . The characteristic features of the micromotor disappeared due to increased attenuation of the reflected photons through the tissues. Still it was possible to detect enough scattered light coming back towards the sensor and the position of the micromotor can be tracked.

Optoacoustic Tracking of Single Moving Micro-objects in Deep Phantom and Ex Vivo Tissues

Optical techniques offer high sensitivity and high spatial resolution but have limited penetration depth due to scattering phenomena in tissues. To overcome this problem, we present the use of multispectral optoacoustic tomography (MSOT) to image micro-objects deep within phantoms and ex-vivo chicken breast tissues, down to 1 cm. Fig. 3a shows the basic principle of MSOT imaging where tissues and micro-objects are exposed to pulsed laser light (600-900 nm). We report the fabrication of tubular micro-objects (length of 100 μm) using two-photon lithography [4] and coated with Ti/Ni for magnetic propulsion. The micro-objects were coated with Al_2O_3 by atomic layer deposition (ALD) to improve their biocompatibility and facilitate the surface functionalization with AuNRs (Fig. 3b). Commercially available AuNRs (width, 10 nm; length, 40 nm) with an absorption peak at around 820 nm were used for this study. The density of the attached AuNRs was optimized and resulted in three final densities (40, 64, and 96 AuNRs/ μm^2) after washing. Here we show only the highest density of AuNRs as seen in SEM image (Fig. 3b). In a first set of experiments, the micro-objects were embedded within the phantoms down to ~ 1 cm depth and then visualized at a single wavelength of 820 nm (AuNRs absorption peak). We observed that the optoacoustic signal from static micro-objects was proportional to the areal concentration of AuNRs (Fig. 3c). Each bright spot indicates the position of a single micro-object functionalized with AuNRs (96 AuNRs/ μm^2) (Fig. 3d). It was possible to locate

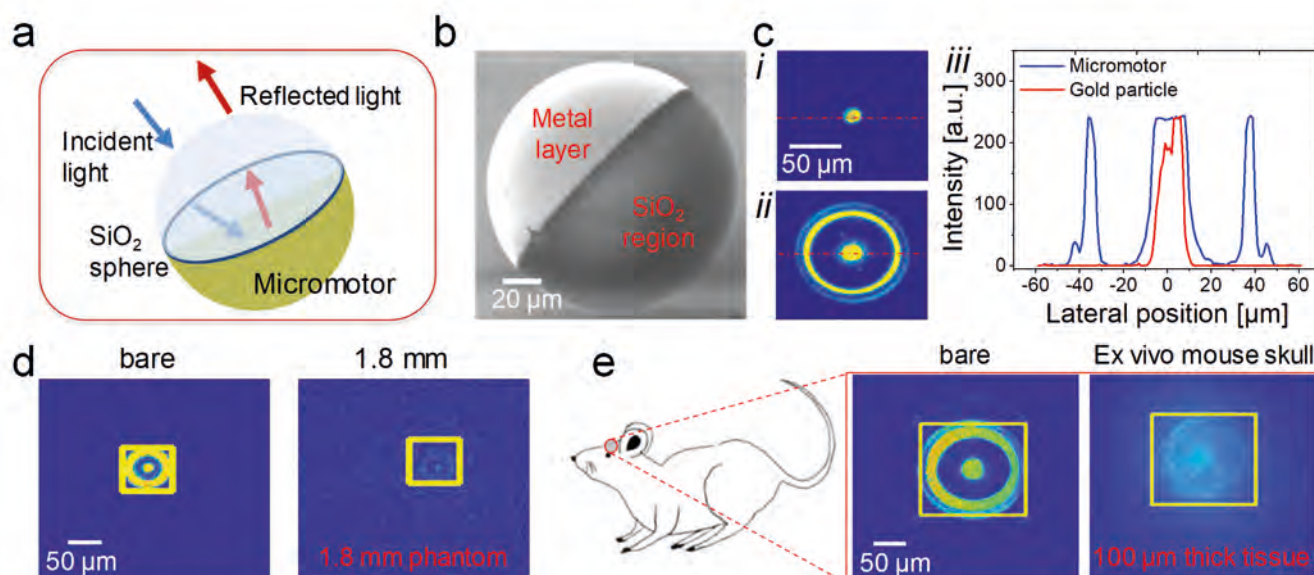
individual micro-objects and visualize their distribution inside the phantoms. For this purpose, we compared with optical images of the same phantoms with micro-objects during the fabrication process. Bright-field images correlate well with the MSOT data and reveal matching locations of the micro-objects. In the second set of experiments, a semi-cylindrical agarose phantom was prepared and placed onto a hand-held imaging detector and the AuNRs-coated micro-objects were injected into the channel. The micro-objects were moved forward by an external magnetic field (~60 mT) and the magnetic field gradient was measured using the positioning of a magnet with respect to a Hall sensor over a distance of 0–3 cm. Fig. 3e shows the real-time tracking of single micro-object in time-lapse images. The speed of the AuNRs-coated micro-objects using the MSOT was 1160 $\mu\text{m/s}$ and it agreed with the bright field video (~1070 $\mu\text{m/s}$). The average length of a moving micro-object at different locations along the trajectory was $\sim 585 \pm 40 \mu\text{m}$. Similar experiment was repeated to image the single micro-object below ex-vivo chicken breast tissues and similar results were observed and it was possible to track single moving object.

Conclusion

The presented works highlight the importance of tracking of the micromotors in scattering tissues in real-time, which is an open problem in the field of medical microrobotics. IR tracking shows the real-time and high-resolution imaging of single “reflective” micromotors (100 and 20 μm in diameter) through scattering tissues (phantom and ex vivo mouse skull). The penetration depth is limited due to pronounced photon scattering in tissues. The presented reflective micromotors have the potential to serve as drug carriers and also active microrheometers by measuring their speeds within biological fluids which in turn give information about the viscosities. To achieve better penetration, optoacoustic imaging appears to be more promising with deep tissue and real-time monitoring. We demonstrated that MSOT can be used to track single moving micro-objects (100 μm in length) in real-time below phantoms and ex vivo chicken breast tissues with a penetration depth of ~1 cm. The contrast and selectivity can be further enhanced by coating with AuNRs as they exhibit strong optical signature at 820 nm and can be distinguished from

Abb. 2: IR-Tracking von reflektierenden Einzelmikromotoren durch streuende Gewebe: a) Schema des mit Metallschichten halbbeschichteten reflektierenden Mikromotors, b) SEM-Aufnahme des Partikels mit metallbeschichtetem Bereich und transparentem Siliziumdioxidbereich, c) Signal von (i) Gold Partikel, (ii) der reflektierende Mikromotor und (iii) die entsprechende Signalintensität, d) Verfolgung eines einzelnen Mikromotors (Durchmesser: 20 μm) unter 1,8 mm dickem Streuphantom und e) Ex vivo-Verfolgung einzelner Mikromotoren (100 μm in Durchmesser) unter Mausschädelgewebe (Dicke ~90 μm).

Fig. 2.: IR tracking of single reflective micromotors through scattering tissues: a) Schematic of the reflective micromotor semi-coated with metal layers, b) SEM image of the particle showing metal coated region and the transparent silica region, c) Signal of (i) the gold particle, (ii) the reflective micromotor and (iii) the corresponding signal intensity, d) Tracking of a single micromotor (diameter: 20 μm) below 1.8 mm thick scattering phantom, and e) Ex vivo tracking of single micromotors (100 μm in diameter) under mouse skull tissues (thickness ~90 μm).



the surrounding tissues. This tool can be beneficial for localization and tracking of single micro-objects in hard-to-reach target sites within deep tissues. In summary, this achievement is of great importance for the visualization of dynamic processes that occur at the microscale, and in particular, for the tracking and control of emerging technologies such as medical microbots, micro-catheters and in general of small medical tools.

References

[1] M. Medina-Sánchez, O. G. Schmidt, “Medical microbots need better imaging and control,” *Nature*, vol. 545, no. 7655, pp. 406–408, 2017.
 [2] O. Loebich, “The optical properties of gold,” *Gold Bull.*, vol. 5, no. 1, pp. 2–10, Mar. 1972.
 [3] M. S. Wróbel, A. P. Popov, A. V. Bykov, and V. V. Tuchin, “Nanoparticle-free tissue-mimicking phantoms with intrinsic scattering,” vol. 7, no. 6, pp. 2088–2094, 2016.
 [4] M. Medina-Sánchez et al., “Rapid 3D printing of complex polymeric tubular catalytic micromotors,” 2016 Int. Conf. Manip. Autom. Robot. Small Scales, MARSS 2016, pp. 1–6, Sep. 2016.

Summarized version of the already published manuscripts:

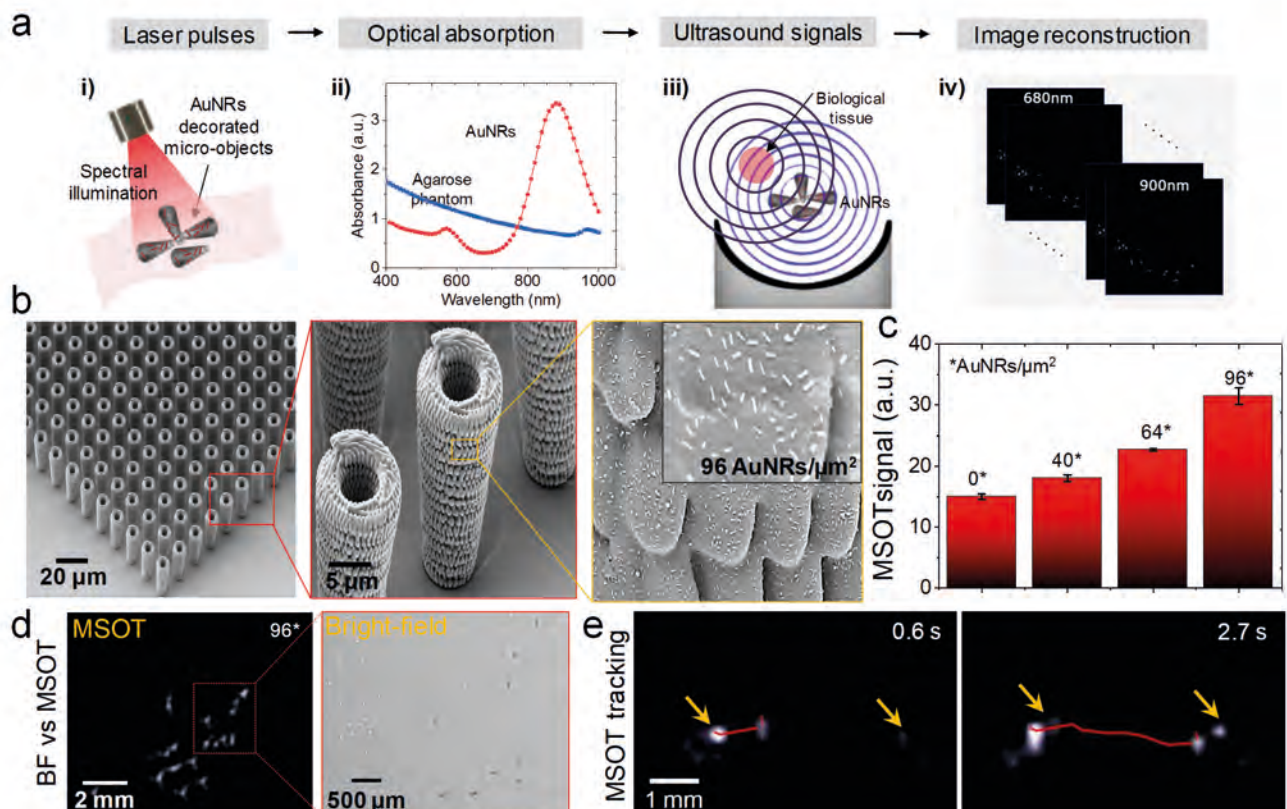
Real-Time IR Tracking of Single Reflective Micro-motors through Scattering Tissues, A. Aziz, M. Medina-Sánchez, N. Koukourakis, J. Wang, R. Kuszmierz, H. Radner, J. W. Czarske and O. G. Schmidt, *Adv. Funct. Mater.*, 29, 1905272, 2019
 Real-Time Optoacoustic Tracking of Single Moving Micro-objects in Deep Phantom and Ex Vivo Tissues, A. Aziz, M. Medina-Sánchez, J. Claussen, O. G. Schmidt, *Nano Letters*, 19, 6612–6620, 2019

Cooperations

iThera Medical München, TU Dresden.

Abb. 3: a) Prinzip des MSOT-Betriebs. Das Phantom und die Mikroobjekte werden von gepulsten Lasern beleuchtet, die nach Absorption von Licht, das zu US-Wellen führt, lokale Erwärmung erzeugen. Diese US-Wellen werden von US-Detektoren erfasst, b) SEM-Aufnahmen von 3D-gedruckten Mikroobjekten vor und nach der Funktionalisierung mit AuNRs (96 AuNRs / μm^2). c) MSOT-Signale von Mikroobjekten (100 μm Länge) mit einer Tiefe von weniger als 1 cm Phantome, d) MSOT-Signal von Mikroobjekten und das entsprechende Hellfeldbild derselben Probe, und e) Zeitrafferbilder eines einzelnen Mikroobjekts, das sich über einen Zeitraum von 2,7 s bewegt.

Fig. 3: a) Principle of MSOT operation. The phantom and micro-objects are illuminated by pulsed laser, which generate local heating after absorption of light that leads to US waves. These US waves are captured by US detectors, b) SEM images of 3D printed micro-objects before and after functionalization with AuNRs (96 AuNRs/ μm^2), c) MSOT signals from micro-objects (100 μm in length) below 1 cm deep phantoms, d) MSOT signal of micro-objects and the corresponding bright-field image of the same sample, and e) Time-lapse images of a single micro-object moving over a time period of 2.7 s.



3D self-assembly for high performance shapeable microelectronic origami

F. Gabler, Dmitriy D. Karnaushenko, Tong Kang, Vineeth K. Bandari, Feng Zhu, Daniil Karnaushenko, Oliver G. Schmidt

Zusammenfassung

Moderne mikroelektronische Systeme und ihre Komponenten sind im Wesentlichen 3D-Bauelemente, die kleiner und leichter geworden sind, um die Leistung zu verbessern und die Kosten zu senken. Um diesen Trend aufrechtzuerhalten, wurden in den letzten Jahren neuartige Materialien und Technologien entwickelt, die eine größere strukturelle Freiheit in 3D bieten als die herkömmliche Mikroelektronik. Diese Materialien ermöglichen einfachere parallele Herstellungswege und bleiben mit den vorhandenen Herstellungsmethoden kompatibel, indem planare Nanomembranen, die Funktionen der Dünnschicht-Mikroelektronik enthalten, zu komplexen 3D-Archi-

tekturen zusammengefügt werden. Wir streben die Entwicklung und Verbesserung dieser neuen Materialien und Selbstorganisationsmethoden an, um zweidimensionale Nanomembranen kontrolliert zu transformieren und eine hohe Ausbeute im Wafermaßstab zu erzielen.

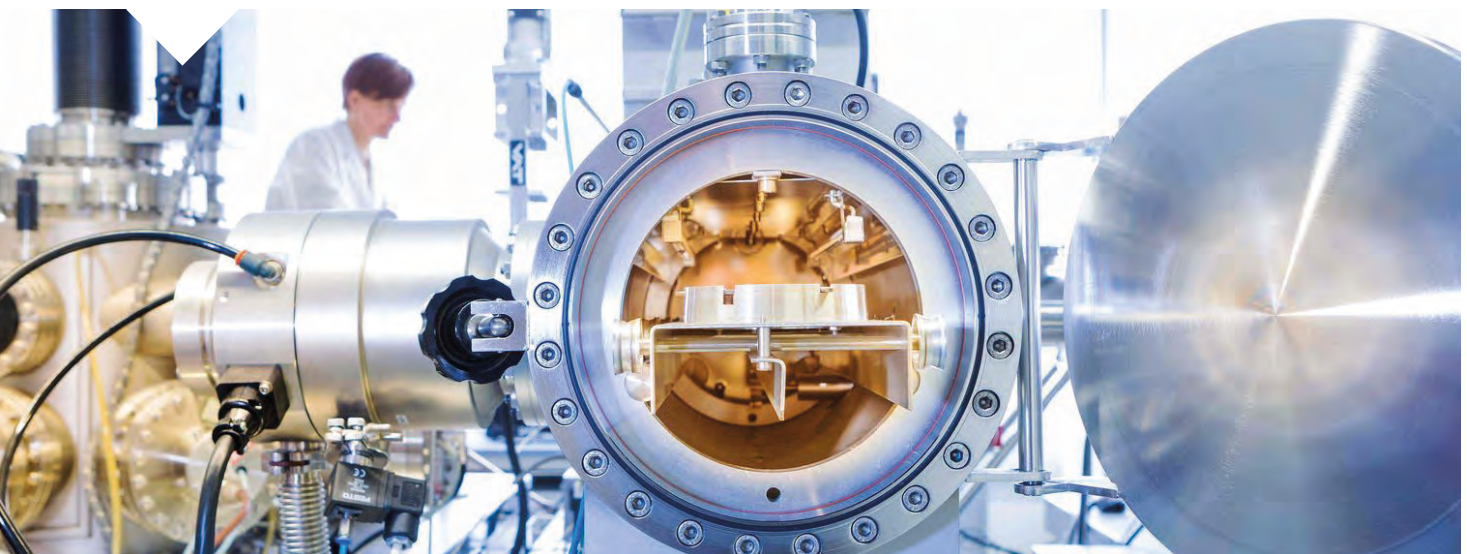
Abstract

Modern microelectronic systems and their components are essentially 3D devices which have become smaller and lighter in order to improve performance and reduce costs. Maintaining this trend, novel materials and technologies have occurred in recent years offering more structural freedom in 3D over conventional microelectronics. These materials provide easier parallel fabrication routes and remain compatible with existing manufacturing methods through self-assembly of planar nanomembranes accommodating thin-film microelectronic functionalities into complex 3D architectures. We strive to develop and improve these new materials and self-assembly methods with unprecedented control and high yield on wafer-scale.

Abb. 1: Die Dünnschichtherstellung mikroelektronischer Funktionen basiert auf Hoch- und Ultrahochvakuumtechnik, die mit Wafern in verschiedenen Maßstäben arbeiten (im Bild: Wafer-Scala-Systeme \varnothing 75 mm). Solche Systeme erzeugen Dünnschichten aus Metallen, Dielektrika und Halbleitern durch physikalische Gasphasenabscheidung, die als Sputtern (Maschine auf dem Foto) bezeichnet wird und in einer Argonatmosphäre durchgeführt wird. Hergestellte und lithographisch strukturierte Dünnschichten besitzen mechanische und elektrische Funktionen, die in Magnetsensoren, passiven und aktiven elektronischen Funktionsblöcken sowie Energiespeichern eingesetzt werden.

Foto: Jürgen Lösel

Fig. 1.: Thin-film fabrication of microelectronic functions rely on high and ultrahigh vacuum equipment operating with wafers at various scales (photo: \varnothing 75 mm wafer-scale system). Such systems create thin-films of metals, dielectrics and semiconductors via physical vapor deposition process called sputtering (machine shown in the photo), which is carried out in atmosphere of argon. Manufactured and lithographically structured thin-films possess mechanical and electrical functions employed in magnetic sensors, passive and active electronic functional blocks, as well as energy storage devices. Photo: Jürgen Lösel



Over the past few decades, the evolution of microelectronics has generated the need for multi-functional devices coupled with higher integration densities within the limited three-dimensional (3D) space in modern consumer and biomedical electronic systems. Increasing the functional complexity of electronic applications often balances between fabrication costs and manufacturing efficiency, which are affected by the methods and processes employed. This involves independent manufacturing of packages (made of e.g. soft or hard plastic and metallic materials), substrates (e.g. monocrystalline semiconductors, plastics and reinforced composites) and devices (e.g. passive devices, integrated circuits and sensors), followed by thorough sequential assembly of different components (e.g. connectors, sensors, actuators) into a full system. This is in contrast to wafer scale manufacturing of semiconductor devices, which has been used for decades as a largely parallel process to fabricate complex circuits such as processors, amplifiers, and radio frequency (RF) devices ever since integrated circuits were demonstrated. Manufactured via this route, modern microelectromechanical (MEMS) and nanoelectromechanical systems (NEMS) sit at the heart of mainstream mass-produced applications nowadays such as accelerometers, pressure sensors, ultrahigh quality factor oscillators, and spatial light modulators (SLM) in digital light processing (DLP) units. The fabrication of these essentially 3D devices are, however, severely restricted in structural design freedom owing to the entirely planar processing scheme. This scheme relies on physical and chemical properties of monocrystalline semiconductor substrates within conventional wafer scale manufacturing technologies.

As a result, conventional methods encounter manufacturing challenges once non-planar shapes are required such as cylinders, helices, and other complex geometries that are essential for capacitors, inductors, RF antennas, and magnetic devices. The electrical performance of these devices is directly related to the specific 3D geometry which in turn determines the distribution of the respective physical fields. Consequently, a variety of multimodal techniques and tools (e.g. bonding and pick-and-place) have been developed to manufacture and assemble 3D electronic components. However, incompatibilities among these techniques often complicate the fabrication process even further since these components have to be assembled separately from integrated silicon devices. This leads

to a reduction in overall integration density and subsequently increases the weight and volume of the final system. In general, 3D microelectronic fabrication processes must consider the various geometries of the final devices when realizing compact, fully integrated electronic components and systems to maintain reasonable manufacturing compatibility and complexity. Self-assembly has become a popular strategy in basic research around the world to construct nontrivial 3D structures such as optical Fresnel elements, micro vehicles and electronic devices (e.g. antennas [1], actuators, capacitors [2,3], coils [4] and sensors [5–8]) on the mesoscopic scale [9,10]. Self-assembly itself has been known for many decades to be key in creating natural and biological 3D architectures.

A set of novel wafer scale technologies have led to new origami-like MEMS and NEMS architectures [10] based on mechanically active and stimuli responsive materials which can be summarized into the class of shapeable materials technologies [11,12]. Planar patterns prepared from these materials via lithographic and thin-film methods can be released from the carrying substrate and then deployed to form 3D architectures in a way similar to how origami is assembled from a piece of paper. In contrast to this classical handmade craft, the structures created by shapeable materials technologies rely on monolithic, parallel self-reshaping principles generating complex mesoscale architectures on a wafer scale.

Self-assembly mechanisms have been exploited to form diverse 3D structures (Fig. 2) in a parallel fashion including surface tension, extrinsic forces, and intrinsic interfacial and volumetric stresses. Surface tension of various materials in the liquid phase has been extensively utilized to reorient conventional MEMS and NEMS structures, position microelectronic components, and fabricate polyhedral architectures. By applying extrinsic forces, structural buckling was studied in detail to form diverse pop-up 3D architectures. Intrinsic interfacial or volumetric stresses were successfully used to create rolled-up tubular and “Swiss-roll” architectures. In their deployed state, these essentially reshaped 2D membranes with thicknesses from nano- to micrometers experience fully integrated electronic functionalities as there is direct compatibility between shapeable materials technologies and conventional thin-film microfabrication processes (Fig. 1).

It has been shown back in 1962 [13], that electronics

need not require monocrystalline substrates to operate. The ease in fabrication and low price of thin-film electronics facilitated the fabrication of devices on amorphous rigid and even polymeric flexible substrates that have been developed by now into active matrix liquid crystalline (AMLCD), organic light emitting devices (AMOLED), and many other intriguing applications. Using a variety of deposition techniques, organic and inorganic materials can be applied to the surface of flexible and stretchable substrates through shadow masks, or by relying on printing and photolithography techniques. New amorphous semiconducting materials are involved in the development of flexible electronics based on high-performance compounds that include organic [14-16] and inorganic [17,18] semiconductors possessing, for instance, the transparency [19] required in optoelectronic applications. Once fabricated on polymeric ultrathin substrates, these devices offer the flexibility, stretchability, printability [20] and imperceptibility [20-22] for on-skin biomedical applications, such as biosensors capable of conformally wrapping a soft or irregularly shaped dynamic 3D biological surfaces. Demonstrating outstanding mechanical stability, thin-film materials are particularly attractive for 3D self-assembled microelectronics compared to monocrystalline ones. By employing substrates with a thickness in the micro- and submicrometer range many issues associated with mechanical stress on the surface could be mitigated, demonstrating the increased robustness and reliability of thin-film electronics. As a result new applications that include integrable pressure, temperature, Hall ef-

fect, and giant magnetoresistive magnetic field [20,22] sensorics have emerged over the past few years.

For self-assembled microelectronics, the compact 3D shape directly improves the form factor and thus the performance per footprint area of energy storage components such as batteries [23,24], capacitors and supercapacitors [2,3,25] and inductors [4], or provide novel features absent in the initial planar state as recently demonstrated for magnetic sensors [6]. Similar improvements were reported for optical and electrical applications when used as mechanical scaffolds to study, manipulate, and interface with biological liquids and soft tissues [7,26-30]. 3D self-assembled microelectronic devices form a new research field that is able to simplify manufacturing processes and provide novel functionalities.

In order to improve the performance of 3D energy storage devices, it is essential to use high length-to-width aspect ratio nanomembranes. Reliable and reproducible self-assembly of such nanomembranes has become, however, an increasingly challenging task as tiny fluctuations in the formation process lead to large deviations in the final shape and structure of each device. From a fundamental point of view, these deviations are triggered and amplified by a large number of spatial degrees of freedom leading to various pathways (Fig. 3) through which nanomembranes relax available potential energy during their assembly process. It was possible to overcome these issues by introducing an alternative approach that explores the magnetic field assisted assembly of 3D nanomembrane architectures [2]. By applying static and dynamic

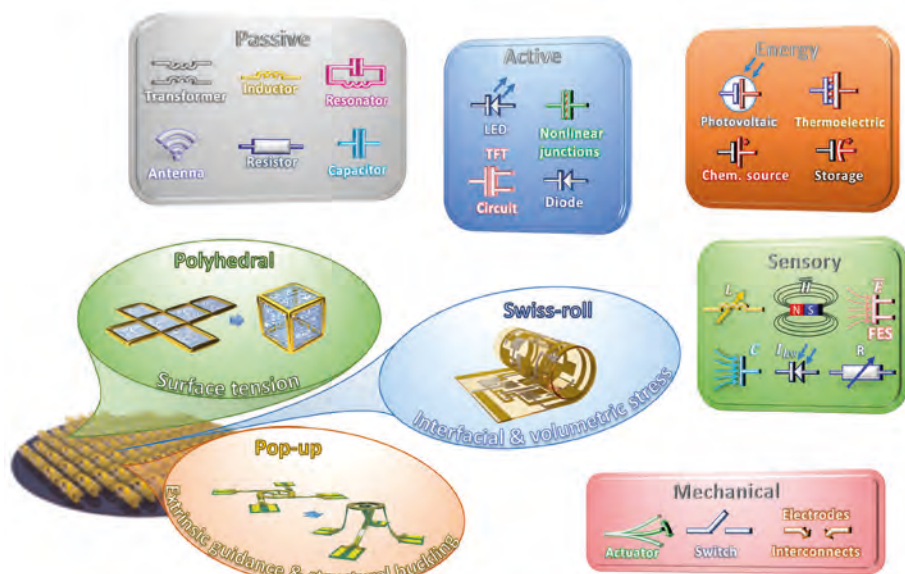


Abb. 2: Familie von selbstorganisierten 3D-Mikroelektronikgeräten aus Polyeder, Pop-up und Swiss-Roll, die im Wafer-Maßstab verarbeitet und über verschiedene Antriebsmechanismen eingesetzt werden können. Die selbstorganisierte 3D-Mikroelektronik beherbergt eine Vielzahl elektronischer Elemente mit passiven und aktiven Funktionen und ermöglicht die Interaktion mit der Außenumgebung über Sensoren und Aktoren, wobei das gesamte System von Mikroenergiequellen und Energiespeicherkomponenten gespeist werden kann. Diese Funktionalitäten werden als Dünnschichtstrukturen auf der Oberfläche der selbstorganisierten 3D-Architekturen implementiert.

Fig. 2: Family of 3D self-assembled polyhedral, pop-up and Swiss-roll microelectronic devices that are wafer scale processable and deployable via various driving mechanisms. 3D self-assembled microelectronics accommodates a variety of electronic elements, carrying passive and active functionalities, and offers interaction with external environment via sensors and actuators, where the whole system can be powered by micro energy sources and energy storage components. These functionalities are implemented as thin-film structures on the surface of the 3D self-assembled architectures.[15]

magnetic fields during assembly, high performance energy storage devices could be created demonstrating that cleverly guided micro-Origami can make a crucial difference when it comes to exploring viable technology routes towards exciting new manufacturing scenarios.

References

- [1] D. D. Karnaushenko et al., NPG Asia Mater. 7 (2015) e188.
- [2] F. Gabler et al., Nat. Commun. 10 (2019) 3013.
- [3] R. Sharma et al., Adv. Energy Mater. 4 (2014) 1301631.
- [4] D. D. Karnaushenko et al., Adv. Electron. Mater. 4 (2018) 1800298.
- [5] D. Gracias et al., MRS Proc. 1249 (2010) 1249.
- [6] D. Karnaushenko et al., Adv. Mater. 27 (2015) 6582.
- [7] S. M. Weiz et al., Adv. Biosyst. 2 (2018) 1700193.
- [8] M. Medina-S. et al., Proceedings 1 (2017) 840.
- [9] G. M. Whitesides, Science (80-.). 295 (2002) 2418.
- [10] J. Rogers et al., MRS Bull. 41 (2016) 123.
- [11] D. Karnaushenko et al., Adv. Mater. Technol. 4 (2019) 1800692.
- [12] D. Karnaushenko et al., Adv. Mater. (2019) DOI 10.1002/adma.201902994.
- [13] P. Weimer, Proc. IRE 50 (1962) 1462.
- [14] H. Sirringhaus, Adv. Mater. 26 (2014) 1319.
- [15] A. R. Jalil et al., Adv. Mater. 28 (2016) 2971.
- [16] V. K. Bandari et al., Beilstein J. Nanotechnol. 8 (2017) 1277.
- [17] N. Münzenrieder et al., Adv. Electron. Mater. 2 (2016) 1.

- [18] D. Karnaushenko et al., Adv. Mater. 27 (2015) 6797.
- [19] G. A. Salvatore et al., Nat. Commun. 5 (2014) 2982.
- [20] M. Melzer et al., Nat. Commun. 6 (2015) 6080.
- [21] G. S. Cañón Bermúdez et al., Sci. Adv. 4 (2018) eaao 2623.
- [22] M. Melzer et al., Adv. Mater. 27 (2015) 1274.
- [23] J. Deng et al., Adv. Energy Mater. 6 (2016) 1600797.
- [24] S. Reineke et al., Nature 459 (2009) 234.
- [25] Z. Liu et al., Adv. Mater. 31 (2019) 1.
- [26] C. S. Martinez-Cisneros et al., Nano Lett. 14 (2014) 2219.
- [27] B. Koch et al., Nano Lett. 15 (2015) 5530.
- [28] V. Magdanz et al., Adv. Mater. 28 (2016) 4084.
- [29] D. Grimm et al., Nano Lett. 13 (2013) 213.
- [30] M. Medina-Sánchez et al., Nano Lett. 16 (2016) 555.

Funding

Leibniz Association

German Science Foundation (DFG) grant HO 1483/64, KA5051/1-1

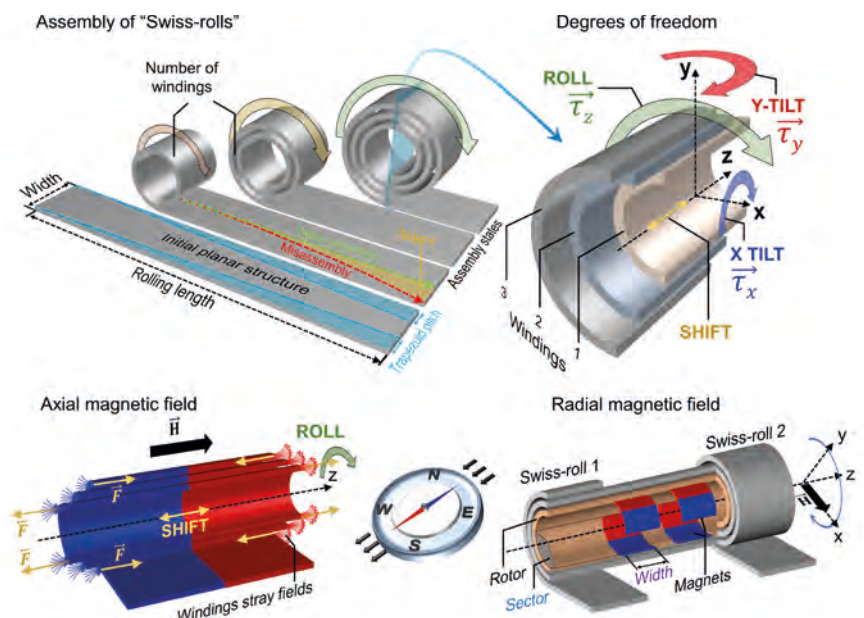
DFG Research Group FOR1713.

Cooperations

University Osaka (Japan), ETH Zürich (Switzerland), University of Sussex (UK), Universität Linz (Austria), HZDR (Germany), TU Dresden (Germany), Universität Bonn (Germany), Universität Stuttgart (Germany), University Hongkong (Hongkong), University Madison Wisconsin (USA), University Twente (Netherlands).

Abb. 3. Schematische Darstellung der Swiss-Roll-Anordnung, die mit einer anfänglich planaren Struktur einer bestimmten Form beginnt. Freiheitsgrade, die für die „Swiss-Roll“-Architektur während des Montageprozesses verfügbar sind, wirken sich stark auf die Stabilität des Prozesses aus, bei dem ein externes Magnetfeld deren Anzahl verringern und die Stabilität erhöhen kann. Zum Beispiel stabilisiert ein axiales Magnetfeld die Selbstorganisation, indem es magnetische Strukturen im Raum ausrichtet, ähnlich einem Kompassnadel, der sich am Erdmagnetfeld orientiert. Während das radiale dynamische (rotierende) Magnetfeld den Magnetkern der Nanomembran wie ein Rotor abrollen kann, lädt es eine Uhrfeder auf und richtet die Geometrie aus, wenn die Struktur eng wird. [2]

Fig. 3. Schematics of the “Swiss-roll” assembly which starts with an initially planar structure of a specific shape. Degrees of freedom available for “Swiss-roll” architecture during the assembly process strongly affect the stability of the process, where an external magnetic field can reduce their number and enhance stability. For instance, axial magnetic field stabilizes the self-assembly by orienting magnetic structures in space, similar to a compass arrow oriented by the Earth magnetic field. While the radial dynamic (rotating) magnetic field can roll magnetic core of the nanomembrane like a rotor charges a clock spring, aligning the geometry when the structure gets tight. [2]



Thermoelectric properties of recycled silicon sawing waste

Ran He, Wieland Heyn, Felix Thiel, Nicolás Pérez, Christine Damm, Darius Pohl¹, Bernd Rellinghaus¹, Christian Reimann², Maximilian Beier², Jochen Friedrich², Hangtian Zhu³, Zhifeng Ren³, Kornelius Nielsch and Gabi Schierning

Zusammenfassung

Thermoelektrische Materialien wandeln Wärme-flüsse in elektrische Energie. Sie gelten daher als potenzieller Akteur bei der Abwärmenutzung. Thermoelektrische Materialien sollten jedoch sowohl effizient als auch nachhaltig sein und daher keine seltenen Elemente verwenden. Unter allen Klassen bekannter thermoelektrischer Materialien erfüllt Silizium diese Kriterien.

Hier berichten wir über die thermoelektrischen Eigenschaften von Siliziumsägeabfällen, die aus der Siliziumwaferherstellung recycelt werden. Wir erhalten hohe Leistungsfaktoren von $32 \text{ mWcm}^{-1} \text{ K}^{-2}$ bei 1273 K

mit sechs Prozent Phosphordotierung im Silizium-Kristall. Diese Ergebnisse legen nahe, dass recyceltes Silizium aus Industrieabfällen für thermoelektrische Anwendungen geeignet ist.

Abstract

Thermoelectric materials convert heat fluxes into useable electricity. They are therefore considered as a potential player in waste heat harvesting. However, large-scale-applicable thermoelectric materials should be both, efficient and sustainable, hence not make use of scarce elements. Among all classes of known thermoelectric materials, silicon fulfills these criteria. Here we report the thermoelectric properties of silicon sawing wastes recycled from silicon wafer manufacturing. We obtain high power factors of $32 \text{ mWcm}^{-1} \text{ K}^{-2}$ at 1273 K with six percent phosphorus substitution in the silicon crystal. Our work suggests the large-scale thermoelectric applicability of recycled silicon that would otherwise contribute to tons of industrial waste.

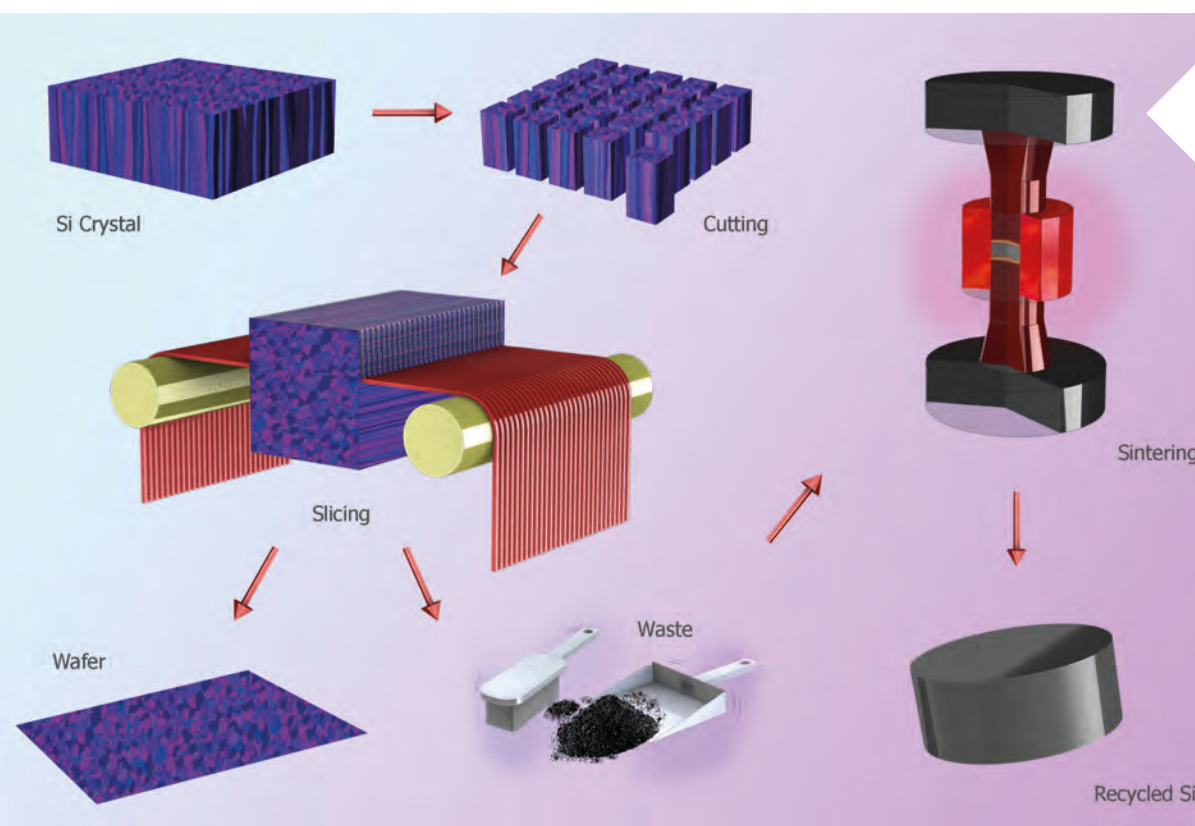


Abb. 1: Waferherstellungsschritte und Siliziumabfallrecycling. Figure and figure caption reproduced with permission from Ref. [1], R. He et al., *Journal of Materiomics* 5, 15-33 (2019), © 2018 The Chinese Ceramic Society. Production and hosting by Elsevier B.V.

Fig. 1: Wafer manufacturing steps and waste silicon recycling. Figure and figure caption reproduced with permission from Ref. [1], R. He et al., *Journal of Materiomics* 5, 15-33 (2019), copyright The Chinese Ceramic Society, 2019.

Thermoelectric waste heat harvesting

The thermoelectric (TE) effects describe the reversible conversion of heat fluxes into electrical fluxes. Thermoelectric (waste) heat harvesting is characterized by the conversion of a heat flux into useable electricity – this becomes an attractive technology especially in the case that the heat source is a byproduct of another technology. In that case, by adding a thermoelectric generator (TEG) to recover parts of this waste heat, the over-all efficiency of the underlying process can be improved. Thermoelectric Peltier coolers convert an electrical flux into a heat flux in a way that active cooling can be provided with an extremely high degree of reliability, cycling stability and precision. To place these two applications of thermoelectricity, the mature industrial application is the Peltier cooling, while waste heat harvesting has an enormously prospective potential for future application. Compared to other waste heat harvesting technologies, TE devices are special due to their solid-state nature. They are reliable, noiseless, scalable, and maintenance free. In outer-space, radioisotope thermoelectric generator (RTG) have powered space missions for decades without a single failure. The drawbacks of TEGs for terrestrial application are currently a relatively low efficiency at too high costs. Further, commercially available TE devices are mostly based on scarce elements or such that impose a risk for health or environment like tellurium, antimony, lead, and germanium. For large-scale waste heat harvesting, this is a drawback that fundamentally limits the application: It is simply not feasible to place TEGs that contain such elements at remote places or in harsh industrial environments for waste heat recovery. The risk of losing a module by unforeseen accidents cannot be completely excluded, with an extremely critical impact on the environment. Therefore, TEG applications are today restricted only to niche markets where reliability overweighs all, environmental concerns, a too low conversion efficiency, and too high costs.

Sustainable raw materials for large scale thermoelectric application

In order to widely apply TE waste heat harvesting, it is crucially important to substitute today's critical elements in TE materials by an environmentally sustainable alternative, and at the same time, to boost the

TE performances of TE materials or to significantly reduce their costs. This is the motivation of a material's development project in which waste products of semiconductor industry are being re-used, to a certain degree refurbished, to make them efficient thermoelectric materials.

The global photovoltaic module production capacity was over 100 GW in 2017, and the Si-wafer based photovoltaic technology accounted for more than 90% of the total production of all absorber materials. Hereby, especially the wafering produces a waste product of still high quality: Cutting silicon wafers from the single crystalline or poly-crystalline ingots relies on either a loose abrasive cutting technology where silicon carbide (SiC) based sawing slurries are used together with a moving steel wire; or a fixed abrasive cutting technique where resin-bonded or -plated diamonds are fixed directly on the moving steel wire. The thickness of a typical wafer (~300 µm) and the diameter of a typical sawing wire (~100 µm) already suggest that approximately one third of the annual production of photovoltaic modules ends up in the waste. In total, more than 100,000 tons of this Si kerf is generated worldwide annually, and due to increasing installations of photovoltaics, this has an upwards trend. Taking into account an initial price of about 15-20 US\$ per kg for the originally used high-quality Si feedstock used for crystal growth it can be stated, that Si material of around 2 billion US\$ per year is grinded down to small Si particles in form of the Si kerf. Due to the incorporation of impurities during the wafering process, this Si kerf cannot be recycled for photovoltaics. Aside the abrasives like SiC or diamond particles, metals like iron (Fe) from the steel wire, and usually carbon from the sawing slurry are part of the kerf.

Since approximately one decade, silicon is investigated as desirable sustainable source materials for thermoelectric waste heat harvesting. It shows an impressive potential for being an applicable TE material because of its low price, excellent chemical and mechanical stability, non-toxicity, and high industrial compatibility. As a widely studied semiconductor, both n- and p-type properties were realized in Si, which greatly facilitate the engineering process in building TE devices. In terms of TE properties, excellent power factors were realized with phosphorus (P)-doping in a wide temperature range from 500 to 900 °C. Suppressing the thermal conductivity of Si is of uttermost importance to enhance its TE performances, which can be by

designing the nano- and microstructure of the material to impede heat transport by phonons. For instance, nano-grained bulk structures showed the potential in intensifying the phonon scattering with an improved TE figure of merit value of $zT \sim 0.7$ reported in n-type Si at ~ 1200 K.

Given both, the enormously high amount of waste Si production worldwide, and the prospective properties of Si as thermoelectric waste heat harvesting material, it is therefore a desirable attempt to utilize waste silicon for thermoelectricity. The schematics of silicon wafer manufacturing and its further utilization for thermoelectricity is shown in Fig. 1.

Thermoelectric transport properties of re-used silicon sawing wastes

In comparison to a re-use scenario in photovoltaics, thermoelectricity hereby benefits from the fact that typically extremely high doping levels are necessary for good thermoelectric performance, much higher than in photovoltaics. Due to these high doping levels, it is possible to overcompensate the amount of metallic impurities that were incorporated during the sawing process. We demonstrate this by a doping study, using the Si kerf as is, hence without any additional purification. We directly translate the recycled Si into TE materials using techniques that are industrially mature such as ball milling and mechanically alloying and spark plasma sintering. We then characterize both, its microstructure and its thermoelectric performance in dependence of the added concentration of phosphorus (P) for n-type doping.

The Si obtained from recycling of the sawing waste was originally produced by a European wafer manufacturer who used the loose abrasive technique based on SiC-

particles and Polyethylene-glycol as coolant. The as-obtained Si batches after recycling are mixtures of several elements/compounds. Depending on the detailed recycling process technology, typically the mixtures contain Si (70-85 Wt.%), SiC (15-30 Wt.%), metals (up to 5 Wt.%), and oxidized silicon or metal phases. In this study, the Si recycling batch consists of 78 Wt.% Si and 22 Wt.% SiC, which converts to mole ratio of 72% Si to 28% SiC, and to volumetric ratio of 83% Si to 17% SiC. Phosphorus (P) was chosen as dopant to tune the carrier concentration. To study the influence of dopant atoms on the thermoelectric properties we selected amounts of P as 0.1 at.%, 0.2 at.%, 1 at.%, 2 at.%, 3 at.%, 6 at.%, 8 at.%, and 10 at.%. As a reference, we also synthesized a pure Si sample with 2 at.% P substitution. Fig. 2 shows a typical microstructure as obtained in the sintered and P-doped slurries.

TEM results indicate that Si and SiC have grain sizes of ~ 500 to 800 nm. Moreover, a considerable amount of precipitates are also observed. These precipitates typically possess sizes of 10 to 50 nm. Electron diffraction patterns of these precipitates point to phosphorous crystals. Besides, the presence of O and Fe in the Si matrix lead to more complex compounds. The temperature-dependent TE performances of the compositions in this study are shown in Fig. 3. Upon the addition of P, electrical resistivity decreases dramatically. But it is obvious that the resistivity of the 2 at.% P-doped silicon is much lower than that of the recycled Si. This is due to the presence of SiC that scatters charge carriers as well as the decreased amount of active material and therewith concentration. As expected, the Seebeck coefficients are lower with higher amount of carrier density. This is in good accordance with the single parabolic band assumption. The combined electrical resistivity and Seebeck coefficient yields the power

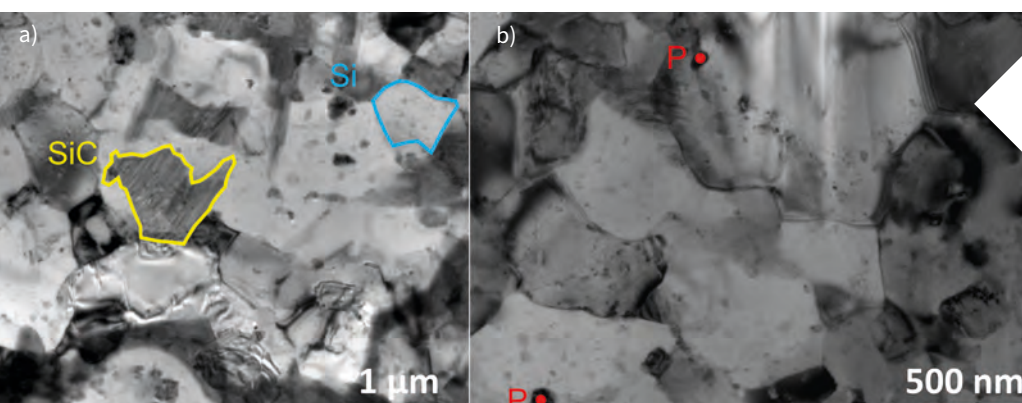


Abb. 2: TEM-Charakterisierung der recycelten Si-Mischung mit 10 at.% P-Substitution. a) Morphologie von Si- und SiC-Körnern, b) die Morphologie von P-Ausscheidungsphasen. *Figure and figure caption reproduced with permission from Ref. [1], R. He et al., Journal of Materiomics 5, 15-33 (2019), © 2018 The Chinese Ceramic Society. Production and hosting by Elsevier B.V.*

Fig. 2: TEM characterization of the recycled Si mixture with 10 at.% P substitution. a) Morphologies of Si and SiC grains, b) the morphologies of P precipitates. *Figure and figure caption reproduced with permission from Ref. [1], R. He et al., Journal of Materiomics 5, 15-33 (2019), copyright The Chinese Ceramic Society, 2019.*

factor, PF . Its peak value of PF at 1073 K reaches $\sim 28 \mu\text{W cm}^{-1} \text{K}^{-2}$ for the recycled Si with 2 at.% P substitution, compare to $\sim 37 \mu\text{W cm}^{-1} \text{K}^{-2}$ of the 2 at.% P-doped reference Si. By further increasing the temperature to 1273 K, we obtain a higher PF of $\sim 32 \mu\text{W cm}^{-1} \text{K}^{-2}$ with 6 at.% P substitution, which is comparable to doped SiGe alloys. The value of the thermal conductivity, κ , decreases with higher concentration of P. Note that the samples with 0.1% and 0.5% doping have abnormally low κ . This is because of their relative low densities. By subtracting the electronic thermal conductivity (κ_e) using the Wiedmann-Franz law $\kappa_e = LT\rho$, where L is the Lorenz number determined from single parabolic band (SPB) model with an approximate equation, we plot the sum of lattice and bipolar thermal conductivity ($\kappa_L + \kappa_{bip}$). Clearly, the reduction of κ originates from the decreased κ_L , with the possible mechanisms being an enhanced electron-phonon interaction, which has been widely proven in Si. Finally, we obtain a peak zT value of ~ 0.33 in recycled Si with 6 at.% P substitution at 1273 K. The obtained peak zT is comparable to that of Si with 2 At.% P doping.

Conclusion and Outlook

Obviously, the material used for this study was not yet further improved by any means. There were neither attempts to reduce the amount of oxygen or SiC, nor the metallic impurities. Obviously, there is still an enormous potential to improve these Si kerfs and demonstrate their feasibility for use of thermoelectric waste heat harvesting. Considering the high abundance of Si from recycled sawing wastes as well as the industrial exigency to turn these “waste” products profitable, we conclude that the recycled Si an applicable TE material.

Acknowledgements

The authors thank R. Uhlemann in IFW Dresden for support in the design of the graphics.

References

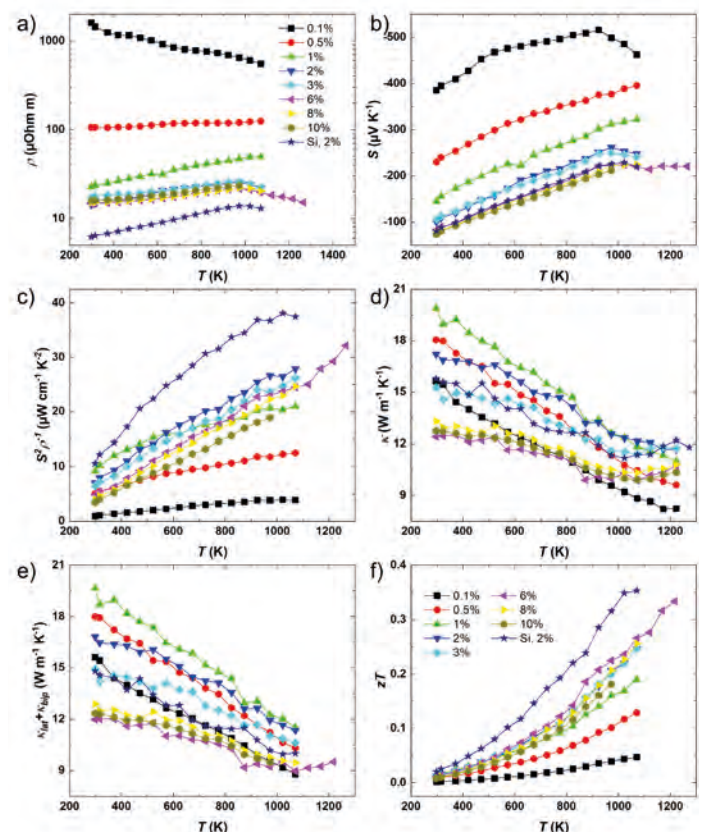
[1] Ran He et al. Journal of Materiomics 5, 15-33 (2019).

Cooperations

- 1) Dresden Center for Nanoanalysis, Technische Universität Dresden, Germany
- 2) Fraunhofer Institut für Integrierte Systeme und Bauelementetechnologie, Erlangen, Germany
- 3) Department of Physics and TcSUH, University of Houston, USA.

Abb. 3: Temperaturabhängige thermoelektrische Eigenschaften, a) elektrischer Widerstand, b) Seebeck-Koeffizient, c) Leistungsfaktor, d) Wärmeleitfähigkeit, e) Wärmeleitfähigkeit des Gitters und bipolare Wärmeleitfähigkeit und f) zT des recycelten Si mit 0,1 at.%, 0,5 at.%, 1 at.%, 2 bei.%, 3 at.%, 6 at.%, 8 at.% und 10 at.% P Substitution. Die TE-Eigenschaften von 2 at.% P-substituiertem Si werden ebenfalls gezeigt. Figure and figure caption reproduced with permission from Ref. [1], R. He et al., Journal of Materiomics 5, 15-33 (2019), © 2018 The Chinese Ceramic Society. Production and hosting by Elsevier B.V.

Fig. 3: Temperature dependent thermoelectric properties, a) electrical resistivity, b) the Seebeck coefficient, c) power factor, d) thermal conductivity, e) lattice plus bipolar thermal conductivity, and f) zT of recycled Si with 0.1 at.%, 0.5 at.%, 1 at.%, 2 at.%, 3 at.%, 6 at.%, 8 at.%, and 10 at.% P substitution at Si. The TE properties of 2 at.% P-substituted Si is also plotted. Figure and figure caption reproduced with permission from Ref. [1], R. He et al., Journal of Materiomics 5, 15-33 (2019), copyright The Chinese Ceramic Society, 2019.





FORSCHUNGSGEBIET 3:

Quantenphänomene im Nanomaßstab

RESEARCH AREA 3:

Quantum Effects at the Nanoscale

Quantenphänomene im Nanomaßstab

In diesem Forschungsbereich beschäftigen wir uns mit Materialien und Strukturen deren quantenmechanischen Effekte auf ihre Nanoskaligkeit zurückzuführen sind. Dies sind sehr dünne Filme, Oberflächen und Grenzflächen, Quantenpunkte, photonische Kristalle und molekulare Nanostrukturen wie Fullere, leitende Polymere und organische Halbleiter. Im Bereich der Nanophotonik bearbeiten wir grundlegende Themen wie die Erzeugung von Einzelphotonen und verschränkten Photonenpaaren mit Halbleiter-Nanomaterialien sowie starke Licht-Materie-Wechselwirkungen im Quantenbereich. Anwendungsorientierte Fragestellungen betreffen die Herstellung moderner photonischer Bauelemente wie Quanten-Leuchtdioden, aufgerollte optische Mikrokavitäten und 3D-Photonische Kristalle. Das Ziel dieser Forschung ist die Realisierung einer integrierten optoelektronischen Plattform zur Erzeugung komplexer photonischer Funktionalitäten.

Auf der Nanoskala können auch völlig neue physikalische Eigenschaften entstehen, etwa an Oberflächen und Grenzflächen topologischer Isolatoren. Dort ist der Spin von Oberflächenelektronen an ihren Impuls gebunden - eine Eigenschaft, die im Kontext der Spintronik interessant ist. Die Arbeit in diesem Bereich ist ein weiteres Beispiel für die Interdisziplinarität unserer Forschung. In enger Kooperation wirken experimentelles Knowhow und theoretische Expertise zusammen, um neue topologische Isolatoren zu erforschen und ihre Oberflächenzustände und Transporteigenschaften zu verstehen.

Quantum Effects at the Nanoscale

In this Research Area we address materials and structures with quantum mechanical effects that are due to their nanoscale. These are very thin films, surfaces and interfaces, so called heterostructures formed by thin films of different composition, quantum dots, photonic crystals and molecular nanostructures like fullerenes, conducting polymers and organic semiconductors.

In the field of nanophotonic the research work at IFW aims to explore several long-standing questions and challenges. Our work approaches fundamental topics: such as the generation of single photons and entangled photon pairs with semiconductor nanomaterials, the strong light-matter interactions in the quantum regime. More applied questions concern the fabrication of advanced photonic devices such as quantum light emitting diodes, rolled-up optical microcavities and 3D photonic crystals. When combined together, this multifaceted research could enable the realization of complex photonic functionalities with an integrated opto-electronic platform.

At the nanoscale also entirely new physical properties may emerge, for instance at surfaces and interfaces of topological insulators where the spin of surface electrons is locked to their momentum, a property that is interesting in the context of spintronics. Work at the IFW Dresden in this area is a nice example of a very interdisciplinary research effort, combining the available experimental and theoretical expertise to investigate topologically protected surface states and transport properties, again combining synthesis, theory and experiment.

Entanglement swapping with semiconductor-generated photons violates Bell's inequality

Michael Zopf, Robert Keil, Yan Chen, Jingzhong Yang, Disheng Chen, Fei Ding and Oliver G. Schmidt

Zusammenfassung

Kommunikation spielt in Wirtschaft und Gesellschaft eine zentrale Rolle. Die derzeit bei der Datenübertragung eingesetzten Verschlüsselungstechniken sind jedoch abhörbar. Die Quantenmechanik eröffnet neue Wege zur sicheren Kommunikation: Dabei kommen Lichtteilchen (Photonen) zum Einsatz, die miteinander verschränkt sind. Das heißt, sie stehen selbst über weite Entfernungen in Verbindung. Jeder Versuch, sie abzufangen, hinterlässt Spuren, die ein unerkanntes Abhören unmöglich machen. Einzelne Photonen können über lange Strecken jedoch leicht verloren gehen.

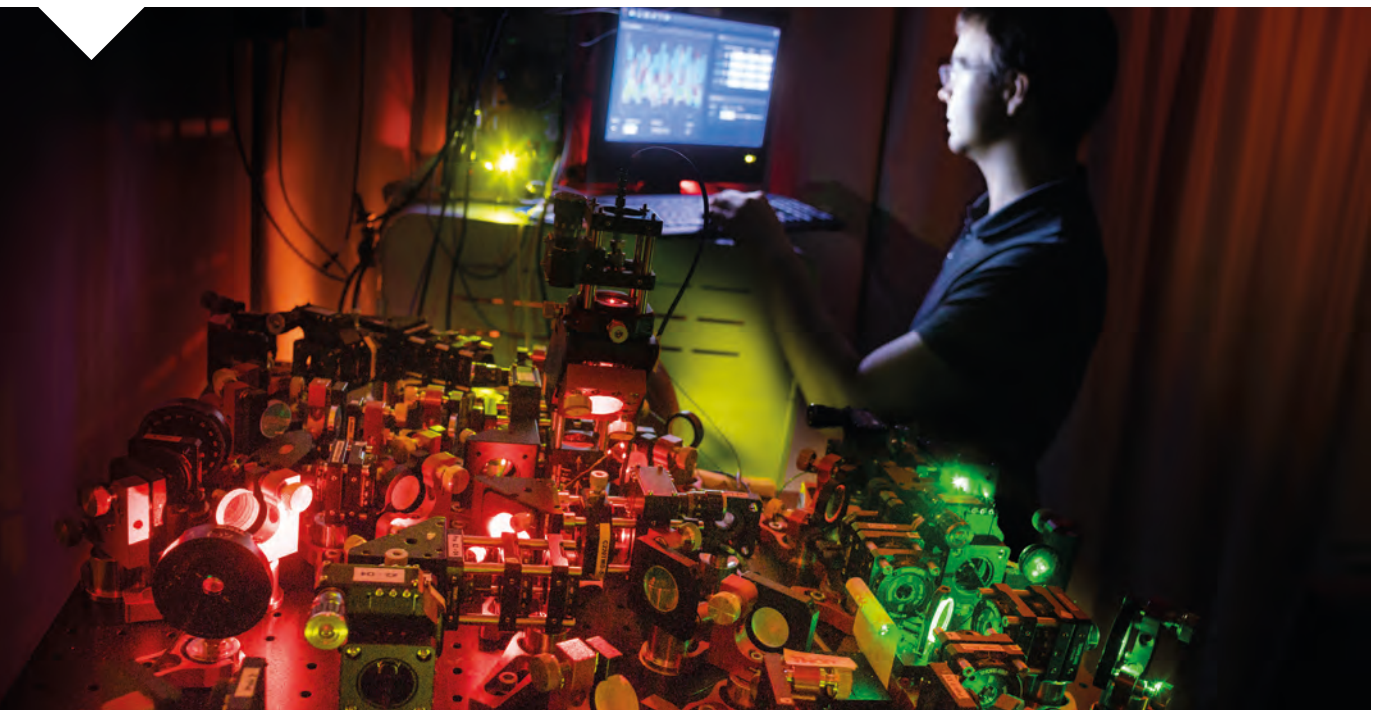
Es ist uns gelungen, die Verschränkung zwischen Photonen weiterzugeben, ähnlich einem Staffellauf. Erstmals sind dabei Halbleiter-Lichtquellen zum Einsatz gekommen.

Abstract

Secure communication plays a key role in modern economy and society. Current data transmissions, however, can be intercepted and deciphered unnoticed. Quantum mechanics opens up new opportunities for truly secure communication, using entangled light particles (photons) as information carriers. Entanglement means, that they are tightly connected even over long distances. Any interception attempt leaves clear traces rendering undetected eavesdropping impossible. However, single photons can easily be lost over long distances. We have succeeded in passing on the entanglement between individual photons, similar to a relay race, using semiconductor light sources which are compatible to existing micro-chip technology.

Abb. 1: Versuchsaufbau für den Verschränkungsaustausch zwischen Photonenpaaren. Die Halbleiter-Photonenquelle befindet sich in einem Kryostaten unterhalb des abgebildeten optischen Tisches und wird mittels eines Lasers angeregt, die emittierten Photonen mittels der Aufbauten zum Verschränkungsaustausch geleitet und anschließend analysiert. Foto: Jürgen Lösel

Fig. 1: Experimental setup for the entanglement swapping. The entangled photon pairs are generated by optically exciting the semiconductor quantum light source, located in a cryostat below the shown optical table. The emitted photons are guided through the swapping experiment and subsequently analyzed. Photo: Jürgen Lösel



Introduction

Semiconductor light sources have revolutionized science and technology since laser diodes and vertical-cavity surface-emitting lasers (VCSELs) arrived in the 1960s. Quantum mechanics lies at the roots for these devices, yet quantum states of light have only been studied extensively in recent decades in their own right. Semiconductor sources can now emit single photons and entangled photons on demand, holding great potential for applications in quantum cryptography, quantum communication, quantum metrology, and quantum computation. The next step towards building quantum networks is to transfer entangled states between distinct pairs of photons. This entails substituting the pairwise entanglement in two-photon states with entanglement between photons from different pairs. The first experiment to do this [1] used a nonlinear optical crystal for the entangled-photon generation. The efficiency and thus scalability of these sources are however fundamentally limited owing to non-deterministic emission statistics. Semiconductor quantum dots (QD) by contrast are able to generate entangled photon pairs on-demand. QDs are nano-scaled islands of a semiconductor with a small energy band gap embedded in another semiconductor with a larger band gap. Such a hetero-nanostructure exhibits discrete energy levels and spectral features comparable to an atom. Until recently, QDs have suffered from low brightness and poor optical quality, blocking the path for quantum information applications. Improvements of the past three years with major contributions from the IFW Dresden have finally overcome these limitations. Highly coherent and strongly entangled photons [2] can now be generated with high brightness [3] and reproducibility [2] from QDs. In this work we demonstrate, for the first time, entanglement swapping between polarization-entangled photons emitted by a semiconductor QD, marking a milestone towards semiconductor-based long-distance quantum communication [4].

Experimental entanglement swapping

A simplified sketch of the entanglement swapping setup is shown in Fig. 2: Two pairs of polarization-entangled photons are consecutively emitted (emissions 1 and 2) after optically exciting a single semiconductor QD. One photon from each pair is directed to

a joint Bell-state measurement (BSM), which, upon success, establishes entanglement of the remaining photons sent to two receivers (Alice and Bob).

The bright sources of entangled photons in our experiment are GaAs/AlGaAs QDs, located in a cryostat at 4 K. The QDs are embedded in a thin membrane with a rear gold mirror which is bonded to a gallium phosphide solid immersion lens. This design offers a high photon extraction efficiency while preserving a high single-photon purity and entanglement degree [3]. To generate polarization-entangled photon pairs, we employ a resonant excitation scheme to deterministically create a biexciton in a single QD [2]. The biexciton, a quasi-particle consisting of two electrons and two holes confined in the QD, decays under the cascaded emission of a single photon pair, the biexciton (XX) and the exciton (X) photon. We use two optical pulses separated by 2 ns to generate two consecutive pairs of photons. Each pair is in the polarization-entangled Bell state $|\Phi^+\rangle$ in the respective emission $i = 1, 2$:

$$|\Phi^+\rangle_i = (|H_X H_{XX}\rangle + |V_X V_{XX}\rangle)/\sqrt{2}$$

with H and V representing horizontal and vertical polarization of the rectilinear basis. Second-order autocorrelation measurements reveal, that under resonant excitation, both X and XX emission show high single-photon purities of $g_X^{(2)}(0) = 0.0041 \pm 0.0003$ and $g_{XX}^{(2)}(0) = 0.0050 \pm 0.0005$. The entangled-photon pairs 1 and 2 are separated using a non-polarizing beam splitter and time-gated single-photon detection. The XX and X photons from each pair are split apart using dichroic optical filters. At this stage, the four-photon state $|\alpha\rangle$ is a product of the states from emissions 1 and 2.

It can be rewritten into products of Bell states between the X and XX photons:

$$|\alpha\rangle = |\Phi^+\rangle_1 |\Phi^+\rangle_2 = (|\Phi^+\rangle_X |\Phi^+\rangle_{XX} + |\Phi^-\rangle_X |\Phi^-\rangle_{XX} + |\Psi^+\rangle_X |\Psi^+\rangle_{XX} + |\Psi^-\rangle_X |\Psi^-\rangle_{XX})/2$$

with the four polarization Bell states

$$\begin{aligned} |\Phi^\pm\rangle &= (|HH\rangle \pm |VV\rangle)/\sqrt{2}, \\ |\Psi^\pm\rangle &= (|HV\rangle \pm |VH\rangle)/\sqrt{2}. \end{aligned}$$

Projecting this four-photon state $|\alpha\rangle$ to a Bell state between photons XX1 and XX2 will in turn result in a Bell state shared by the previously uncorrelated X1

and X2. The projection of the state $|\Phi^+\rangle$ is performed by the following BSM: First, photons XX1 and XX2 are sent to interfere on a non-polarizing beam splitter. The photons then pass through an H- or a V-oriented polarizer in each beam splitter output and single-mode fibers deliver the photons to superconducting nanowire single-photon detectors (SNSPDs). Successful interference indicated by simultaneous detection events at both SNSPDs now leaves the two remaining photons X1 and X2 in the Bell state

$$|\Phi^+\rangle_{AB} = (|HV\rangle \pm |VH\rangle) / \sqrt{2},$$

sent to Alice and Bob for measurement. Subsequent arrangement of a quarter-wave plate, half-wave plate (HWP), polarizer, and SNSPD allows for projection on any desired polarization state.

Successful entanglement swapping relies on high entanglement degrees of the initial photon pairs and on high photon indistinguishability I of the XX photons sent to the BSM. The degree of entanglement can be quantified by the entanglement fidelity f_i (emission $i = 1, 2$) which expresses the resemblance of the measured state to a maximally entangled Bell state. The fidelity f_i can be deduced from the density matrix ρ_i of the two-photon polarization state of the respective pair, which in turn can be reconstructed from polarization measurements in a set of 16 polarization base combinations. For both consecutively emitted photon pairs we obtain high degrees of entanglement with fidelities of $f_1 = 0.9369 \pm 0.0004$ (emission 1) and $f_2 = 0.9267 \pm 0.0004$ (emission 2) to the Bell state $|\Phi^+\rangle$. The indistinguishability I of the XX photons can be deduced from the two-photon interference visibility.

Here, both XX photons enter an unbiased beam splitter simultaneously from different input ports. If the photons are indistinguishable, quantum interference occurs and both photons always exit the beam splitter together at one exit port. The photon polarization at one input is then changed by a HWP, rendering the photons distinguishable. Distinguishable photons however exit the beam splitter randomly. From the visibility of the observed quantum interference, quantified by coincidence counts from both SNSPDs at the BSM, we extract photon indistinguishabilities of $I = 0.569 \pm 0.009$ which directly specifies the success probability of the BSM in the entanglement swapping experiment.

Now, the actual entanglement swapping shall be observed: As a control measurement, the photon state shared by Alice and Bob is first investigated without considering the BSM. The density matrix ρ_{mix} extracted from the quantum state tomography is shown in Fig. 3a. As expected, the photons X1 and X2 show the signature of a statistical mixture of polarization states, with a fidelity of $f_{mix} = 0.9960 \pm 0.0004$ to the completely mixed state $\frac{1}{4} \mathbb{1}$. Now the entanglement is swapped from the initial photon pairs to the photons received by Alice and Bob, as established by coincidences at the BSM. In order to increase the chance for a successful BSM and thus entanglement swapping, we employ temporal post selection of BSM detection events, at the expense of the total rate of heralding events. The obtained density matrix ρ_{AB} shown in Fig. 3b closely resembles the maximally entangled Bell state $|\Psi^+\rangle$. The fidelity of $f_{AB} = 0.81 \pm 0.04$ clearly surpasses the classical limit of 0.5 and therefore testifies to the successful swapping of the entangled state.

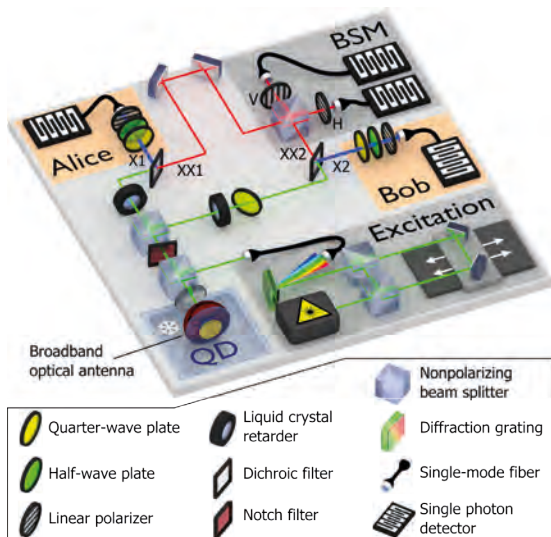


Abb. 2: Schematischer Versuchsaufbau für den Verschränkungstausch. Ein schmalbandiger Laser (Excitation) regt die Halbleiter-Lichtquelle (QD), die sich in einem Kryostaten befindet. Die emittierten Photonen werden separiert, der Verschränkungstausch erfolgt durch die Bell-Messung (BSM) und wird mittels Polarisations-Analysatoren bei 'Alice' und 'Bob' nachgewiesen.

Fig. 2: Sketch of the experimental setup for the entanglement swapping. A narrowband laser (Excitation) excites the semiconductor photon source (QD), located in a cryostat. The emitted photons are separated and the entanglement swapping is performed using a Bell state measurement (BSM) and verified using polarization analyzers located at 'Alice' and 'Bob'.

Another confirmation for the non-local nature of the generate state shared by X1 and X2 is the Bell parameter S , as used in the CHSH Bell inequalities. For the post selected detection events, we obtain a Bell parameter $S = 2.28 \pm 0.13$, which clearly violates the CHSH and Bell inequalities, $S \leq 2$, by more than 2 standard deviations. Assuming perfect indistinguishability, it reaches $s_{max} = 2.47$.

Conclusion

In conclusion, we have realized the first entanglement swapping based on photons from a quantum dot, laying the foundations for scalable semiconductor based quantum networks. Therefore, the swapping of entanglement with photons from distant emitters or the realization of multiphoton entanglement comes into reach. For practical application in quantum communication systems, further efforts should be spent on improving the photon indistinguishability, entanglement fidelity, and source brightness. These stringent requirements can be achieved, e.g., by integrating quantum dots into microcavities. Applying electric fields in QD integrated diode structures may further decrease photon dephasing. Furthermore, the indistinguishability of photons from distant emitters can be ensured using integrated strain tuning platforms.

References

- [1] J.-W. Pan et al., Phys. Rev. Lett. 80, 3891-3894 (1998)
- [2] R. Keil et al., Nat. Commun. 8, 15501 (2017)
- [3] Y. Chen et al., Nat. Commun. 9, 2994 (2018)
- [4] M. Zopf et al., Phys. Rev. Lett. 123, 160502 (2019)

Funding

- BMBF-Projekt Q.com
- BMBF-Projekt Q.Link.X
- ERC starting grant QD-NOMS (Fei Ding)

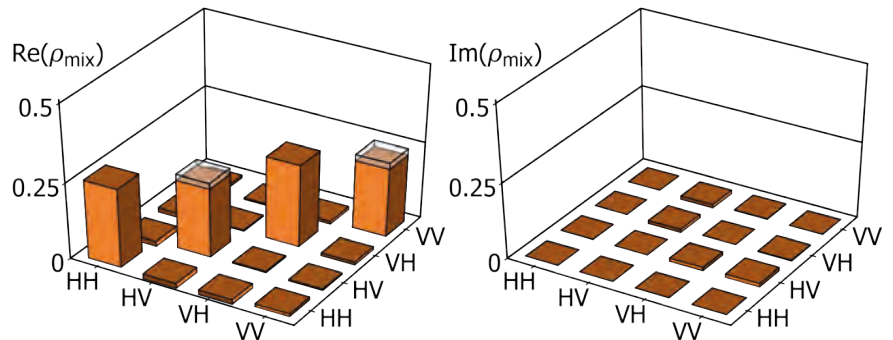
Cooperation

Leibniz-Univ. Hannover, Germany.

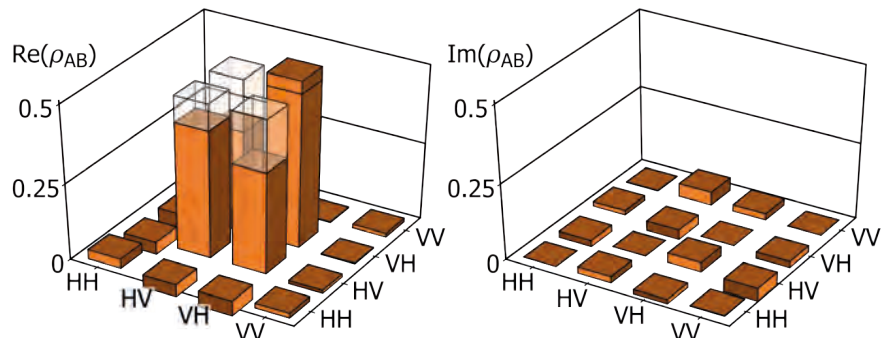
Abb. 3: Dichte-Matrix des Zwei-Photonen-Polarisationszustands. Ohne den Verschränkungsaustausch in (a) weisen die Photonen keinerlei Korrelation auf, die Dichtematrix entspricht der Einheitsmatrix. Mit Verschränkungsaustausch in (b) ergibt sich ein völlig anderes Bild, die Dichtematrix entspricht der eines verschränkten Zustandes.

Fig. 3: Density matrix of the two-photon polarization state. Without the entanglement swapping in (a), the photons show no correlation, indicated by a unity matrix. After the successful swapping shown in (b), however, the density matrix shows the clear signature of a strongly entangled state.

(a) Without BSM (no swapping)



(b) With BSM (entanglement swapping)



Nernst Effect in Quantum Materials

A. Thomas, C. Hess, K. Geishendorf, C. Wuttke, F. Caglieris, S. Sykora, F. Scaravaggi, A. U. B. Wolter, P. Vir¹, C. Shekhar¹, C. Felser¹, K. Manna¹, V. Süß¹, J. I. Facio, J. van den Brink, G.-H. Park, H. Reichlova², R. Schlitz², M. Lammel, A. Markou¹, P. Swekis¹, P. Ritzinger¹, D. Kriegner², J. Noky¹, J. Gayles¹, Y. Sun¹, K. Nielsch, B. Büchner

Zusammenfassung

Es gibt verschiedene Effekte, die sowohl aus Sicht der Grundlagenforschung als auch für mögliche Anwendungen interessant sind. An dieser Stelle interessiert uns der sogenannte Nernst-Effekt. Der Nernst-Effekt (manchmal auch als Nernst-Ettinghausen-Effekt bezeichnet) beschreibt den Aufbau einer elektrischen Spannung senkrecht zu sowohl einem angelegten Magnetfeld als auch zu einem thermischen Gradienten. Der Nernst Effekt kann verwendet werden, um die Eigenschaften von Quantenmaterialien zu untersuchen. Zusätzlich kann er verwendet werden, um Wärmeenergie in elektrische Energie umzuwandeln

oder Materie zu kühlen, ohne auf mechanische Teile zurückgreifen zu müssen. Damit kann eine Geräuschentwicklung vermieden werden. In diesem Beitrag wird über unsere Arbeit zu den grundlegenden Aspekten des Nernst-Effekts berichtet.

Abstract

There are several effects that are interesting from a fundamental point of view as well as for possible applications. Here, we are interested in the one called Nernst effect. The Nernst effect (sometimes also denoted Nernst-Ettinghausen effect) describes the development of an electrical voltage perpendicular to both an applied magnetic field and a thermal gradient. It can be used to look into the properties of quantum materials. In addition, it could be used to convert thermal energy into electrical energy or to cool matter without the need for mechanical parts, i.e. without generating noise. This contribution will report on our work on the fundamental aspects of the Nernst effect.

Abb. 1: Dünnschichtherstellung am IFW im eigens dafür eingerichteten Labor. Sputteranlage und Atomlagendeponierung sind durch einen Handschuhboxencluster verbunden. So kann eine Verunreinigung der Proben durch Oxidation oder Benetzung durch Luftfeuchtigkeit vermieden werden.

Fig. 1: Thin film preparation in the dedicated laboratory at IFW. Sputter and atomic layer deposition tools are connected via glove boxes to avoid contamination of the samples with air and moisture.



One class of quantum materials are topological materials such as Dirac and Weyl semimetals. One can utilize their response to external magnetic fields to further look into the properties of these material classes. The Nernst effect uses external magnetic fields and thermal gradients and the Hall effect uses external magnetic fields and an applied voltage. Both effects can have a contribution arising from the spontaneous magnetization of ferromagnetic materials. The contribution of the spontaneous magnetization to the Hall and Nernst effects is designated by the term ‘anomalous’, i.e. anomalous Nernst effect (ANE) and anomalous Hall effect (AHE).

The AHE is indicative of the occupied electronic structure, while the Nernst effect gives information about the band structure close to the Fermi energy, which makes it also very sensitive to temperature changes. We will illustrate our work on the Nernst and Hall effects in quantum materials using three different quantum material systems, namely $\text{Co}_3\text{Sn}_2\text{S}_2$, Co_2MnGa and Mn_3Ge .

$\text{Co}_3\text{Sn}_2\text{S}_2$

$\text{Co}_3\text{Sn}_2\text{S}_2$ is a so-called shandite which denotes a rhombohedral crystal structure. In this structure, metallic Co-Sn layers in a triangular pattern are separated by Sn-S blocks [1]. The compound is in its paramagnetic phase at room temperature and orders ferromagnetically at 175 K [2]. We cut micro-ribbons out of a high-quality single crystal using focused ion beam (FIB) cutting [3]. Afterwards, the ribbon is put on a glass slide using a micro manipulator. Then, we write the contact structures defining the Hall bar as well as the on-chip 4-point thermometer and heater lines using conventional lithographic patterning of 10 nm titanium and 150 nm platinum films. The complete device was put on a chip carrier and we utilize wire bonding to electrically connect the Hall bar, heaters and thermometers to the chip carrier. Finally, the transport experiments were performed in a cryostat where we could adjust the temperature and the external magnetic field.

Now, we can investigate the temperature dependency of the Hall and Nernst effect of our $\text{Co}_3\text{Sn}_2\text{S}_2$ micro ribbon. Then, we extracted the anomalous parts, i.e. the AHE and ANE. The differences in the signals of

the ANE and AHE indicate a contribution of the entropy associated with the magnetic degrees of freedom. It can be used to further look into a complete theoretical description of the Nernst effect in the full temperature range. For example, this could be Berry phase and long-range spontaneous symmetry breaking.

Co_2MnGa

Co_2MnGa is a member of the so-called full Heusler compounds. It exhibits very interesting properties, e.g., a high spin polarization and a high Curie temperature of 700 K [4]. In addition, the compound is a magnetic Weyl semimetal showing an unconventional topological surface state [5]. Bulk samples of this compound displayed the fingerprint of the Berry curvature and its connection to evaluated Weyl fermion lines in the signal of the anomalous Hall effect. The very large value of $-6 \mu\text{V}/\text{K}$ for the ANE [6] makes this compound interesting from an application point of view in addition to its interest for fundamental physics experiments.

We investigated Co_2MnGa thin films of 20 nm to 50 nm that were sputter deposited on MgO substrates. The films were covered with 3 nm of aluminum to prevent oxidation of the Heusler compound. Afterwards, the layer stack was post annealed at 500°C. The structure of the films was investigated by x-ray diffraction indicating a high degree of atomic order. We looked into the magnetic properties utilizing squid magnetometry. We found a saturation magnetization of approximately 720 kA/m and typical in-plane and out-of-plane hysteresis loops if compared to bulk samples.

To measure the samples, we defined Hall bar structures comparable to the $\text{Co}_3\text{Sn}_2\text{S}_2$ devices described in the last section. More specifically, we patterned the Hall bars by a combination of conventional, optical lithography and HCl and Ar/ O_2 plasma etching. Afterwards, we again patterned on-chip heaters and thermometers utilizing a lift-off process of 30 nm of platinum.

Finally, we looked into the anomalous Nernst effect and its dependence of the thickness of our $\text{Co}_3\text{Sn}_2\text{S}_2$ devices. We found very large ANE values even in thin films of Co_2MnGa . Combining the electrical and

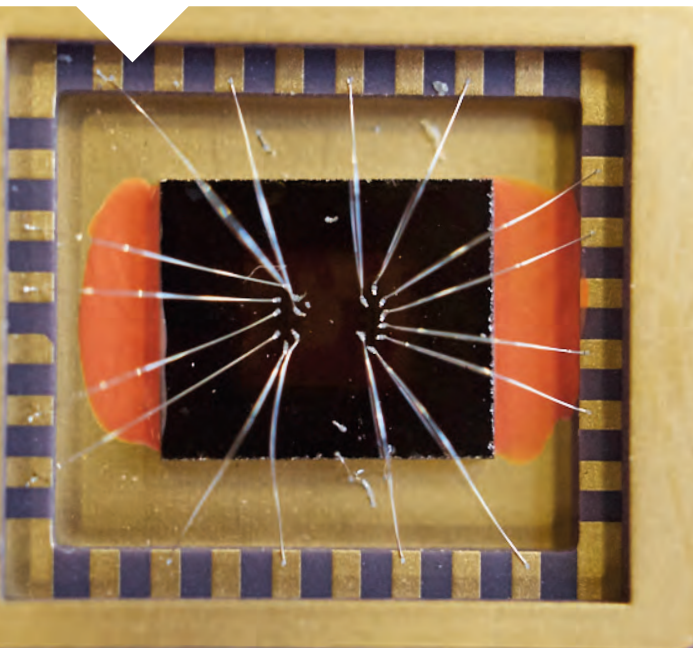
the thermoelectric measurements and the extracted Nernst coefficients, we employed this system to study the Mott relation in thin films with a nontrivial topology inherent to band structure. We observed that the ANE is largest $-3 \mu\text{V}/\text{K}$ for the 40 nm thin film. An analog trend is observed when studying the AHE. By comparing various thicknesses with magnetometry measurements, we observe that this trend is independent in the variation of magnetization. In agreement with recent reports, we believe that both the ANE and the AHC have contributions arising from finite Berry phase curvature. We show that the Mott relation is valid in this material with a nontrivial topology of the band structure.

Mn_3Ge

Mn_3Ge is characterized by a hexagonal crystal structure, where Mn atoms form a kagome lattice of mixed triangles and hexagons with Ge atoms at the center of the hexagons. In the noncollinear antiferromagnetic ground state the Mn magnetic moments are oriented at 120° with respect to their neighbours [7]. Due to the peculiar magnetic structure, multiple Weyl points have been predicted to exist in the band structure of Mn_3Ge [8]. Electrical transport measurement already revealed a striking pure AHE which is constant after a jump at very low fields [9].

Abb. 2: Mit dünnen Aluminiumdrähten kontaktierte Probe auf einem Siliziumsubstrat. So können Proben magnetfeldabhängig und bei tiefen Temperaturen vermessen werden.

Fig. 2: Thin aluminum wires are wire-bonded to a thin film sample on top of a piece of a silicon wafer. Now, the samples can be measured at low temperatures and high magnetic fields.



We studied the Nernst effect in several different configurations and obtained a very pronounced signal when the temperature gradient is applied perpendicular to the planes. The field dependence of the Nernst signal (Fig. 3, left) shows an instant jump at small fields and saturates immediately at a remarkably large value of $-0.5 \mu\text{V}/\text{K}$ at room temperature. The anomalous behavior does not change upon cooling down the system to 5 K, whereas the amplitude exhibits a pronounced temperature dependence. In particular, a peak saturation value of $1.5 \mu\text{V}/\text{K}$ is observed at about 100 K. Furthermore, the Nernst signal exhibits a hysteresis cycle at low fields which remains almost unaltered from 5 K to room temperature. This cycle is rectangular-shaped and closes at around 20 mT (not shown). This hysteretic behavior leads to the fact that Mn_3Ge shows a huge finite Nernst signal even at zero field. Since the Nernst signal is purely anomalous in this compound, we could extract the anomalous Peltier coefficient using Nernst, Hall, Seebeck and resistivity measurements (Fig. 3, right). Assuming that the anomalous transport is caused by a finite Berry curvature due to the existence of Weyl nodes in this system and using a minimal model of a Weyl semimetal, we were able to rationalize the temperature dependence of the anomalous Peltier coefficient. A pertinent fit (red line) provides a direct measure of the Berry curvature at the Fermi level as well as the Weyl point energy and their distance in momentum space, which agree well with band structure calculations [8].

Our findings show clearly that the ANE, beyond the mere statement that the integrated Berry curvature near the Fermi level is finite for a given material, can also be used as a sensitive probe for the experimentally relevant strength of the Berry curvature as well as momentum space geometrical properties of Weyl points lying closest to the Fermi level. The exceptionally large value of the Nernst signal at zero field in Mn_3Ge underpins that noncollinear antiferromagnets may constitute a new material paradigm in the field of spintronic and thermoelectric technologies.

References

[1] W. Schnelle, A. Leithe-Jasper, H. Rosner, F. M. Schappacher, R. Pöttgen, F. Pielhofer, and R. Wehrich, *Phys. Rev. B* 88, 1 (2013)
 [2] M. A. Kassem, Y. Tabata, T. Waki, and H. Nakamura, *Phys. Rev. B* 96, 014429 (2017)
 [3] K. Geishendorf, R. Schlitz, P. Vir, C. Shekhar, C. Felser, K. Nielsch, S.T.B. Goennenwein, and A. Thomas, *Appl. Phys. Lett.* 114, 092403 (2019)
 [4] H. Xi Liu, Y. Honda, T. Taira, K. Ichi Matsuda, M. Arita, T. Uemura and M. Yamamoto, *Appl. Phys. Lett.* 101, 132418 (2012)
 [5] C. Felser and B. Yan, *Nature Mater.* 15, 1149 (2016)
 [6] S. N. Guin, K. Manna, J. Noky, S. J. Watzman, C. Fu, N. Kumar, W. Schnelle, C. Shekhar, Y. Sun, J. Gooth and C. Felser, *NPG Asia Materials* 11, 16 (2019)
 [7] J. F. Qian, A. K. Nayak, G. Kreiner, W. Schnelle, and C. Felser, *J. Phys. D* 47, 305001 (2014)
 [8] H. Yang, Y. Sun, Y. Zhang, W.-J. Shi, S. S. P. Parkin, and B. Yan, *New J. Phys.* 19, 015008 (2017)
 [9] A. K. Nayak, J. E. Fischer, Y. Sun, B. Yan, J. Karel, A. C. Komarek, C. Shekhar, N. Kumar, W. Schnelle, J. Kübler, C. Felser, and S. S. P. Parkin, *Sci. Adv.* 2, e1501870 (2016)

Funding

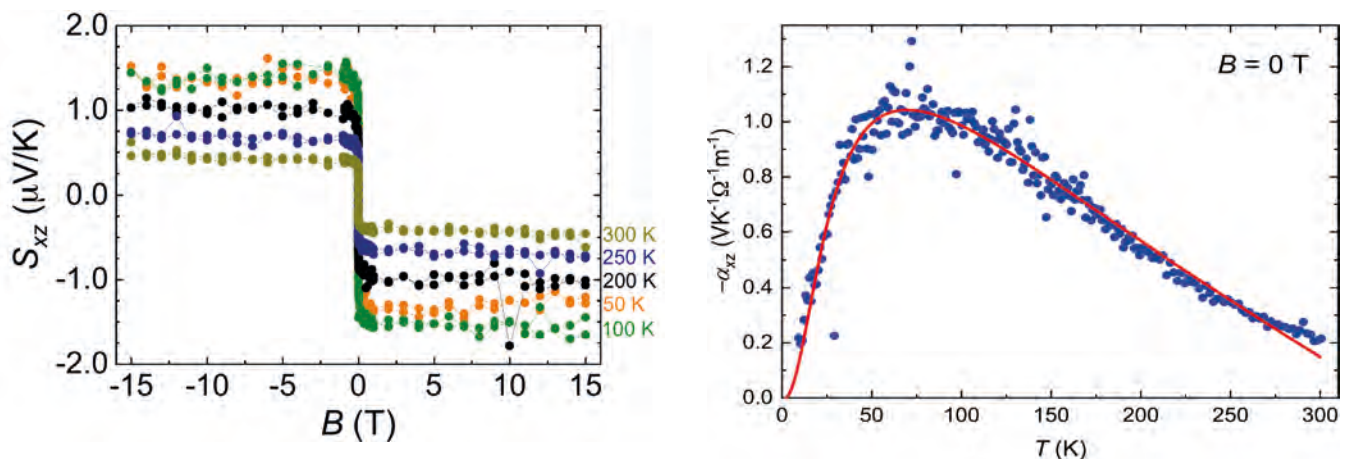
FET Open RIA Grant 766566
 ct.qmat
 CRC 1143
 European Structural and Investment Funds
 Czech Ministry of Education, Youth and Sports

Cooperations

¹⁾ Max Planck Institute for Chemical Physics of Solids, Dresden, Germany.
²⁾ Institut für Festkörper- und Materialphysik and Würzburg-Dresden Cluster of Excellence ct.qmat, Technische Universität Dresden, Germany.

Abb. 3: Peltier-Koeffizient α_{xz} von Mn_3Ge (blaue Punkte). Die rote Linie stellt einen Fit gemäß unseres Modells dar (rechts). Nernst-Signal S_{xz} von Mn_3Ge als Funktion des angelegten Magnetfelds B . S_{xz} erhält man aus der gemessenen Spannung entlang der x-Richtung während ein Temperaturgradient ∇T und ein Magnetfeld B entlang der z- bzw. y-Richtung angelegt werden (links).

Fig. 3: Peltier coefficient α_{xz} of Mn_3Ge (blue dots). The red line represents the fit provided by our theoretical model (right). Nernst signal S_{xz} of Mn_3Ge as a function of the applied magnetic field B . S_{xz} is obtained by measuring the voltage along the x-direction while applying a thermal gradient ∇T and a magnetic field B along z and y-direction, respectively (left).



Dual topology in jacutingaite Pt_2HgSe_3

Jorge I. Facio, Sanjib Kumar Das, Yang Zhang, Klaus Koepf, Jeroen van den Brink, Ion Cosma Fulga

Zusammenfassung

Topologische Phasen elektronischer Systeme koexistieren oft in einem Material, welches damit als starker und schwacher topologischer Isolator zugleich fungiert. Kürzlich wurde eine Reihe von Materialien gefunden, die sowohl schwache topologische Isolatoren als auch Reflektionssymmetrie-geschützte topologische kristalline Phasen sind.

Im vorliegenden Beitrag befassen wir uns mit dem natürlich vorkommenden Mineral Jacutingaite, Pt_2HgSe_3 . Mittels Dichtefunktionalrechnungen zeigen wir, dass dieses Mineral durch eine duale topologische Phase charakterisiert ist. Durch Konstruktion von Tight-Binding-Modellen können wir die wesent-

lichen Eigenschaften dieser dualen Phase definieren und die Hauptmerkmale der Oberflächenspektral-dichte für eine ganze Klasse ähnlicher Materialien beschreiben.

Abstract

Topological phases of electronic systems often coexist in materials, well-known examples being systems which are both strong and weak topological insulators. More recently, a number of materials have been found to have the topological structure of both a weak topological phase and a mirror-protected topological crystalline phase. Here, we focus on the naturally occurring mineral jacutingaite, Pt_2HgSe_3 . Based on density-functional calculations we show that it realizes this dual topological phase. By constructing simplified tight-binding models we capture the essential properties of this dual topological phase and describe the main features of the surface spectral density also for a whole class of related materials.

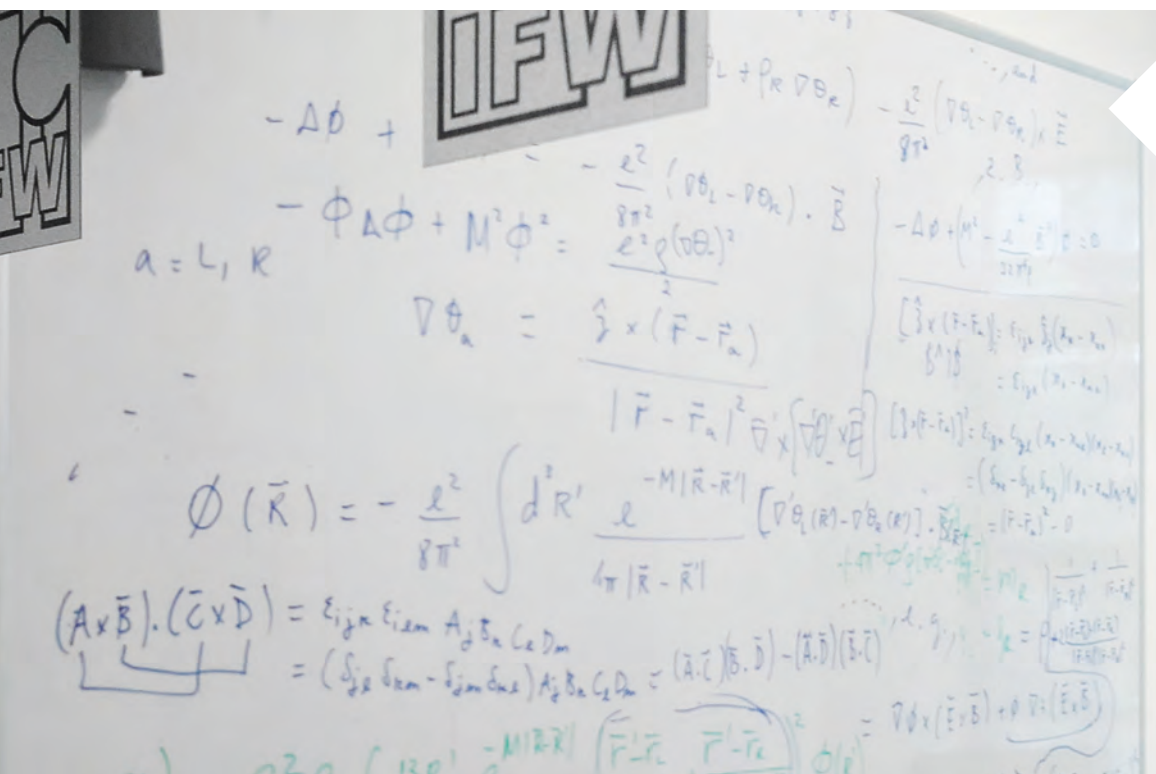


Abb. 1: Eines der wichtigsten Hilfsmittel einer/s theoretischen Physikerin/Physikers ist die Wandtafel, auf der man Gedanken festhält und an der man mit KollegInnen Ideen diskutiert.

Fig.1: One of the most important tools of theoretical physicists is the white board, which serves well for brainstorming and discussions with other colleagues.

Physical systems with topological properties are characterized by two interrelated phenomena: the existence of topological invariants which are an intrinsic property of the system itself (in condensed matter usually the 3-dimensional (3D) infinite bulk or the 2-dimensional infinite multilayer system) and the bulk-boundary correspondence which connects these invariants to the appearance of special protected quantum states after introduction of boundaries/surfaces in such systems. The famous example is the quantum Hall effect, which owes its quantization to topological invariants and exhibits surface states. Since then this concept has been expanded and greatly enriched by the discovery of symmetry protected topological phases such as the time-reversal protected three-dimensional topological insulators (TIs), the related weak topological insulators (WTIs) and crystal symmetry protected phases, called topological crystalline insulators (TCIs). Recently, the bulk boundary correspondence has been further extended by the introduction of higher-order topological insulators (HOTIs).

The identification of materials realizing topological phases is important, since the protected surface states are connected to modified transport properties and under certain conditions to the appearance of strange quantum states (Majorana fermions), and hence interesting for experimental studies and possible applications.

Recently, it was predicted that a two-dimensional monolayer of the naturally occurring mineral jacutingaite (Pt_2HgSe_3) can realize a quantum spin Hall insulating state (QSHI) and it was argued that an inherent instability to inversion symmetry breaking leads to a topological state robust at room temperature and switchable by external electric fields. Even superconductivity of this layered system was suggested. In light of these facts it is of interest to study whether the 3D bulk system itself exhibits topological phases.

We performed a theoretical investigation of 3D jacutingaite [1] based on density functional theory calculations which produce the electronic structure and topological indices of the bulk material. The resulting data can be further mapped onto simplified models, which allow a generalized understanding of the origin of the topological invariants of a whole class of related materials possessing the same crystal symmetries.

The crystal structure of jacutingaite including some essential symmetries and the corresponding Brillouin zone (BZ) including the surface BZs for the (100) and (001) terminations are depicted in Fig. 2. The compound has a layered structure with the Hg atoms sitting in a triangular environment delimited by planes of Se and Pt forming a buckled honeycomb lattice. The band structure close to the Fermi energy can be described as a semimetal with small electron and hole pockets. Similar to Bismuth, the spin-orbit coupling opens a topological gap of around 10 meV throughout the full BZ between the bands forming the electron/hole pockets. Although there is no optical gap this separation between all bands of band number N and smaller and band number $N+1$ and larger allows a mathematically meaningful characterization of the topological nature of the compound.

Besides crystal symmetries the compound possesses time-reversal symmetry (TRS) which gives rise to Z_2 topological indices which can be determined from the parity invariants at time-reversal invariant momenta (TRIM) namely, negative at Γ - and Z - and positive at all X - and R -points (Fig. 2). Hence, we obtain the Z_2 topological indices as $(\nu_0; \nu_1 \nu_2 \nu_3) = (0; 001)$ which classify a weak topological insulator. This is consistent with the idea of engineering WTIs by stacking quantum spin Hall insulator layers along a certain direction, in our case the z - or ΓZ -direction.

The helical edge states of the QSHI phase of each layer together form surface Dirac cones at the projections of the ΓX - and ZR -planes onto the (100) surface BZ. The resulting band crossings along the surface BZ path $\bar{\Gamma} X \bar{R} Z$ can be seen in the surface spectral densities of a (100)-terminated semi infinite slab at points \bar{X} and \bar{R} as shown in Fig. 3a. As long as the translational symmetry in the z -direction is preserved the two Dirac cones cannot hybridize and hence not gap out, since they occur at different k_z -momenta. Note, however that not all 2D materials which are QSHIs will form 3D WTIs after stacking. Consequently, the bulk topological invariants cannot, in general, be inferred from the behavior of the 2D layered material and must be determined separately as done here.

An alternative view on the topological properties is obtained from the concept of elementary band representations (EBRs): if the occupied bands cannot be

decomposed into EBRs they cannot be the result of a set of well localized atom-like orbitals (more exactly Wannier functions) and hence these bands cannot transform into atom-like entities if the lattice is pulled apart to infinite atomic separation. Such a system then cannot be in the same topological class as separate atoms; it must be topologically non-trivial. For systems with inversion symmetry, as is the case for jacutingaite, a simple rule tells us if the occupied bands can be decomposed into EBRs: the number of negative parity eigenvalues per Kramers pair must be a multiple of 4. In our case it is $4N+2$ with N integer and hence non-trivial topology is signaled from the EBR's point of analysis as well.

The stacking of 2D Pt_2HgSe_3 layers in 3D jacutingaite preserves additional symmetries, besides translational symmetry. Here, we focus on the mirror symmetries. Some of the mirror planes are indicated in Fig. 2 (left) by the green planes. In the BZ (right) the 3 mirror planes are spanned by $\Gamma X_i R_i Z$. A particular property of particles with spin $1/2$ is that a rotation by 360 degree does not give back the same wave function but one with a phase factor of -1 . Consequently, applying the mirror symmetry operator twice in a row produces a factor of -1 or for a single operation a phase factor of $\pm i$. Because of that the eigen states

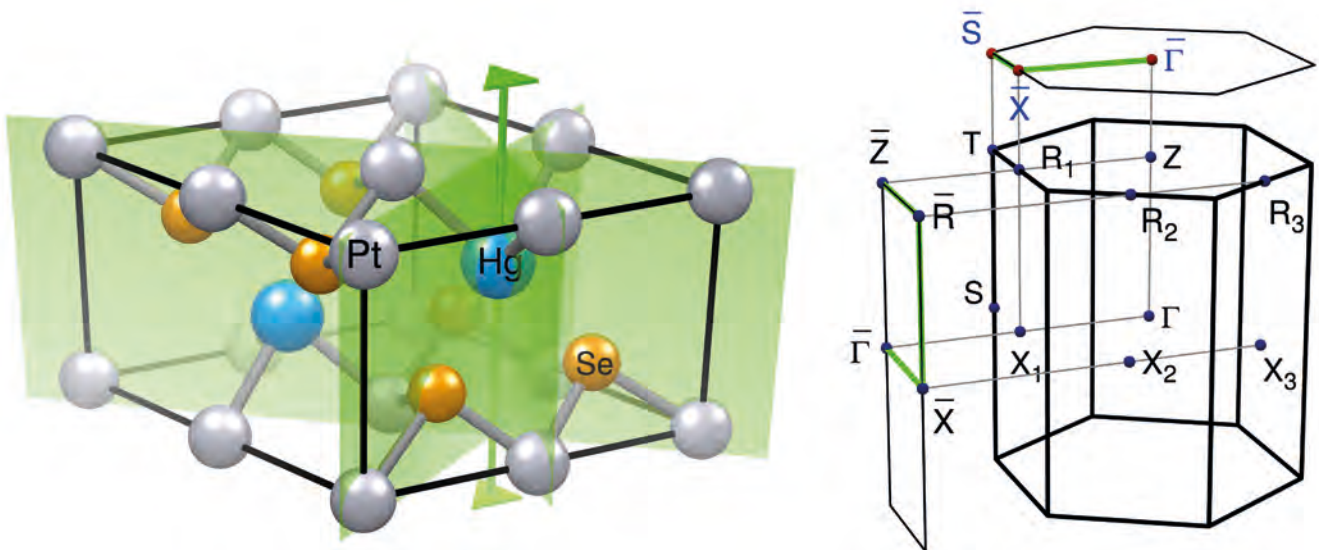
in the mirror planes can be labeled by these mirror eigenvalues and they hence can be divided into two separate subspaces. In each subspace a Chern number C^\pm can be defined and half of the difference of the two defines a topological invariant called the mirror Chern number C_M . For jacutingaite we obtain $C_M=-2$ for each of the mirror planes, which means that this material can realize helical HOTI phases under suitable surface perturbations.

Fig. 3b shows the surface spectral densities for a (001)-terminated semi infinite slab. In this projection the bulk valence and conduction bands overlap and lead to a closing of the gap in the surface spectral function. However, consistent with the mirror Chern number having $|C_M|=2$ a pair of Dirac cones are visible at the \bar{X} -point above and below the Fermi level.

Our findings concerning the positioning of the topological surface states were further corroborated by analysing simplified models of the electronic structure, which were constructed by coupling two strong 3D TIs with appropriate coupling terms, perserving the time-reversal, the three-fold rotational and mirror symmetry. These models, which are applicable in general to systems with these symmetries and lattice structures reproduce the weak invariants, the mirror

Abb. 2: Elementarzelle von Jacutingaite, inklusive einiger relevanter Symmetrieeoperationen: eine dreizählige Drehachse und drei Spiegelebenen durch das Hg-Atom (links). Die dreidimensionale und zwei Oberflächen-Brillouin-Zonen für eine (100)-Terminierung (links) und eine (001)-Terminierung (oben) (rechts).

Fig. 2: Unit cell of jacutingaite showing some of the relevant symmetry operations: a threefold rotation axis and three mirror planes all through the Hg atom (left). The bulk and the surface Brillouine zones for a (100)-termination (left) and a (001)-termination (above) (right).



Chern number and the positions of surface Dirac cones and can be used to further study the degree of influence of various surface perturbations (for which higher order topological phases, HOTIs, could occur), the behavior of modes localized to step edges as well as the effects of disorder. Moreover, they may be used to determine the degree of influence of surface modes on transport properties in the presence of co-existing bulk states.

Together with the nontrivial weak topological invariant the nonzero mirror Chern number leads us to predict that jacutingaite, which is a naturally occurring mineral, is in a dual topological phase. This result places jacutingaite into the list of materials which can host surface states protected by different, unrelated symmetries.

Although, the material is a semimetal with small electron and hole pockets, which precludes domination of transport by surface states it has a well defined topological gap which together with the topological invariants leads to surface states in the energy range of the topological gap, which could be detected by experimental techniques as angle-resolved photoemission spectroscopy or scanning tunneling spectroscopy.

References

- [1] Facio et al., Phys. Rev. Mater. 3 (2019) 074202
- [2] C. Felser, J. Phys. D 47, 305001 (2014)

Funding

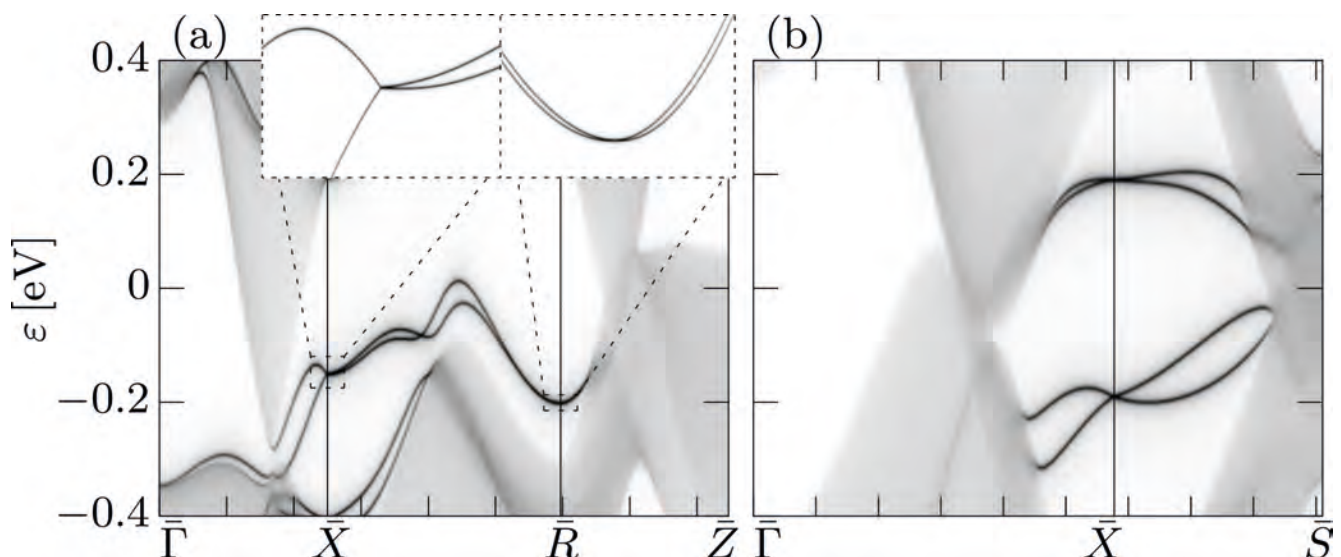
DFG via SFB 1143, project A5
 Würzburg-Dresden Cluster of Excellence ct.qmat

Cooperations

Max Planck Institute for Physics of Complex Systems,
 Dresden, Germany.
 Würzburg-Dresden Cluster of Excellence ct.qmat.

Abb. 3: Oberflächenspektralichten von halbinendlichen Slabs mit a: (100)-Terminierung and b: (001)-Terminierung. Die Vergrößerungen heben die Dirac-Kone hervor während die dunklen Partien generell Oberflächenzustände zeigen.

Fig. 3: surface spectral densities of a semi-infinite slab with a: (100)-termination and b: (001)-termination. The insets highlight the surface Dirac cones, while in general the dark features are surface states.



Layered α -TiCl₃: Microsheets on Substrates for Ethylene Polymerization with Enhanced Activity

Martin Grönke, Ubed S. F. Arrozi², Nadine Bronkalla, Peer Schmidt¹, Martin Valldor, Steffen Oswald, Thomas G. Woodcock, Victoria Eckert, Qi Hao, Laura Plüschke^{3,4}, Alben Lederer^{3,4}, Kornelius Nielsch, Bernd Büchner, Stefan Kaskel², and Silke Hampel

Zusammenfassung

α -Titan(III)-Chlorid (α -TiCl₃) ist ein 2D Material und fest etablierter Ziegler-Natta Katalysator für die Polymerisierung von Ethylen. Wir präsentieren eine Technik zur Präparation von dünnen (4 μ m), hochkristallinen TiCl₃ Schichten mit außergewöhnlichen physikalischen Eigenschaften wie beispielsweise eine erhöhte chemische Reaktivität durch ein vergrößertes Oberfläche-zu-Volumen Verhältnis. α -TiCl₃ Mikroschichten mit deutlich erhöhtem katalytischen Effekt werden durch chemischen Gasphasentransport (CVT) direkt auf Yttrium-stabilisiertes Zirkonoxid (YSZ) Substraten abgeschieden. Diese dünnen

Schichten wurden für die Polymerisierungsreaktionen genutzt. Durch diese Mikrostrukturierung wurde eine signifikante Erhöhung der katalytischen Aktivität von 16 Prozent, bzw. durch delaminierte Nanoschichten von 24 Prozent, im Vergleich zum makroskopischen Festkörpermaterial nachgewiesen.

Abstract

α -titanium(III) chloride (α -TiCl₃) is a layered 2D compound and a well-established Ziegler-Natta catalyst for the polymerization of ethylene. A new synthesis technique is used to obtain thin (4 μ m) high-crystalline microsheets of α -TiCl₃ with exceptional physical properties due to an enlarged surface-to-volume ratio. Chemical vapor transport (CVT) of α -TiCl₃ directly on substrates results in microsheets with a considerable improved catalytic effect. These thin sheets of α -TiCl₃ on Yttrium stabilized zirconia (YSZ) substrates were implemented as catalysts for ethylene polymerization reactions. A significant improvement of catalytic activity of either 16 percent related to microsheets or 24 percent with respect to subsequent delaminated nanosheets was achieved due to downscaling effects.

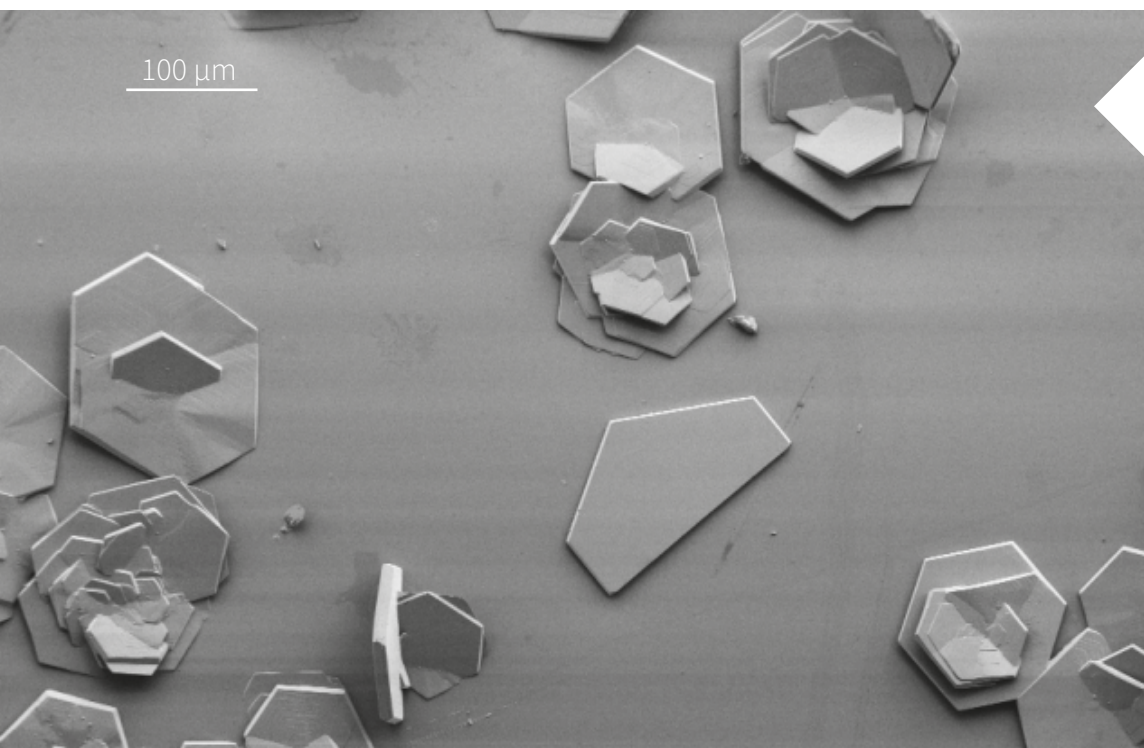


Abb. 1: Rasterelektronenmikroskopieaufnahme von α -TiCl₃ Mikroschichten auf YSZ Substraten im Sekundärelektronenmodus unter Verwendung einer Transferkammer von Kammrath & Weiss um jegliche Sauerstoffkontamination während des Transferprozesses (Glovebox zum SEM) auszuschließen.

Fig. 1: Scanning electron microscopy (SEM) image in the secondary electron mode of α -TiCl₃ microstructures on YSZ substrates using a transfer module by Kammrath & Weiss to avoid any oxygen contamination while transferring the samples from the glovebox to the SEM.

Introduction

Van der Waals bonded transition metal trihalides (TMTHs) with formula MX_3 (M = transition metal, X = Cl, Br or I), deployed since decades as catalysts in organic synthesis procedures, feature incomplete filled d orbitals that are strongly correlated due to the Coulomb repulsions of electrons. These TMTHs were recently re-examined with respect to their layered nature and their consequent potential as ultrathin magnetic layers or improved catalysts with enlarged surface-to-volume ratio. α -titanium(III) chloride (α -TiCl₃) is a two-dimensional (2D) compound and very known for its catalytic properties (Ziegler-Natta catalyst) related to polymerization reactions of olefins. As the weakly coupled sheets of TiCl₃ are comprised of honeycombs, similar to graphene, our interest pointed towards an investigation of new functionalities while downscaling from bulk to thinner micro- and nano dimensions. The initial idea was to enlarge the surface-to-volume ratio of sheets by miniaturization and thus to probable enlarge the catalytic properties by exposure of more active surface sites. In order to extensively avoid structural defects e.g. stacking faults, often associated with mechanical exfoliation, chemical vapor transport (CVT) of nano- and microsheets directly on YSZ (yttria stabilized zirconia, ZrO₂:Y) substrates benefits from low timescales (minutes), less material consumption (very few mg) and highly crystalline solids. For a rational synthesis planning, the preparation of well-suited TiCl₃ microsheets was simulated priorly to avoid time consuming trial-and-error synthesis approaches. The synthesized TiCl₃ crystals on top of the YSZ substrate were characterized by several analytics proving morphology, crystallinity, phase-purity and the desired composition. In addition, as-grown TiCl₃ microsheets were delaminated to reveal even thinner nanosheets. Finally, as-prepared TiCl₃ samples with different thicknesses (bulk, micro- and nanosheets) were investigated as catalytic model systems for the polymerization of ethylene.

Thermodynamic Modeling

Optimum growth conditions of TiCl₃ microsheets were deduced by application of thermodynamic simulations using the freeware TRAGMIN. By modelling it is possible to calculate the temperature dependent composition of the occurring gas phase with

specific partial pressures of all potential components as well as their contribution to the transport process under experimental conditions (e.g. ampoule material and volume). Although TiCl₃ sublimates at higher temperatures (> 900 K) without the addition of a transport agent, modeling showed that medium temperatures (600-700 K) and thus low transport rates (≈ 1 mg/h) are beneficial for the deposition of thin catalytic TiCl₃ sheets directly on YSZ surfaces. The decrease of transport temperatures (600-700 K) requires the implementation of a transport addition. We calculated the potential suitability of pure Cl₂, Al₂Cl₆ and Ga₂Cl₆ as transport agents for the vapor growth of TiCl₃ microsheets. The calculations revealed that the implementation of minimum amounts of dimeric Ga₂Cl₆ (where actually GaCl₃ is introduced) is advantageous for crystallization of thin sheets composed of TiCl₃. The resulting gas phase consists of various components with distinct partial pressure (Fig. 2). The introduction of GaCl₃ as soft chlorinating agent results in the formation of the more volatile transport efficient titanium species TiCl₄ and also GaCl (transport relevant heterogeneous equilibrium: $2 \text{TiCl}_3 + 0.5 \text{Ga}_2\text{Cl}_6 \rightleftharpoons 2 \text{TiCl}_4 + \text{GaCl}$) with rather high partial pressures (TiCl₄ and GaCl). Thereby both gaseous molecules of Ga₂Cl₆ and GaCl₃ function as transport agents, but Ga₂Cl₆ is more effective. The simulation results showed that vapor transport of catalytic TiCl₃ microsheets is favorable by using fractional additional amounts of GaCl₃ (few mg) and medium reaction temperatures (700 \rightarrow 600 K). These reaction conditions were applied for the successful deposition of TiCl₃ microstructures directly on YSZ substrates, used as a catalyst for polymerization reactions.

Vapor growth, delamination and characterization of α -TiCl₃ micro- and nanosheets

Based on the prior thermodynamic modeling results, α -titanium(III) chloride (α -TiCl₃) microsheets were prepared directly on YSZ substrates by short time CVT in sealed silica glass (quartz) ampoules for around 1 hour from 700 to 600 K in two-zone furnaces. The mass of deposited α -TiCl₃ at YSZ substrates could be determined to be 0.5 mg (± 0.2 mg). The morphology and dimensions of microsheets were investigated by microscopy. For scanning electron microscopy (SEM) we used a transfer chamber by Kammrath & Weiss to exclude any oxygen, since α -TiCl₃ and espe-

cially its microsheets are extremely oxygen sensitive (Fig. 1). The as-prepared microsheets appear as dark and shiny-purple hexagons or half-hexagons and exhibit thicknesses of about 4 μm and lateral dimensions of about 75 μm (Fig. 3). Using delamination techniques subsequently to CVT led to thinner nanostructures that are slightly visible with weaker purple color and thicknesses less than 200 nm with lateral dimensions of about 25 μm . Using SEM we observed stacked and individual deposited $\alpha\text{-TiCl}_3$ sheets on top of YSZ (Fig. 1). By means of EDX the desired composition of microsheets (Ti:Cl = 1:3, according to TiCl_3) could be confirmed without any oxygen contaminations. Thin catalytic TiCl_3 nanosheets were also investigated by TEM. Similarly to SEM-EDX, TEM-EDX could prove TiCl_3 . Additional TEM nano-diffraction investigations confirmed the high crystallinity of deposited layers by occurrence of many reflections spots that fit to TiCl_3 with trigonal space group $P\bar{3}m1$. The high crystallinity of TiCl_3 samples was also approved by means

of X-ray diffraction investigations using thicker TiCl_3 flakes, deposited under the exact same conditions, but longer transport times (24 h). Surface sensitive X-ray photoelectron spectroscopy (XPS) showed that the surface of both bulk and TiCl_3 microsheets are highly probable oxidized by the presence of only fractional amounts of oxygen or moisture. In summary, we could successfully synthesize $\alpha\text{-TiCl}_3$ microsheets on YSZ substrates, and these sheets are utilized to be implemented as catalysts for enhanced production of polyethylene.

Ethylene polymerization using as-grown $\alpha\text{-TiCl}_3$ microsheets

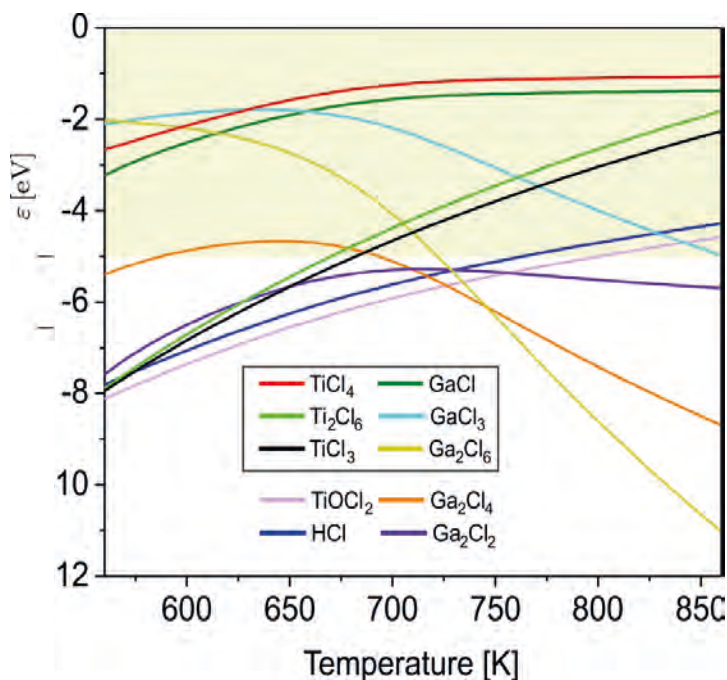
Gas phase reactions of ethylene polymerization were performed in cooperation with TU Dresden using as-prepared catalytic $\alpha\text{-TiCl}_3$ microsheets on top of YSZ substrates. The starting material of $\alpha\text{-TiCl}_3$ (bulk $\alpha\text{-TiCl}_3$) was used as a comparison. By employing AlEt_3 as the co-catalyst and a static pressure of ethylene at 10 bar, the ethylene polymerization reaction at room temperature catalyzed by $\alpha\text{-TiCl}_3$ microsheets (4 μm thickness) succeeded and had a clear 16 % increase in the activity compared to bulk $\alpha\text{-TiCl}_3$ (5.8 and 5 g g^{-1} , respectively) after a reaction time of 1 h. Using similar catalytic reactions conditions but in contrast even thinner $\alpha\text{-TiCl}_3$ nanosheets (200 nm thickness) the catalytic activity increased once again up to 24 % (6.2 g g^{-1}) in comparison to the bulk material (Fig. 3). This is the first time that an improved catalytic effect of $\alpha\text{-TiCl}_3$ is observed as a result of downscaling from bulk to micro- and nanosheets by CVT. Furthermore this is a proof-of-concept that an enlargement of surface-to-volume ratio leads to increased catalytic properties. The produced polyethylene was in addition further characterized by microscopy, spectroscopy, X-ray diffraction, differential scanning calorimetry and size-exclusion chromatography.

Conclusion

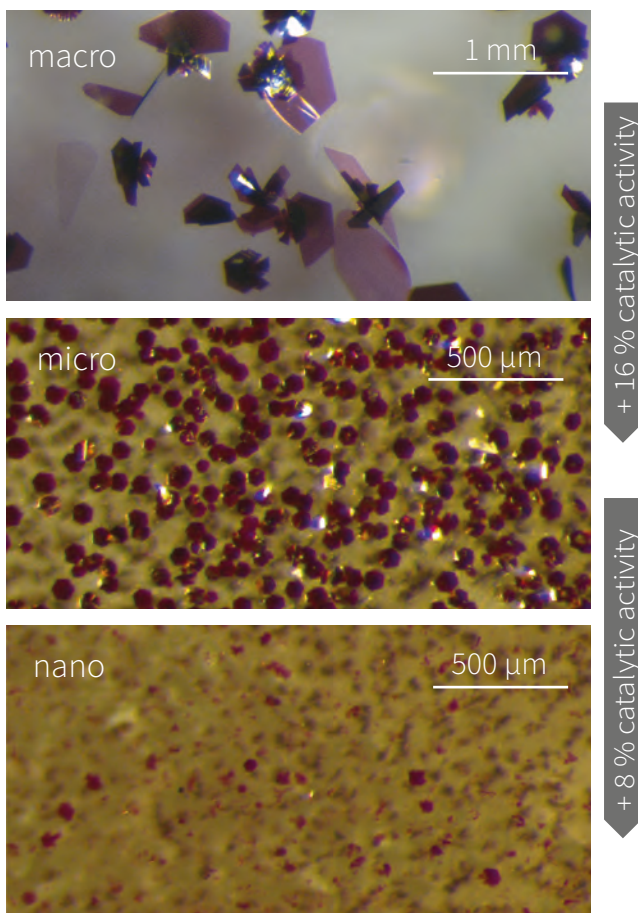
We synthesized highly crystalline and phase pure $\alpha\text{-TiCl}_3$ microsheets with thicknesses around 4 μm on YSZ substrates by chemical vapor transport. The chemical composition and phase purity of the as-prepared sheets was confirmed by spectroscopy and diffractions techniques. Rational synthesis planning

Abb. 2: Thermodynamische Modellierung unter Nutzung der Software TRAGMIN: Partialdrücke der Komponenten in der Gasphase in Bezug auf das eingesetzte System $\text{TiCl}_3/\text{GaCl}_3$ ($n\text{TiCl}_3/\text{GaCl}_3 \approx 5:1$), der gelbe Bereich im Graph kennzeichnet den transportrelevanten Bereich für Komponenten mit einem Partialdruck höher als 10^{-5} bar in logarithmischer Auftragung (TiCl_4 , GaCl , GaCl_3 , Ga_2Cl_6 , Ti_2Cl_6 , TiCl_3 und Ga_2Cl_4 in absteigender Relevanz in Bezug auf die genutzten Transporttemperaturen 700 \rightarrow 600 K).

Fig. 2: Thermodynamic simulation using the program package TRAGMIN: partial pressures of the component species in the gas phase according to the applied system $\text{TiCl}_3/\text{GaCl}_3$ ($n\text{TiCl}_3/\text{GaCl}_3 \approx 5:1$), the yellow area indicates the transport relevant range for components with a partial pressure higher than 10^{-5} bar (TiCl_4 , GaCl , GaCl_3 , Ga_2Cl_6 , Ti_2Cl_6 , TiCl_3 and Ga_2Cl_4 in decreasing relevance according to applied deposition temperatures 700 \rightarrow 600 K) with respect to the logarithmic application of values.



of α -TiCl₃ crystals succeeded by modeling the gas phase equilibria and transport simulations. From these calculations, we concluded that Ga₂Cl₆ acts as the main transport agent, while TiCl₄ and GaCl are the main transport relevant gas species at applied temperatures. According to the simulations, the temperature range 700 → 600 K proved to be very suitable to deposit microsheets in short time vapor transport. As a highlight of our studies, we performed ethylene polymerization reactions with α -TiCl₃ microsheets grown by CVT. A clear enhanced activity of α -TiCl₃ microsheets up to 16 %, compared to bulk α -TiCl₃ crystals, has been observed as a consequence of an increased surface-to-volume ratio. The improvement of catalytic activity by downsizing effects was also reconfirmed by using even thinner α -TiCl₃ nanosheets (200 nm). Thus, a significant increase of up to 24 % was achieved by enlargement of active α -TiCl₃ catalyst sites. With this study, we have further developed and subtilized the concept of downsizing α -TiCl₃ crystals to improve the catalytic properties due to a decrease of bulk and increase of surface effects. For future investigations, it could be possible to exhibit the 2D structure of α -TiCl₃ to generate ultrathin layers down to the monolayer limit.



References

- M. Grönke et al., Chem. Mater. 31, 5305–5313 (2019).
 E. Benckiser, Phys. J. 18, 146 (2019).
 P. Miro et al., Chem. Soc. Rev. 43, 6537–6554 (2014).
 TRAGMIN: www.tragmin.de

Cooperations

- ¹⁾ Institute for Applied Chemistry, Brandenburg University of Technology Cottbus-Senftenberg, Germany.
- ²⁾ Department of Inorganic Chemistry, Technische Universität Dresden, Germany.
- ³⁾ School of Science, Faculty of Chemistry and Food Chemistry, Technische Universität Dresden, Germany.
- ⁴⁾ Leibniz-Institut für Polymerforschung Dresden e.V., Germany.

Abb. 3: Konzept zur Herstellung von α -TiCl₃ Mikroschichten: durch CVT wurden dünne Schichten (4 μ m Schichtdicke) auf YSZ Substraten abgeschieden welche die katalytische Aktivität von TiCl₃ um 16 % erhöhen (im Vergleich zum TiCl₃ Bulkmaterial); die aufgewachsenen Schichten wurden daraufhin delaminiert um α -TiCl₃ Nanoschichten (200 nm Schichtdicke) zu erhalten welche die Aktivität nochmals steigern (24 % im Vergleich zum Bulkmaterial).

Fig. 3: Concept of preparation of α -TiCl₃ microsheets: thin sheets (4 μ m thickness) were initially deposited on YSZ substrates by CVT that enhanced the catalytic activity up to 16 % (in comparison to the bulk material); the as-grown microsheets were subsequently delaminated to obtain α -TiCl₃ nanosheets (200 nm thickness) with even higher activity (24 % in comparison to bulk α -TiCl₃).

First intrinsic magnetic topological insulator

Anna Isaeva, Alexander Zeugner¹, Anja U. B. Wolter, Sebastian Gaß, Laura T. Corredor-Bohorquez, Alexey Alfonsov, Kavita Mehlawat, Vladislav Kataev, Federico Caglieris, Christian Hess, Romain Giraud, Jorge I. Facio, Rajyavardhan Ray, Manuel Richter, Hendrik Bentmann², Raphael C. Vidal², Bernd Büchner

Zusammenfassung

Als Teil eines interdisziplinären Forscherteams haben wir ein Quantenmaterial neuer Art, MnBi_2Te_4 , entdeckt, dessen Kristallzüchtungsmethode optimiert sowie strukturelle, magnetische und elektronische Eigenschaften bestimmt [1-3].

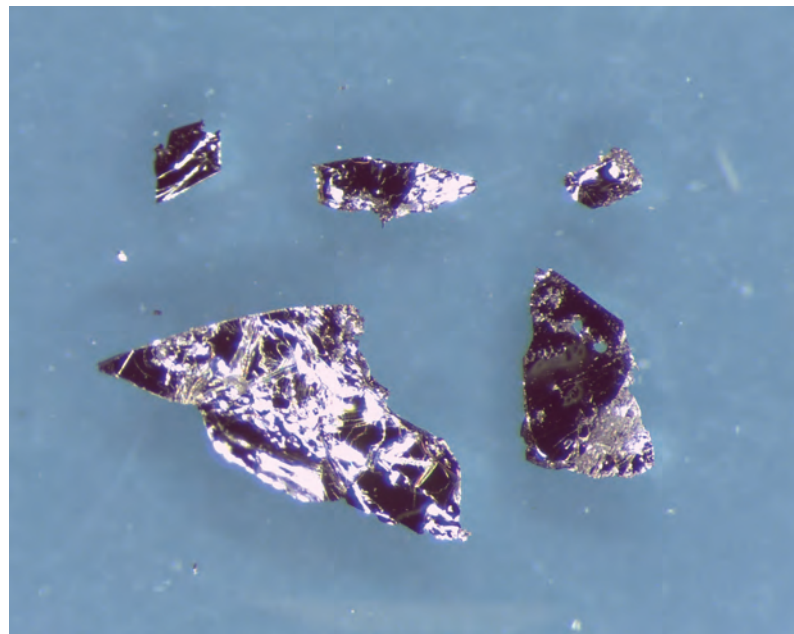
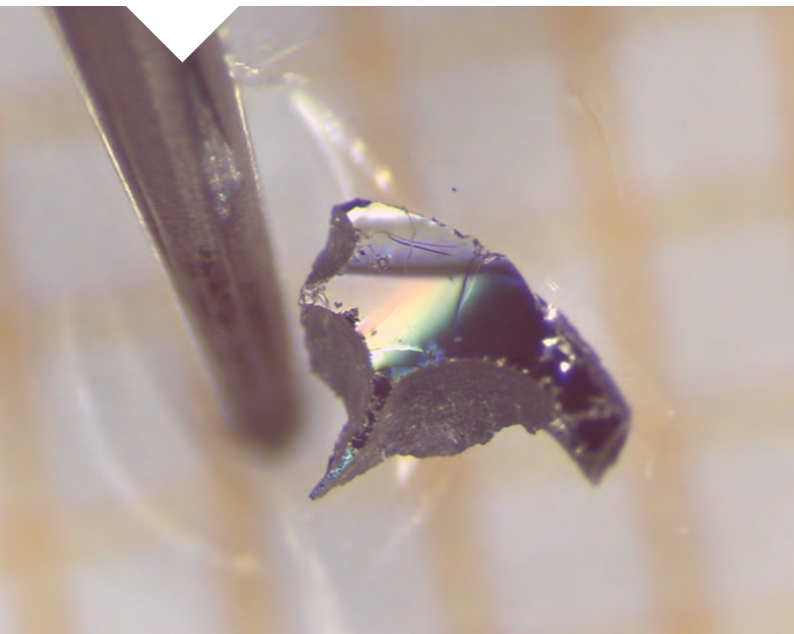
MnBi_2Te_4 ist der erste antiferromagnetische topologische Isolator (TI): er ist intrinsisch magnetisch geordnet und topologisch nicht-trivial. Intrinsisch bedeutet dabei, dass die magnetische Anordnung aus dem Inneren des Materials resultiert, nämlich durch ein periodisches Untergitter aus Mn-Atomen. Diese Besonderheit ist ein entscheidendes Merkmal gegenüber dem nicht-magnetischen, strukturell verwandten „Patriarchen“ aller TIs, Bi_2Te_3 . Eine spekt-

roskopische Studie enthüllt die besonderen Oberflächenzustände an der Oberfläche von MnBi_2Te_4 , welche eine Energielücke besitzen. Das macht das Material vielversprechend für antiferromagnetische Spintronik, Quantentechnologien und magnetische Erscheinungen in zwei Dimensionen.

Abstract

As part of an interdisciplinary consortium we discovered a new type of bulk quantum material, MnBi_2Te_4 , developed its crystal-growth technique, determined its crystal structure, magnetic and electronic properties [1-3]. MnBi_2Te_4 is the first antiferromagnetic topological insulator (TI): it exhibits intrinsic magnetic and topological properties. As the word “intrinsic” suggests, magnetic order originates from within the material itself, namely from a periodic sublattice of Mn atoms. This is a notable step forward with respect to the non-magnetic, structurally-related “patriarch” of all TIs, Bi_2Te_3 . Spectroscopy confirms that the surface of MnBi_2Te_4 hosts spin currents that are promising for applications in antiferromagnetic spintronics, quantum technologies and the exploration of two-dimensional magnetic phenomena.

Abb. 1: Durch unsere optimierte Methode gezüchtete Einkristalle von MnBi_2Te_4 .
Fig. 1: Single crystals of MnBi_2Te_4 grown by our optimized technique.



Advent of topological magnetic materials

Materials engineering aspects are often the driving force behind exploration of new compounds. Lately the spotlight is shifting towards new functionalities based on quantum phenomena. All too often special conditions, like very low temperatures, extreme magnetic fields or high pressure, are needed for these properties to manifest. The vision is to fabricate tailored materials that take advantage of quantum mechanical effects under “real world” conditions, namely, close to room temperature, without external fields and at macroscopic length scales. These properties could promote technological advances such as further miniaturization of electronic devices, novel types of spin transistors and even quantum computing. An umbrella term – quantum material – is widely spreading over the solid-state physics and materials science and brings together various types of materials with (strong) electron correlations or/and a certain topology of the collective electron wave function. Over the past decade, various classes of quantum functional materials have emerged, but the most famous are undoubtedly topological insulators that hold promises for robust, quantized surface spin transport at ambient conditions.

Following the experimental discovery of the 3D topological insulator (TI) in Bi_2Te_3 and Bi_2Se_3 in 2009 [4], a conceptually new direction of research on quantum transport has emerged. In a very general sense, it is focused on how the topology of the electron wave function manifests itself in the material’s properties. Over the past decade, a plethora of topological states of matter has been revealed, which encouraged exciting proposals for next-generation electronic devices enabling low energy consumption, dissipationless topological transport and even topological quantum computation. Nowadays particular efforts are focused on interacting topological phases that combine quantum spin transport in the presence of magnetic order or superconductivity and a non-trivial topology of the electronic spectrum. Magnetic topological insulators (MTI) are one particular example. An MTI material features one edge state (spin current) on its surface that can realize quantized Hall conductivity even in zero external magnetic field, the so called Quantum Anomalous Hall Effect (QAHE). MTIs are envisioned as a hotbed for novel quasiparticles and exotic quantum phenomena, while their

experimental realization is very challenging.

The *first extrinsic MTI* – a Cr-doped $(\text{Bi,Sb})_2\text{Te}_3$ thin film – was fabricated in 2013 [5]. The QAHE was observed for the first time, but only in the mK range. Plus high external magnetic fields above 10 T were required to suppress the dissipative conduction channels. Further optimisations, involving complex material engineering of modulated doped heterostructures, helped to stabilize the QAHE up to several Kelvin only. Inhomogeneity of magnetic dopants distribution, variations in the exchange gap size, and poor reproducibility are general serious obstacles for the advance of extrinsically doped MTIs.

The first intrinsic magnetic topological insulator

Single-crystals of the *first intrinsic MTI*, MnBi_2Te_4 , were obtained and characterized in a joint endeavour of many research teams [1,2]. Our joint group from the Leibniz IFW Dresden and Technische Universität Dresden highly values a careful optimization of crystal-growth techniques and an accurate determination of chemical purity and crystal structure. To obtain high-quality single crystals (Fig. 1), we have meticulously optimized the synthesis protocol, taking into account the peculiar thermal behaviour of MnBi_2Te_4 : single-crystals can be synthesized by slow cooling within a narrow, well-controlled high-temperature interval at around 600°C (Fig. 2).

From X-ray single-crystal diffraction experiments, we found that MnBi_2Te_4 is a layered compound composed of septuple layers that structurally resembles the “patriarch” of all TIs, Bi_2Te_3 , but on top of that it features a unique periodic sublattice of Mn atoms. We also established a ubiquitous off-stoichiometry of this material, $\text{Mn}_{1-x}\text{Bi}_{2+2x/3}\text{Te}_4$ ($x = 0.15$), reflecting that a certain portion of Mn atoms enter the Bi sites and vice versa.

Further comprehensive field- and temperature-dependent magnetization measurements by a partner group at the Leibniz IFW Dresden showed that the well-ordered Mn magnetic centers establish a 3D long-range antiferromagnetic state below 24 K. It originates from an antiferromagnetic coupling between the septuple layers, which each exhibits a ferromagnetic intralayer coupling. Competing anti- and ferromagnetic couplings are indicated by the small and positive value of the Curie-Weiss temperature. The out-of-plane Mn(II) magnetic state is also confirmed

by X-ray photoemission, X-ray absorption and linear dichroism data. Our theory partners from the Donostia International Physics Centre (DIPC), The Basque Country, Spain, concluded that a combination of this magnetic ground state and a centrosymmetric space group ($R-3m$) entail the $Z_2 = 1$ topological classification and classify MnBi_2Te_4 as the first antiferromagnetic topological insulator (AFM TI) [1].

Advanced angle-resolved photoemission (ARPES) experiments on our single crystals performed by colleagues from the University of Würzburg, Germany, provided evidence for a surface state on the (0001) cleaving plane, which is essentially a gapped Dirac cone [1,3]. This accords with theoretical predictions for an MTI. What was completely unexpected is that this gap persisted well above the critical temperature! In its paramagnetic state MnBi_2Te_4 was predicted to transform into a typical 3D TI, like Bi_2Te_3 , and to exhibit a gapless surface electronic spectrum. Spin-resolved ARPES data and the Mn spin dynamics extracted from electron spin resonance (ESR) experiments performed by a partner group at the Leibniz IFW Dresden on MnBi_2Te_4 in the paramagnetic state evidenced anisotropic spin fluctuations and instantaneous out-of-plane polarization of Mn spins that might be responsible for the persisting gapped surface state on the (0001) plane in the absence of long-range magnetic order. Furthermore, photoemission measurements below and above the magnetic ordering tem-

perature conducted by colleagues from Saint-Petersburg State University, Russia, demonstrated changes in the gapped state as a function of temperature. This means that the topological surface state of MnBi_2Te_4 is significantly affected by the antiferromagnetic state in the bulk mostly due to the S-broken state on it.

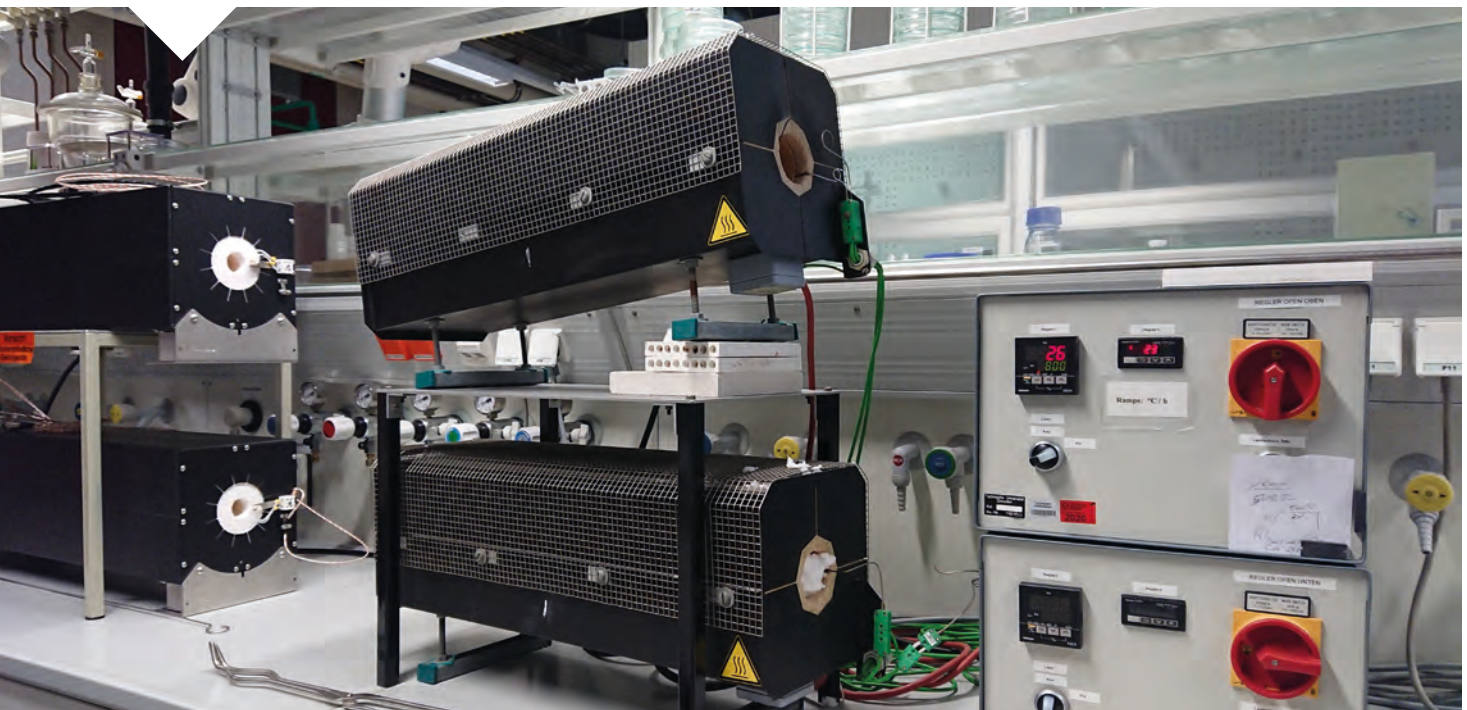
All pieces of this puzzle are put together in the recent article [1] to confirm the unique topological flavour of the layered antiferromagnetic compound MnBi_2Te_4 (Fig. 3).

Outlook: the structure family is expanding

Potential implications of this discovery are manifold. The newly developed bulk material MnBi_2Te_4 heralds a new, post-doping era in the field of MTI. The observation of a stable QAHE may pave avenues towards a new electrical resistance standard and a new type of quantum metrology, as well as the realization of Majorana fermions via proximity to a superconductor. Beyond that, an experimental realization of an AFM TI contributes to the booming field of antiferromagnetic spintronics, which may make use of the unique magnetoelectric response of an AFM TI in constructing axion modulators and sensors. An emergent field of magnetic van der Waals materials, that aims at new transistor designs with van der Waals heterojunctions, may profit considerably from a new two-dimensional ferromagnet, that MnBi_2Te_4 realizes in the thin-film limit. Many of these fascinating prospects

Abb. 2: Hochtemperatur-Heizöfen mit präziser Temperaturregulation am Institut für Anorganische Chemie II, TU Dresden.

Fig. 2: High-temperature furnaces with precise temperature control at the Institute of Inorganic Chemistry II, TU Dresden.



are already being tested, and other groups worldwide are joining the effort to explore the interplay of magnetism and topology in MnBi_2Te_4 . The first observation of the QAHE up to 6.5 K in thin-layer specimens of MnBi_2Te_4 was reported very recently [6].

Our most recent synthetic experiments reveal more structure derivatives of MnBi_2Te_4 that are relevant in the context of MTIs [7,8]. We currently witness the emergence of a new family of magnetic topological insulators that rely on an intrinsic magnetization rather than on the magnetic doping approach. Layered van der Waals compounds $(\text{MnBi}_2\text{Te}_4)(\text{Bi}_2\text{Te}_3)_n$, $n = 1, 2$ with a periodic Mn sublattice are built by varying sequences of septuple (MnBi_2Te_4) and quintuple (Bi_2Te_3) layers. We envision that the $(\text{MnBi}_2\text{Te}_4)(\text{Bi}_2\text{Te}_3)_n$ family will gain more importance in the coming years as a unique material platform for the realization of tunable MTI quantum phenomena thanks to their versatile magnetic and electronic properties.

References

- [1] M. M. Otrokov et al., *Nature* 576 (2019), 416.
- [2] A. Zeugner et al., *Chem. Mater.* 31 (2019), 2795.
- [3] R. C. Vidal et al., *Phys. Rev. B.* 100 (2019), 121104.
- [4] H. Zhang et al., *Nature Phys.* 5 (2009), 438; Y.L. Chen et al., *Science* 325 (2009), 178.
- [5] C.-Z. Chang et al., *Science* 340 (2013), 161.
- [6] Y. Deng et al., *Science* (2020), 10.1126/science.aax8156.
- [7] D. Souchay et al., *J. Mater. Chem. C* 7 (2019), 9939.
- [8] R. C. Vidal et al., *Phys. Rev. X* 9 (2019), 041065.

Funding

DFG SPP 1666 IS 250/1-2.
ERA-Chemistry RU 766/15-1.
DFG SFB 1170.
DFG SFB 1143.
EXC 2147, ct.qmat.
IFW Excellence Programme.

Cooperations

- ¹⁾ TU Dresden, Germany.
- ²⁾ Universität Würzburg, Germany.
- ³⁾ DIPIC, Spain.
- ⁴⁾ University Saint-Petersburg, Russia.

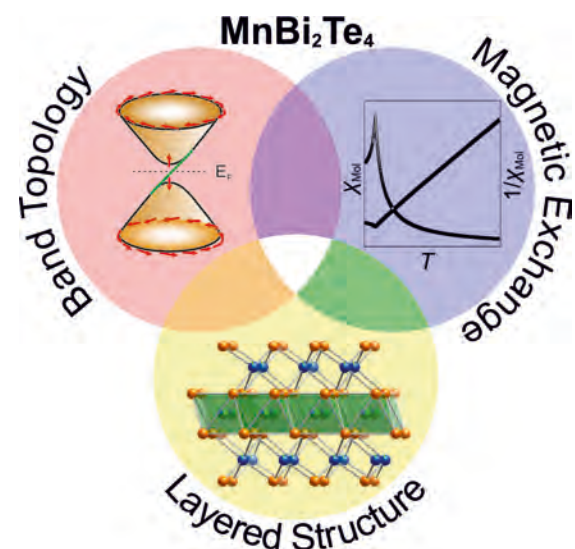


Abb. 3: Das Zusammenspiel zwischen dem schichtartigen Aufbau, der ferromagnetischen Anordnung und der nicht-trivialen Topologie der elektronischen Struktur erzeugt die einzigartigen physikalischen Eigenschaften von MnBi_2Te_4 .

Fig. 3: Interplay of layered structure, intra-layer ferromagnetic order and non-trivial topology of the electronic spectrum results in the unique physical properties of MnBi_2Te_4 .



FORSCHUNGSGEBIET 4:

Vom Material zum Produkt

RESEARCH AREA 4:

Towards Products

Vom Material zum Produkt

Das Forschungsgebiet 4 umfasst Materialsysteme, deren Eigenschaften im Hinblick auf konkrete Anwendungen, Prototypen und Produkte optimiert werden. Dies geschieht in der Regel in enger Zusammenarbeit mit Industriepartnern. Forschungsergebnisse, die wirtschaftliche Bedeutung haben können, werden frühzeitig patentrechtlich geschützt. Eine große Zahl nationaler und internationaler Patente belegt die Praxisrelevanz dieser Themen.

Ein typisches Beispiel sind akustische-Oberflächenwellen-Bauelemente. Diese werden als Frequenzfilter zur Auswahl von Signalübertragungskanälen und Sensoren verwendet. Sie bestehen aus einem piezoelektrischen Einkristallchip, auf dem elektrische in akustische Signale und wieder zurück umgewandelt werden. Das IFW hat auf diesem Gebiet wichtige Innovationsbeiträge geleistet, die direkten Einfluss auf die Produkte haben, z.B. die Verbesserung der Temperaturstabilität und der elektromechanischen Anregung durch Aufbringen eines speziellen Dünnschichtmaterials.

Weitere Projekte in diesem Forschungsgebiet betreffen Materialien für bio-medizinische Anwendungen, Legierungen für hochfeste Werkstoffe, Nanomembranen für flexible magnetoelektronische Bauelemente und Demonstratoren für die Anwendung von Hochtemperatursupraleitern.

Towards Products

This research area comprises materials whose physical, mechanical and chemical properties are to be optimized with respect to certain applications, prototypes and products. Usually this is achieved in close cooperation with partners from industry. In the case that scientific results are of economic importance intellectual property rights are secured. A large number of national and international patents and a high degree of licensing indicate their practical relevance.

A typical example are surface acoustic waves components. These are used in sensors and as frequency filters for the channel selection in signal transition. They consist of a piezo-electric single crystal chip which transforms electric signals in acoustic ones and back. The IFW has contributed a number of innovations in this field, for example a considerable improvement of temperature stability and of electromechanical excitation by a special thin film material.

Further projects in this research area concern materials for bio-medical applications, alloys for high-strength materials, nanomembranes for flexible electronic devices and demonstrators for the application of high-temperature superconductors.

Manipulation of complex biological fluids with microacoustic waves

Cynthia Richard, Armaghan Fakhfour, Melanie Colditz, Friedrich Striggow, Romy Kronstein-Wiedemann¹, Torsten Tonn¹, Mariana Medina-Sánchez, Oliver G. Schmidt, Thomas Gemming, Andreas Winkler

Zusammenfassung

Neue medizinische Therapien basieren zunehmend auf der Isolation von Zellen aus Körperflüssigkeiten, deren Analyse, Biomodifikation und schlussendlich ihrer Rückführung in den Körper. Die hochreine Verarbeitung selbst kleiner Mengen spezialisierter Zellproben ist mit klassischen Labormethoden jedoch sehr aufwendig und teuer, was dem breiten Einsatz von Zelltherapien im Wege steht.

Im SAWLab Saxony des IFW Dresden wurde nun eine mikrofluidische Chiptechnologie für die Zellisolation mit hochfrequenten Schallwellen entwickelt

und auf dieser Basis die Trennung von Blutzellen demonstriert. Diese Chiptechnologie nutzt übliche Verfahren der Mikrotechnologie, welche für die Skalierung zu einer qualitativ hochwertigen und kostengünstigen Chipfertigung ideal geeignet sind.

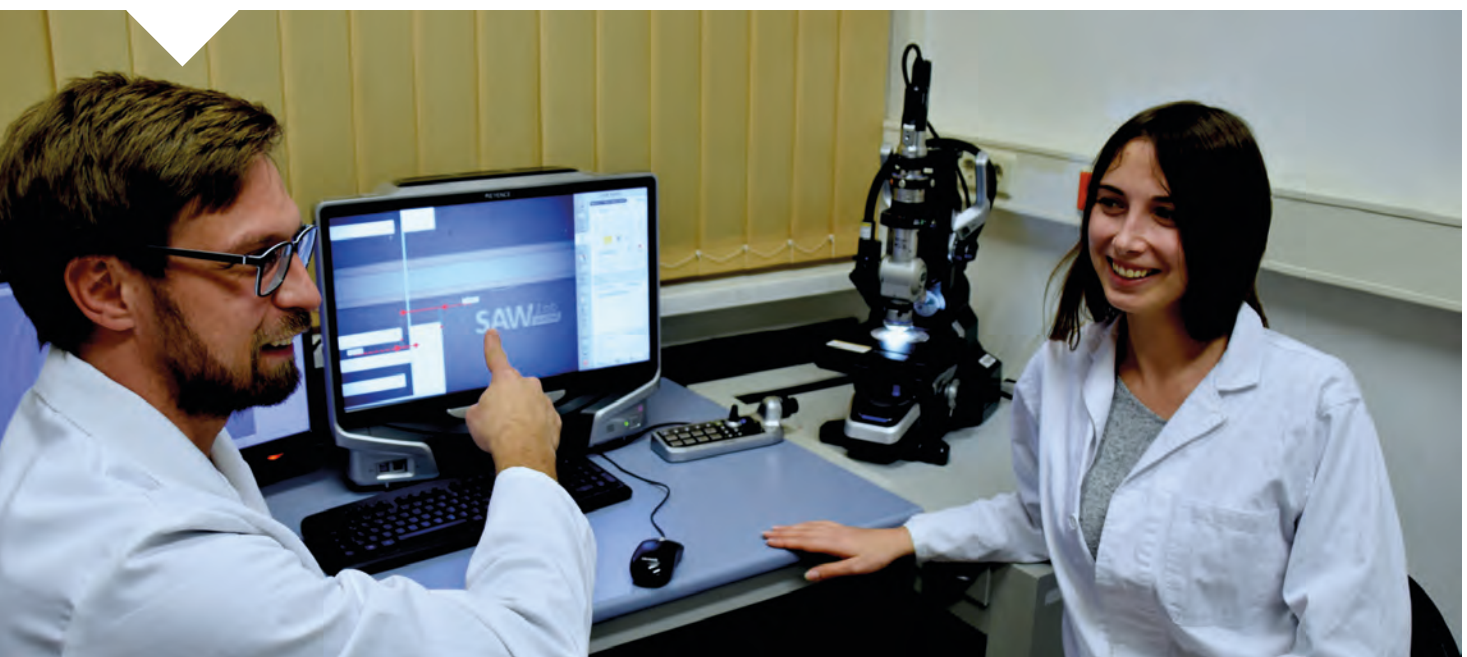
Abstract

New medical therapies require the isolation of cells from body fluids, their analysis, biomodification and, finally, their reapplication to the body. The processing of even small amounts of specialized cell samples with high purity, however, is very time-consuming and expensive using conventional laboratory methods, which stands in the way of a broad application of cell therapies.

At IFW Dresden's SAWLab Saxony, a microfluidic cell isolation technology using high-frequency waves has now been developed and demonstrated for the separation of blood cells. This chip technology is based on semiconductor fabrication processes, which are ideally suited for the simple up-scaling of production for high-quality mass production.

Abb. 1: Andreas Winkler und Melanie Colditz vom Team des SAWLab Saxony am IFW Dresden untersuchen einen Wafer mit hochfrequenten akustofluidischen Chips für Anwendungen in zukünftigen biomedizinischen Lab-on-a-Chip-Systemen.

Fig. 1: Andreas Winkler and Melanie Colditz from the team of IFW's SAWLab Saxony investigate a wafer with high-frequency acoustofluidic chips for applications in future biomedical Lab-on-a-Chip systems.



Acoustofluidics @ SAWLab Saxony

At the SAWLab Saxony, the Competence and Application Center for Acoustoelectronic Fundamentals, Technologies and Devices, of the Leibniz IFW Dresden (www.SAWLab-Saxony.de), researchers investigate new devices and innovative technological principles employing special high-frequency acoustic ("ultrasonic") waves on chip substrates.

The SAWLab Saxony combines the comprehensive acoustoelectronics research activities and expertise of two IFW institutes, i.e. the Institute for Complex Materials (IKM) and the Institute for Solid State Research (IFF), with complementary competences and skills of regional and international research institutes, universities and high-tech companies. This allows IFW Dresden to address economic sectors with high growth dynamics, such as telecommunication, MEMS, sensors and actuators as well as Smart Systems and Life Sciences.

Surface acoustic wave (SAW) devices like high-frequency analog bandpass filters and resonators are already key components for all mobile communication devices, including wireless networks, GSM, Bluetooth and infrared signaling. In their development, the IFW Dresden had a significant influence and fruitful collaborations with major partners from industry. According to Dr. Hagen Schmidt, co-leader of the SAWLab Saxony, this competence in acoustoelectronics is now focused onto research for the second and the third generation of SAW applications, namely i) wireless, autarc sensing at high temperatures (>600 °C) and harsh environments, and ii) SAW-driven acoustofluidics. For the latter, the researchers follow a comprehensive approach considering chip design and manufacturing with task-specific electroacoustic transducers, on-chip integrated fluidic microchannels and functional thin films, as well as chip handling and interconnection to its fluidic and electric peripheral components.

Acoustofluidic cell and particle manipulation

In a recent study, the research group around Dr. Andreas Winkler at the IKM, with assistance from IIN regarding clean-room manufacturing technologies, designed and tested a straight-forward surface acoustic wave (SAW) acoustofluidic device for the enrichment and separation of specific cells from complex

body fluids, like blood, lymph, milk and saliva. As these fluids are highly important for the analysis of a human being's health and as well for the therapy of diseases, their controlled manipulation offers a variety of application fields.

The application of microacoustic fields, i.e. high frequency ("ultrasonic") waves, to liquids is a very promising microfluidic approach aiming for the contactless, precise manipulation of suspended particles, biological cells, cell components and biomolecules. In general, the high-frequency mechanical wave-particle interaction allows for rapid mixing, focusing, trapping, on-demand droplet production and even aerosol generation.

Of specific importance for the recent work, is the ability to manipulate and to separate specific biological components from complex cell suspensions, which is indispensable for liquid biopsies, and for personalized diagnostics and therapy. In acoustofluidic devices, a tiny chip represents the core component. It is built upon a piezoelectric crystal substrate, i.e. lithium niobate (LiNbO_3), that deforms at the application of an electrical field and, vice versa, establishes an electric field upon deformation, a principle used e.g. in electric cigarette lighters or for translation stages with nanometer movement precision. On the surface of these substrates, so-called interdigital transducer (IDT) electrodes for electro-acoustic energy conversion together with microfluidic channels and chambers - containing the liquid to be investigated - are defined using microelectronic techniques. The specific design of the chip, the properties of the involved materials and the technological boundary conditions are decisive for the interaction between excited acoustic waves and particles or cells in the liquid, as well as - like in all acoustic setups - wave effects like reflection, diffraction and interference have to be considered. Here, the SAWLab Saxony is an important player as its research is dedicated to the acquirement of deep insight into the physics of acoustic wave excitation and propagation, the control of the material properties, and the development of advanced methods for manufacturing and analysis of microacoustic devices.

In a recently developed demonstrator, cell suspensions are guided from a suspension reservoir through a tiny channel on the chip surface with the inner diameter smaller than the diameter of a human hair. In

this channel, all cellular components of the suspension are initially focused to a dense line and subsequently separated by size using acoustic radiation forces (ARF) applied through standing surface acoustic waves (sSAW). The acoustic forces thereby create a pressure field which interacts with the cells in a contactless manner and leads to their displacement to so-called pressure nodes, i.e. regions of low pressure change. Conventional acoustofluidic setups employ molded silicone microchannel blocks for the creation of microfluidic channels - an inaccurate, time consuming and costly process hindering the proceeds from lab-based demonstrators to real-world applications. Contrarily, the approach developed by the team of Dr. Winkler uses microchannel walls made from a precise lithographically-patterned epoxy polymer material and a removable silicone cover, the latter with only coarse features. This allows highest precision of all geometrically critical features as well as simple, reproducible production and upscaling.

The demonstration of the device performance in a real world task, was carried out in close collaboration with the DRK Nord-Ost gGmbH and the chair for Experimental Transfusion Medicine of the TU Dresden. It was shown, that the selection of platelets (PLTs, thrombocytes) from a suspension of PLTs and red blood cells (RBCs, erythrocytes) at whole blood concentration, was possible with a substantially higher cell throughput of 40.000 blood cells per second and considerably lower applied power than compared with similar devices as known from literature. This

opens up new possibilities for versatile applications in high-throughput cell manipulation. Furthermore, blood cells and nanoparticles, like exosomes, are often needed to be fully viable for further diagnosis in fluid biopsy applications or for body transfusion in a therapeutic approach. This technology is proven to provide a gentle handling of especially shear sensitive cells and particles while maintaining the cell viability. Additionally, the proposed device is compatible with current (Lab-on-a-Chip) microfabrication techniques allowing for mass-scale chip manufacturing which is crucial to push the technology from lab-based to real-world applications.

To gain insights into the fundamentals of the complex acoustofluidic interaction, highly-demanding, fully-coupled 3D numerical simulations were carried out using the straightforward FEM (finite element method) simulation infrastructure of the IFW. The simulation conditions were chosen based on dedicated electrical, geometrical and acoustical analysis results acquired in the SAWLab Saxony. These simulations allow to access otherwise inaccessible physical effects, i.e. the transient coupling of the wave field into the fluid, the resulting pressure field in the microchannel and, finally, the acoustic forces acting on the particles and their resulting movement.

The simulated results show an ideal match to the experimental observations and offer the first insights into the acoustic behavior of SU-8 polymer as channel wall material. In addition, they allow the prediction of device behavior significant for future chip design.

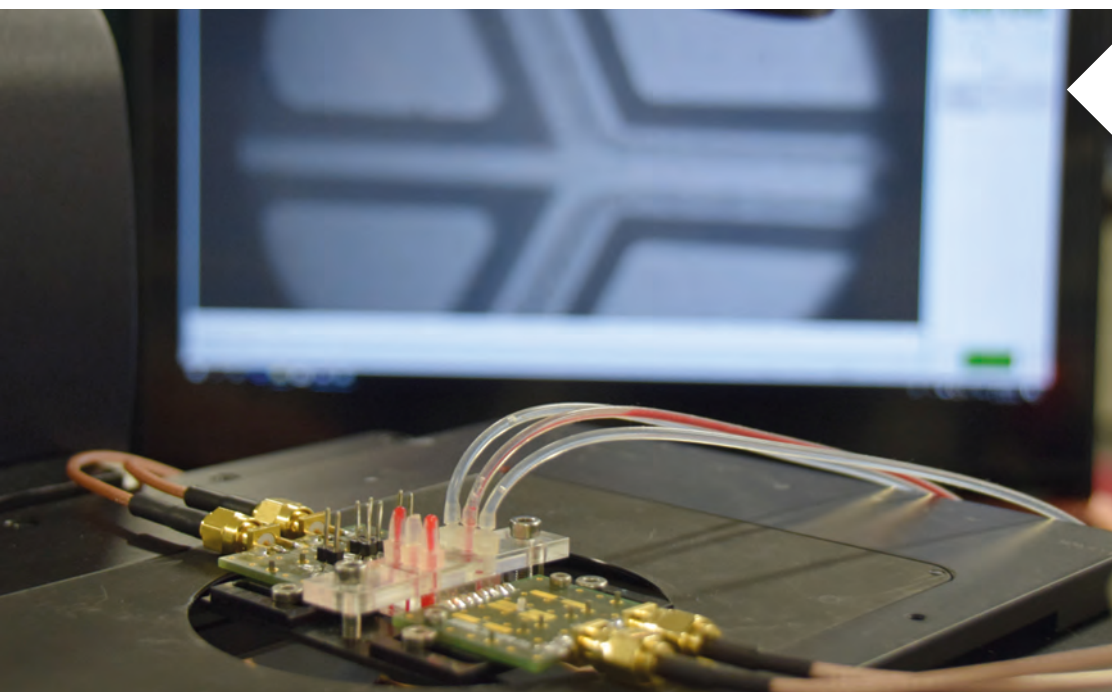


Abb. 2: Am SAWLab Saxony des IFW Dresden entwickelter Demonstrator zur Zelltrennung: Blut und Kochsalzlösung werden über Schläuche einem akustofluidischen Chip zugeführt. Auf diesem bewirken akustische Wellen in einem mikrofluidischen Kanal die Trennung verschiedener Zelltypen aufgrund ihrer charakteristischen Eigenschaften.

Fig. 2: Setup for cell separation developed at the SAWLab Saxony of the IFW Dresden: Blood and saline solution are delivered to an acoustofluidic chip via tubing. On the chip, acoustic waves in a microfluidic channel cause the separation of different cell types based on their characteristic properties

From lab demonstrator to medtech device

Due to the versatile fields of application of the developed technique and the great interest from possible industrial applicants, the researchers are currently pushing forward the transfer from applied research into real-world products, assisted by the IFW Dresden technology transfer office. This involves testing of the setup in specific scenarios in the labs of external partners from research and industry. Furthermore, in 2019, the team was selected to improve their transfer strategy within the start-up incubation program “LifeTechLab”, a coaching platform of the founding initiative Dresden|exists. For their approach to apply the cell separation technique to new biotechnological analysis and therapy methods, the researchers recently were awarded with a prize in the idea phase of “Science4Life Venture Cup”.

References

C. Richard et al., *Lab Chip* 19 (2019) 4043

Funding

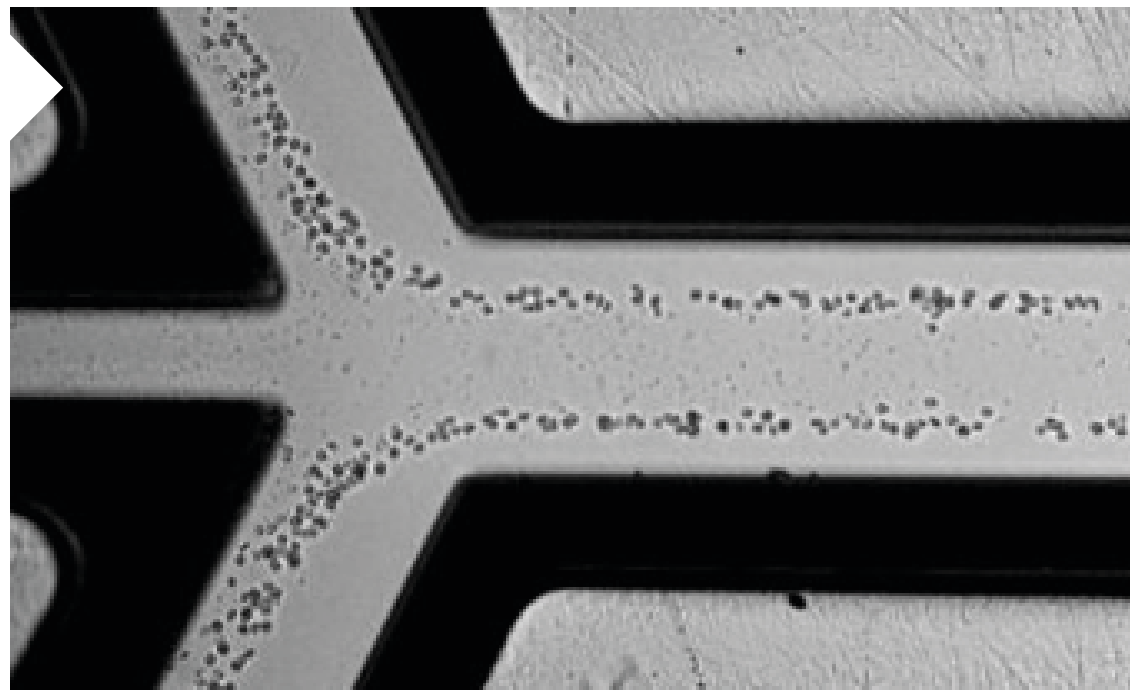
EFRE InfraPro Projekt „ChAMP: Chipbased Acoustofluidic Medtech Platform“

Cooperations

¹⁾ Experimentelle Transfusionsmedizin, Medizinische Fakultät Carl Gustav Carus der TU Dresden/ DRK-Blutspendedienst Nord-Ost gGmbH, Dresden Cells4Therapy / Niederlande.

Abb. 3: Akustische Zelltrennung im mikrofluidischen Kanal: große Zellen, z.B. rote Blutkörperchen, werden zu den Seitenkanälen bewegt, während kleinere Zellen, z.B. Blutplättchen, über den zentralen Kanal abgeführt werden (Flussrichtung von rechts nach links).

Fig. 3: Acoustic separation of blood in the microfluidic channel: larger cells (e.g. red blood cells) are guided to the side channels, while smaller ones (e.g. platelets) leave through the center channel (flow from right to left).



Superconducting magnetic bearings for turbo ring spinning applications

Tilo Espenhahn, Maria Sparing, Günter Fuchs, Kornelius Nielsch, Ruben Hühne, Mahmud Hossain¹, Anwar Abdkader¹, Chokri Cherif¹

Zusammenfassung

Im Rahmen eines gemeinsamen DFG-Projektes mit der TU Dresden wurde eine neue Komponente für das Ringspinnverfahren mit einem supraleitenden Magnetlager entwickelt, mit der die Spinnengeschwindigkeit gegenüber dem konventionellen Verfahren deutlich erhöht werden konnte. Im Rahmen der Untersuchungen wurde die Funktionsweise des Lagers bis zu einer Geschwindigkeit von über 35.000 U/min erfolgreich getestet und sowohl die Bewegung des Magnetringes als auch der dynamische Fadenlauf detailliert analysiert.

Das Leistungspotential des neuen Systems ist damit jedoch noch nicht ausgeschöpft. Deshalb sind grundlegende technologische Weiterentwicklungen an der Ringspinnmaschine geplant, um Spinnengeschwindigkeiten von bis zu 50.000 U/min zu realisieren.

Abstract

Within the scope of a joint DFG project with TU Dresden, a new component was developed for ring spinning using a superconducting magnetic bearing. This allowed to increase the spinning speed significantly compared to the conventional process. As part of the investigations, the operation of the bearing was successfully tested up to a speed of more than 35.000 rpm including a detailed analysis of the magnetic ring movement as well as the dynamic yarn path. However, the potential of the new system has not yet been exhausted. Therefore, fundamental technological studies are planned in order to realize spinning speeds of up to 50.000 rpm.

Abb. 1: Neuer Ringspinnerteststand an der TU Dresden, der Spinnengeschwindigkeiten von bis zu 50.000 Umdrehungen pro Minute erlaubt. Der Kryostat mit dem supraleitenden Magnetlager wurde auf der äußersten rechten Spinnposition eingebaut (links) Neu konzipiertes supraleitendes magnetisches Ringspinnlager während des Spinnprozesses bei 25.000 Umdrehungen pro Minute (rechts).

Fig. 1: New ring spinning tester at TU Dresden designed for spinning speeds up to 50.000 rpm. The cryostat with the superconducting magnetic bearing is installed in the most right spinning position (left). New superconducting magnetic bearing for ring spinning while spinning at 25.000 rpm (right).



Development of an improved superconducting magnetic bearing twist element

Ring-spinning is the most widely used technology for the production of short staple yarn due to the high quality and the flexibility of the process. The continuous ring spinning process converts a loose fiber roving to yarn by drawing, twisting, and winding up on a bobbin. The so-called ring-traveler system thereby induces twist in the processed material by guiding it around the spindle. This technology includes a c-shaped clip, the traveler, which is dragged along a ring surrounding the spindle. However, the rotational speed and hence the productivity of the process is limited by the friction heat between ring and traveler, which can lead to melting of synthetic yarns at high speed. Therefore, the maximum rotational speed achievable in industrial yarn production with a conventional system is limited to less than 25.000 rpm depending on the raw material.

The goal of our DFG-funded project together with the Institute of Textile Machinery and High Performance Material Technology (ITM) at the TU Dresden was to replace the ring-traveler system by a superconducting magnetic bearing (SMB), where a permanent magnet (PM) ring levitates in a stable position above a high-temperature superconductor [1]. We showed in the first project phase that such a SMB system might be successfully used for ring spinning up to a speed of 25.000 rpm producing yarn with a similar quality as in the conventional process. Goal of the second project phase was to increase the spinning speed significantly by using a new ring spinning test system enabling a speed of up to 50.000 rpm. At the same time, a detailed analysis of the SMB behavior as well as of the spinning process at higher speeds were the central aims of our joint studies.

As central part of the project, a new cryostat was constructed and implemented afterwards in the new ring spinning tester (Fig. 1). A superconducting ring composed of 10 bulk $\text{YBa}_2\text{Cu}_3\text{O}_{7-x}$ (YBCO) segments was arranged in this cryostat, which is cooled by liquid nitrogen. Additionally, it is possible to operate the new SMB in the temperature range between 77 K and 65 K by pumping the cryostat down to a pressure of 125 mbar. This allows to modify the bearing properties in a controlled way in order to improve the stability of the system for ring spinning. At the same time, the targeted high rotational speed required an

additional reinforcement of the PM ring to avoid a fracture by the large tangential tensile stresses. Therefore, we designed and build a permanent magnet ring suitable for rotational speeds up to 50.000 rpm by using a shrunk-on high strength Ni-alloy. All developed parts were assembled in the new ring spinning tester and successfully tested afterwards up to a speed of about 35.000 rpm [2].

Characterization of the SMB

In general, such a bearing is characterized by its stiffness and damping parameters. Both properties are of high importance for the use of such a SMB system in the ring spinning process, as numerous forces act on the bearing with high dynamics. These forces arise from the yarn itself as well as from ring rail movements, machine vibrations and thread force oscillations. At the end, one needs to ensure that none of these forces or vibrations excite the bearing to an unstable condition, which leads to a yarn brakeage. Therefore, it is a crucial prerequisite to identify the bearing properties in detail. It was our task to develop suitable methods for characterizing the bearing properties in different spatial directions. The basic principle is to move the permanent magnet ring from its equilibrium position by a defined deflection and to release it afterwards [3]. The resulting damped oscillation is measured by a 3-axis acceleration sensor for all directions. The detailed analysis of the data results in values for the resonance frequency, the bearing stiffness and the decay constants of the SMB system for a given parameter set. As an example, the bearing showed a resonance frequency of $f_{\text{rad}} = 15$ Hz in radial and $f_{\text{ax}} = 30$ Hz in axial direction, respectively, at a temperature of 65 K and a cooling height of 3 mm. The corresponding damping constants are $\delta_{\text{rad}} = 5$ and $\delta_{\text{ax}} = 10$. Compared to the old SMB system with a fixed temperature of 77 K, the decay constants of the vibrations were increased by a factor of 2 due to the temperature reduction, whereas the resonance frequency and the stiffness remained almost constant. Dynamic measurements also showed that the bearing stiffness is independent of deflection range (within a few millimeters) for a given levitation height, whereas the damping depends directly on the deflection and increases with increasing deflection [3]. Additionally, the magnet ring design has a decisive influence on the bearing stiffness. It was shown

with theoretical simulations and measurements that a change in the magnet aspect ratio can increase the radial bearing stiffness from 2.4 N/mm² to a value of up to 4.2 N/mm² [4] (Fig. 2).

Measurement of the magnet movement during spinning

In general, the levitating magnet of the SMB system is accelerated and driven by the thread. It was one task in the project to track the magnet movement in-situ during the spinning process in order to analyze the motion under real processing conditions. Therefore, a position measurement system was developed and implemented in the ring spinning tester (Fig. 3). The movement of the PM ring during spinning is recorded by 5 synchronized optical laser triangulation sensors mounted directly on the ring rail combined with an additional velocity sensor. The optical sensors generate a signal, which is linear to the distance between sensor and magnet with a resolution of up to 300 nm. From the measured distances over time, the movement (inclination and displacement in the x-, y- and z-direction) of the geometric center of the PM ring was calculated using an evaluation software developed in the project (Fig. 4). It was possible to study the magnet ring motion for different yarn quality in the speed range from 10.000 rpm to 21.000 rpm. It was found that the magnet tilt is smaller than 1° for all examined yarn qualities and speeds. Since the tilt remains stationary (i.e. does not change in time) for each cooling position, it is probably connected to

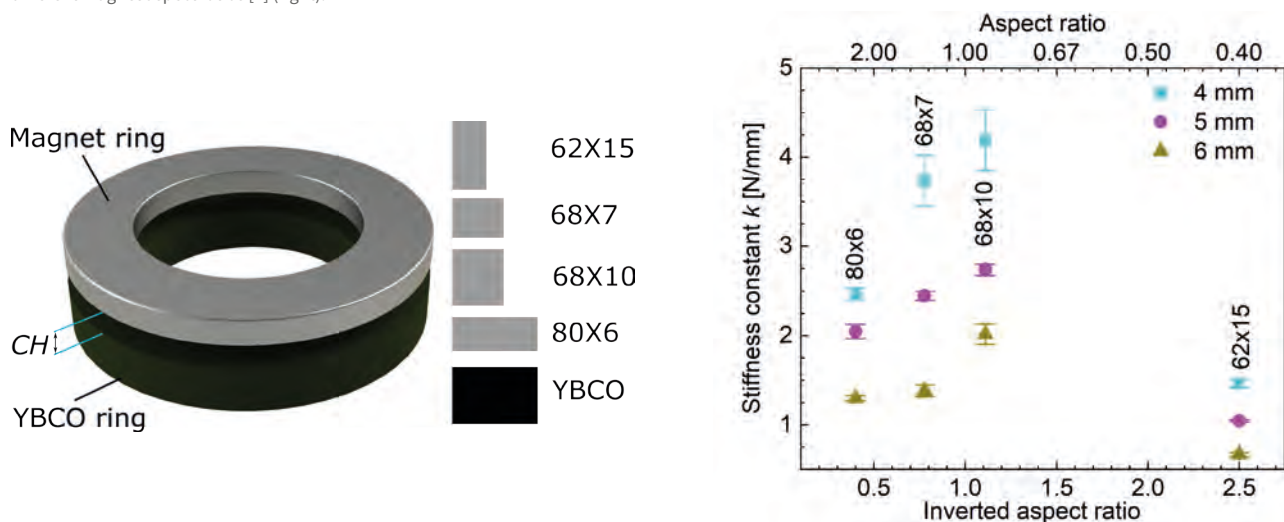
an asymmetric force distribution in the SMB rather than to the axial force component of the thread. The movement of the magnet during spinning is a superposition of a rotation around the axis of the magnet ring with the frequency of the spinning speed and a circular path of the geometric magnet center around the spindle with a speed independent frequency of 18 Hz (Fig. 4). The maximum amplitudes of these movements depend on both speed and yarn properties. The 18 Hz oscillations observed at all spinning speeds might be triggered by low frequency machine vibrations near the SMB resonance frequency of 15 Hz, a force below 0.3 N would be sufficient to generate the observed peak amplitudes. More detailed studies are required to understand the origin of the different movements in detail.

Loss measurements on the SMB

The damping of the SMB comprises both the oscillation decay constant already mentioned above as well as the reduction of the rotational speed of the PM ring due to air friction and dissipative processes in the superconductor. The influence of the air friction was evaluated by experiments on the force-free run-off behavior of the PM ring without a thread resulting in an attenuation constant of $7 \cdot 10^{-4} \text{ s}^{-1}$ for the lower speed range. In praxis, a rotation of 200 rpm takes almost an hour to drop to 20 rpm. Dissipative processes in the YBCO ring are also responsible for the damping of vibrations of the magnet. In particular, tilting vibrations of the PM ring may play a role.

Abb. 2: Anordnung des Magnet- und Supraleiterrings mit schematischer Darstellung der Ringquerschnitte für die untersuchten Aspektverhältnisse, CH ist der Einkühlabstand (links). Gemessene laterale Steifigkeit des Lagers für verschiedene Aspektverhältnisse und Einkühlabstände (rechts).

Fig. 2: Magnet and YBCO ring arrangement and comparison of the different studied magnet ring aspect ratios, CH is the cooling height (left). Measured lateral stiffness for different magnet aspect ratios [4] (right).



Associated with this behavior are hysteresis losses in the superconductor, which depend on a number of bearing parameters. These dissipative processes were investigated with calorimetric loss measurements by detecting the additional nitrogen evaporation with a thermal gas flow meter in the cryostat while keeping the superconductor ring at constant temperature. The measurement design made it possible to set a speed of up to 5.000 rpm and the tilt angle of the magnetic ring up to 5°. Measurements with the smallest possible cooling distance showed that the hysteretic losses due to the inclination of the magnet are almost neglectable, i.e. a value of 20 mW was determined at 2° tilt and 5.000 rpm. The loss decreases with both decreasing speed and with decreasing tilt angle. In the meantime, it was found that the tilt of the PM is smaller and does not change with time, so that no additional hysteresis losses are expected inside the superconductor.

Conclusion

Our studies showed that superconducting magnetic bearings are a suitable alternative to conventional ring-traveler system in ring spinning despite the more complex design as they might be used at significantly higher speeds. It was shown that the bearing properties are sufficient for stable spinning with high quality. A maximum spinning speed of about 35.000 rpm was reached. Above this value, the thread tension limits the process, which requires changes in the yarn path, whereas the SMB itself is suitable for higher speeds. Measurements of the magnet motion showed a superposition of different movements and only a small tilt. However, machine vibrations in the range of the bearing resonance frequency may excite the bearing. Nevertheless, the SMB stabilizes itself even in this case due to the deflection-dependent damping. It was also found that the hysteretic losses in the superconductor are neglectable for the observed displacement values. Further studies are planned to stabilize the SMB against external disturbances and to modify the yarn path to enable even higher spinning speeds.

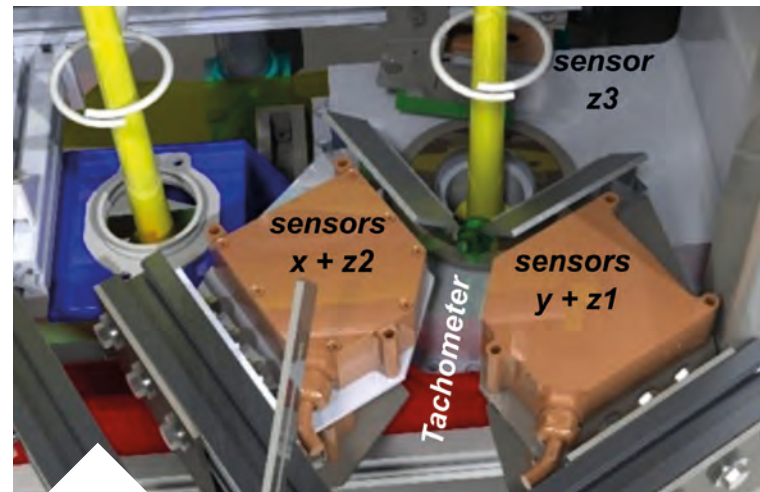


Abb. 3: Messaufbau zur Bestimmung der Magnetringposition während des Spinnprozesses.

Fig. 3: Measurement set up for in-situ magnet ring position measurement.

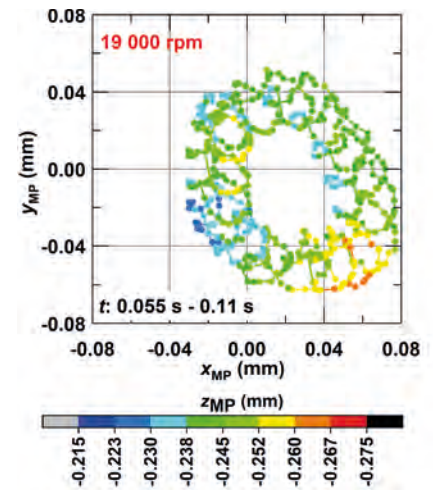


Abb. 4: Beispiel für die Bewegung des Magnetringzentrums während des Spinnprozesses bei 19.000 Umdrehungen pro Minute.

Fig. 4: Exemplary in-situ measurement of the magnet ring displacement during spinning at 19.000 rpm.

References

- [1] M. Hossain et al., Text. Res. J. 84 (2014) 871
- [2] M. Hossain et al., Text. Res. J. (2020) accepted (DOI: 10.1177/0040517519879899)
- [3] M. Sparing et al, IEEE Trans Appl. Supercond. 26 (2016) 3600804.
- [4] T. Espenhahn et al., J. Phys. D: Appl. Phys. 53 (2020) 035002.

Funding

DFG SCHU 1118/12-1,12-2

Cooperations

¹⁾ Institute of Textile Machinery and High Performance Material Technology (ITM), Technische Universität Dresden, Germany. IFW Research Technology.

Bioabsorbable Fe-Mn-based alloys for medical applications

Julia Hufenbach, Monica Fernandez-Barcia, Fabian Kochta, Samer Kurdi¹, Andrea Voss, Volker Hoffmann, Steffen Oswald, Horst Wendrock, Christine Damm, Ulrike Wolff, Margitta Uhlemann, Salvador Pane², Anja Lode³, Uta Kühn, Annett Gebert

Zusammenfassung

Bioabsorbierbare Metalle sind neue Materialien für medizinische Anwendungen, bei denen lediglich eine temporäre Funktionalität erforderlich ist. Anschließend zersetzen sie sich in nicht-toxische Bestandteile. Wir stellen die Synthese und Eigenschaftseinstellung Fe-Mn-basierter Legierungen für diesen Einsatz anhand von zwei Beispielen vor. Die Legierung Fe-30Mn-1C-0.025S mit austenitischer Matrix und MnS-Ausscheidungen ist ein aussichtsreiches bioabsorbierbares Implantatmaterial. Entsprechende Stent-Prototypen wurden bereits durch selektives Laserschmelzen erzeugt. Darüber hinaus wurden Fe-Mn-Dünnschichten mit umweltverträg-

lichen Techniken, Elektrodeposition und Magnetron-Sputtern hergestellt und zeigen ein vielversprechendes Eigenschaftsspektrum für den Einsatz im bioelektronischen Bereich.

Abstract

Bioabsorbable metals are new materials for applications in the medical field where only temporary functionality is required, then they degrade leaving non-toxic products. We present two examples of synthesis and property adjustment of Fe-Mn-based alloys with good perspectives for medical use. The solidified Fe-30Mn-1C-0.025S alloy with austenitic matrix phase and MnS precipitates has a high potential as bioabsorbable implant material, whereby stent prototypes were already successfully manufactured by selective laser melting. In addition, Fe-Mn-based thin films with wide compositional range were produced by sustainable techniques, i.e. electrodeposition and magnetron sputtering, and reveal a spectrum of promising properties for use in bio-electronic devices.



Abb.1: Korrosionslabor – Tests von Fe-Mn-C-basiertem Stentmaterial

Fig. 1: Corrosion Lab – testing of Fe-Mn-C-based stent material

In recent years, “bioabsorbable metallic materials” or “biodegradable metals” (BM) have revolutionised the field of metallic biomaterial research. Different to classical metallic biomaterials which are designed for permanent disposition in the human body with appropriate long-term stability of mechanical integrity and corrosion resistance, this new material class will provide a temporary biofunctionality which is necessary to support a healing process and then degrade with formation of only non-toxic residues. According to ASTM-F3160, BMs are metals expected to corrode gradually in vivo with an appropriate host response elicited by released corrosion products, which can pass through or be metabolized or assimilated by cells and/or tissue, and then dissolve completely upon fulfilling the mission to assist with tissue healing with no implant residues [1]. This way revision surgery of implants which is often related with various health risks can be avoided. Meanwhile bioabsorbable metals are being developed for a variety of applications ranging from bulk materials for bone implants (osteosynthesis material), via delicate stents for the cardiovascular system up to thin films for transient electronics. Besides magnesium- and zinc-based alloy systems, iron-based materials are getting more and more in the focus of research. To overcome the limited corrosion rate of pure iron (Fe), manganese (Mn) is added as more reactive alloying element. Moreover, small additions of non-metals (carbon C, sulphur S, boron B) are effective in tailoring the alloy microstructure and in consequence, to attain an adequate combination of mechanical and corrosion properties. In the following we present two examples of our research work in this field.

Fe-Mn-C-based alloys for stent applications

Fe-Mn-based alloys are promising candidates as bioabsorbable stent materials [2]. Within a project funded by the German Research Foundation (DFG), novel Fe-30Mn-1C(-B/S) alloys were developed, whereby the influence of microalloying with boron (B) or sulfur (S) and of high solidification rates on the microstructure as well as on selected mechanical, corrosion and biological properties were investigated. Exemplary, the effect of 0.05 wt.% B and 0.025 wt.% S on the Fe-30Mn-1C base system is described [3-5]. All manufactured Fe-Mn-C(-B/S) alloys possess a fine austenitic matrix due to the high solidification

rate in the applied casting process. Further, in the Fe-30Mn-1C-0.05B alloy, mixed borocarbides of type $(\text{Fe},\text{Mn})_{23}(\text{B}_3\text{C}_3)$ are formed, while in the Fe-30Mn-1C-0.025S system, manganese sulfides of type $(\text{Fe}_{0.3}\text{Mn}_{0.7})\text{S}$ were detected. In quasi-static tensile tests all cast Fe-Mn-C(-B/S) alloys exhibited a significantly increased yield and ultimate tensile strength compared to a bioabsorbable Fe-30Mn reference system as well as to AISI 316L stainless steel, a clinically used material which is considered as a benchmark material for stent applications with regard to the mechanical properties. In addition, a good plasticity was observed for the novel developed alloys, which originates, among other effects, from a pronounced twinning induced plasticity (TWIP) effect. Regarding the influence of microalloying, it became apparent, that the average offset yield and ultimate tensile strength of Fe-30Mn-1C are successfully improved by microalloying with B and S. This enhancement of the strength can be traced back to precipitation hardening due to the formation of finely distributed borocarbides as well as manganese sulfides in the respective alloy [3,5].

Potentiodynamic polarization measurements in simulated body fluid (SBF) indicated that the Fe-Mn-C(-B/S) alloys show generally higher corrosion rates than the 316L and Fe-30Mn references [2-4]. The polarization curves of all Fe-Mn-based alloys show a similar active dissolution behavior. However in comparison to Fe-30Mn-1C-0.05B and the Fe-30Mn-1C base alloy, for the Fe-30Mn-1C-0.025S alloy a shift of the corrosion potential to more negative values as well as an enhanced corrosion current density were detected. This indicates an enhanced corrosion rate due to sulfur addition, which is due to preferentially dissolving manganese sulfide precipitates acting as initiation sites for localized corrosion. In the alloy modification with boron, additional selective corrosion along the interface between the austenitic matrix and the borocarbides could be detected, which can result in a borocarbide detachment. This is regarded critically considering potential implant applications. First in vitro cytotoxicity tests with fibroblast cells which were performed at the Centre for Translational Bone, Joint and Soft Tissue Research (University Hospital Dresden and the Medical Faculty Carl Gustav Carus of Dresden University of Technology) indicated that microalloying with boron and sulfur does not affect the cytocompatibility [3].

In conclusion, microalloying with sulfur presents an

effective method for further enhancing the mechanical and corrosion properties of Fe-30Mn-1C. The novel designed Fe-30Mn-1C-0.025S alloy shows a high potential for application as bioabsorbable stent material. Recently, stent prototypes out of the designed alloy were successfully manufactured by selective laser melting (Fig. 2) and are currently further investigated.

Fe-Mn-based thin films for transient electronics

Transient electronics is a rapidly evolving field that is focused on the development of biodegradable, bioresorbable, biocompatible and environmentally friendly electronic devices for a variety of applications such as for biomedical or environmental sensors [6]. Often, polymers are so far utilized for those devices as a substrate or packaging layer. However, they do not properly meet the pursued properties such as high mechanical stability or good conductivity. Fe-Mn-based compounds are considered also here as promising new materials to substitute polymeric materials. For their implementation in transient electronic technology, suitable synthesis techniques such as electrodeposition or magnetron co-sputtering are to be employed to obtain thin or thick films with appropriate properties. Nowadays, integrating sustainability with technological progress is one of the major challenges in modern society. Our project on Fe-Mn-based films was embedded in the EU-ITN SELECTA (Smart ELECTrodeposited Alloys for environmentally sustainable applications: from advanced protective

coatings to micro/nano robotic platforms), a training network focussing on the “green” electrochemical synthesis and characterization of advanced functional metallic layers and microstructures.

An electrochemical approach to prepare Fe-Mn-based films based on the elemental electrodeposition of Fe and Mn [7] was developed. Fe-Mn based films were potentiostatically deposited from acidic water-based electrolytes using various sulfate salt concentrations as sources for Fe^{2+} and Mn^{2+} ions as well as ammonium sulfate, boric acid and glycine. Different ratios of $\text{Mn}^{2+}:\text{Fe}^{2+}$ ions in the electrolyte led to metallic and oxide-based FeMn layers. Fig. 3 shows a typical cyclic voltammetry curve (green) with the corresponding electrochemical quartz crystal microbalance mass change curve (blue) measured in a selected electrolyte. These sets of curves are used to determine the different potential ranges at which the deposition (reduction) and the dissolution (oxidation) of the metals in the electrolyte take place. The obtained layer samples were characterized regarding their structure and composition and their resulting magnetic, corrosion and biocompatibility performance. Those data were compared with those of thin films prepared by magnetron co-sputtering.

The electrodeposited Fe-Mn films showed different crystalline structures depending on their composition: for Mn contents < 15 wt.% they were metallic with a body-centered cubic (bcc) Fe structure and for 16-24 wt.% Mn content they were oxidic with face-centred cubic (fcc) structure. Glycine, which was used as an additive in the electrolyte, led to less-cra-

Abb.2: Bioabsorbierbare Fe-Mn-C-basierte Stentstrukturen hergestellt mittels selektivem Laserschmelzen (SLM).

Fig. 2: Bioabsorbable Fe-Mn-C-based stent structures manufactured by selective laser melting (SLM).



cked film morphologies and affected the Mn content. Magnetron co-sputtered films contained between 10 and 70 wt.% of Mn and were metallic in the whole compositional range. Differently to the electrodeposited films, they revealed a well-defined bcc structure that changed its symmetry when the Mn content increased. All synthesized films exhibited a soft magnetic behaviour, a key characteristic to its possible future application in the medical field. To assess the degradability of the films, their corrosion behaviour was evaluated by electrochemical studies in NaCl solutions. A shift to more negative corrosion potential values was observed when the Mn content in the film increased, which indicates the anticipated enhanced corrosion activity. In vitro cytocompatibility tests revealed high biocompatibility characteristics with a cell viability of 85% even for the Mn-richest sputtered films while electrodeposited mostly oxide films showed a higher trend for toxicity [8]. These results pave the way for Fe-Mn film preparation with biocompatible characteristics through low-cost and environmentally friendly techniques and, therefore, present a possible alternative to the use of polymers towards (bio-)absorbable parts of transient devices.

Publications

- [1] Y. Fu et al., *Adv. Funct. Mater.* 29 (2019) 1805402.
- [2] S. Loffredo et al., *Acta Biomater.* 98 (2019) 103.
- [3] J. Hufenbach et al., *Mater Des.* 142 (2018) 22.
- [4] A. Gebert et al., *Mater Corr.* 69 (2018) 167.
- [5] J. Hufenbach et al., *Mater Lett.* 186 (2017) 330.
- [6] H. Cheng, V. Vepachedu, *Theor. Appl. Mech. Letts.* 6 (2016) 21.
- [7] M. Fernandez-Barcia et al., *Surf. Coat. Technol.* 334 (2018) 261.
- [8] M. Fernandez-Barcia et al., *Surf. Coat. Technol.* 375 (2019) 182.

Funding

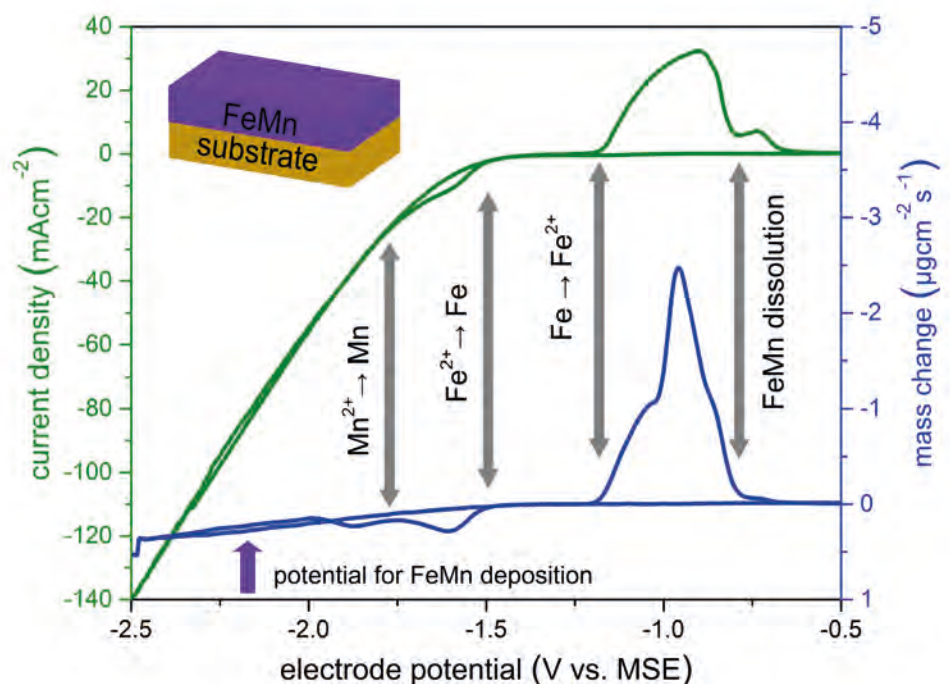
DFG, EU-ITN SELECTA

Cooperations

- ¹⁾ University of Cambridge (UCAM), UK.
 - ²⁾ Swiss Federal Institute of Technology Zürich (ETH), Switzerland.
 - ³⁾ University Hospital Carl Gustav Carus and Faculty of Medicine, Dresden University of Technology (TUD), Germany.
- Universitat Autònoma de Barcelona (UAB), Spain.

Abb. 3: Zyklovoltammetrie und Massenänderungskurven, die die katodische Deposition und die anodische Auflösung von Fe-Mn in einem Fe(2+) und Mn(2+)-haltigem wässrigen Elektrolyten beschreiben; dünne Filme wurden bei einem Potential von -2.2 V vs. MSE erhalten.

Fig. 3: Cyclic voltammetry and corresponding mass change curves describing cathodic deposition and anodic dissolution of Fe-Mn in a Fe(2+) and Mn(2+) containing water-based electrolyte; thin films were obtained at a potential of -2.2 V vs. MSE.



Novel anti-perovskites (Li_2M)SO as bi-functional cathodes for Lithium-ion batteries

Mikhail Gorbunov, Sebastian Maletti, Steffen Oswald, Lars Giebeler, Salvatore Carrocci, Nico Gräßler, Silke Hampel, Martin Valldor and Daria Mikhailova

Zusammenfassung

Neue Oxysulfide, die in einer Anti-Perowskit-Struktur kristallisieren, stellen vielversprechende Kathoden für Li-Ionen Batterien dar, weil sie hohe spezifische Kapazitäten besitzen, kostengünstig und leicht herzustellen sind. Wir haben am Beispiel von (Li_2Fe)SO mithilfe von operando und ex situ spektroskopischen und XRD Methoden (Abb.1) den Redoxmechanismus während des Ladens und Entladens der Batterie untersucht. Während des Ladens wird zuerst Eisen von 2+ auf 3+ und dann Schwefel partiell auf S^0 reversibel oxidiert. Allerdings sind die dabei auftre-

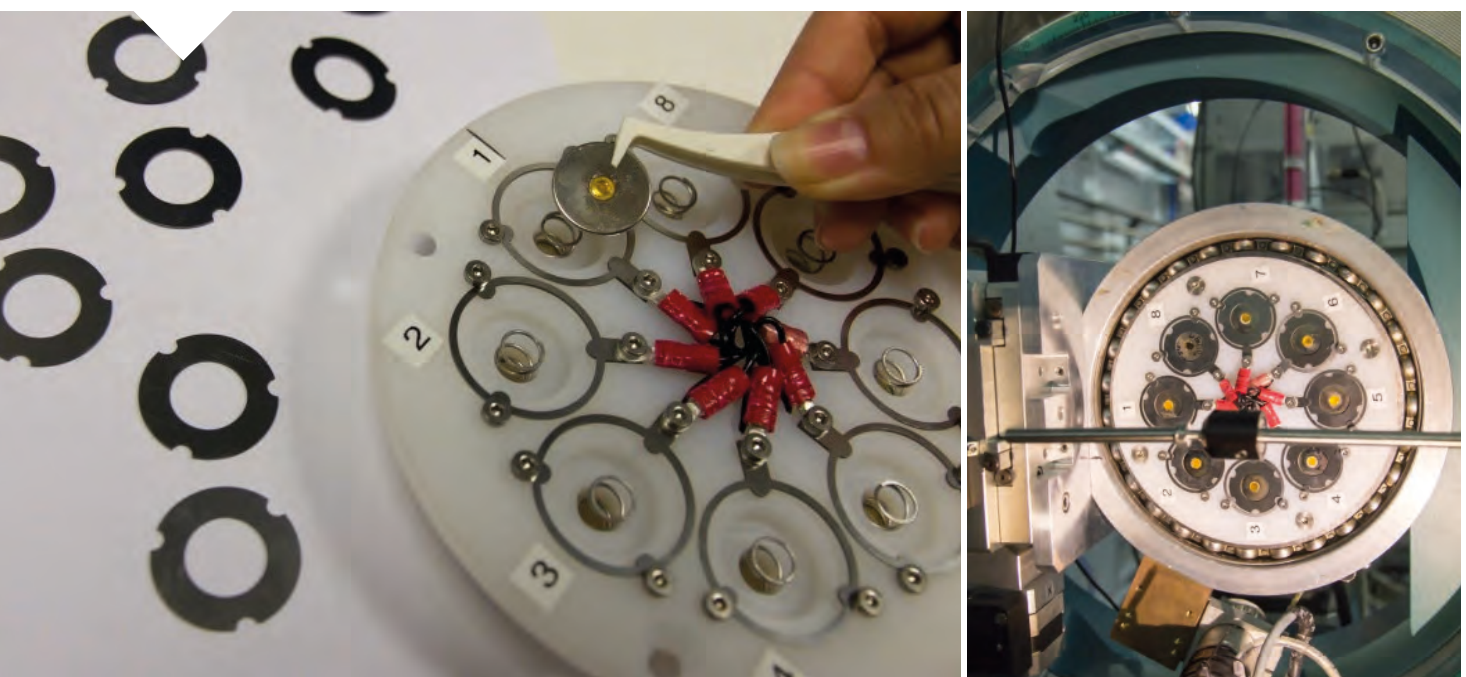
tenden strukturellen Änderungen im Material irreversibel. Um die Strukturstabilität von (Li_2Fe)SO zu erhöhen, wurden spezielle Strategien wie Kationendotierung erfolgreich angewandt.

Abstract

Novel oxysulfides in the anti-perovskite structure exhibit promising performance as cathodes for Li-ion batteries, since they show high specific capacity, are low-priced and can be easily synthesized. Using (Li_2Fe)SO in the battery as an example, we applied operando and ex situ spectroscopic and XRD techniques (Fig.1) to investigate the redox reaction mechanism during charge and discharge. At low charging, Fe is oxidized from +2 to +3, whereas at higher charging S^{2-} is also partly oxidized to S^0 , suggesting a cathode bifunctionality. Irreversible structural changes were also observed during battery cycling. Special approaches like partial cation doping impede sulfur redox and increase structural stability in the operating battery.

Abb. 1: Probenhalter mit 8 in situ Knopfzellen für operando Röntgenbeugung (XRD) und Röntgenabsorptionsspektroskopie (XAS) an einer Synchrotronquelle (links) und während des Betriebes am Synchrotron ALBA in Spanien (rechts).

Fig. 1: Sample holder with 8 in situ electrochemical cells for operando XRD and XAS measurements at a synchrotron source (left), and during operation at ALBA synchrotron in Spain (right).



Iron-containing electrode materials have revolutionized the commercial battery market for almost two decades after introduction of pyrite-type FeS_2 in primary, and olivine-type LiFePO_4 in secondary lithium-ion batteries, operated at room-temperature [1-3]. These iron-based compounds are environmentally more friendly and cost effective in contrast to cobalt- and nickel-based ones. Recently, novel cubic antiperovskites $(\text{Li}_2\text{Fe})\text{ChO}$ ($\text{Ch} = \text{S}, \text{Se}$) with a shared cation position in the anti-perovskite structure (Fig. 2) were synthesized, and their preliminary characterization as cathodes in lithium-ion batteries showed promising properties [4]. In the present project, we deepened our knowledge about the reaction mechanism in $(\text{Li}_2\text{Fe})\text{SO}$ in operating batteries [5] and proposed some strategies to improve its electrochemical performance towards commercial application.

Electrochemical studies

The $(\text{Li}_2\text{Fe})\text{SO}$ material exhibits a theoretical specific capacity of 227 mAh g^{-1} for the reversible extraction and insertion of 1 Li per formula unit, much higher than for the commercially established LiFePO_4 (170 mAh g^{-1}). Cycling of a battery with a $(\text{Li}_2\text{Fe})\text{SO}$ cathode, metallic Li-anode, and an ether-containing electrolyte with LiTFSI salt, which is commonly used in Li-S batteries, yields a promising electrochemical performance at different current rates. On varying the current density (the charging/discharging rate) during 60 subsequent charge-discharge cycles, higher rates decrease the specific capacity, as expected, but the material seems to recover some of its capacity after cycling at higher rates: the first cycles at 0.1C start at about 270 and end at 250 mAh g^{-1} while the subsequent 1C cycles remain close to 190 mAh g^{-1} ; However, the following 0.1C cycles begin again close to 220 mAh g^{-1} .

The same tests with the carbonate-containing LP30 electrolyte, usually used in Li-ion batteries, provided lower absolute capacity values and much less stable cycling life, thus pointing to a possible involvement of sulfur into the redox process. Moreover, slow cycling of the battery (with a lower current rate) results in much faster capacity loss.

During the first cycle, a large hysteretic effect in the ionic conductivity, extracted from electrochemical galvanostatic titration technique (Fig. 3), is observed between the charging and discharging processes: in

the range of 2.0–2.6 V, Li extraction (battery charge) proceeds with three orders of magnitude higher than that of subsequent Li insertion (battery discharge). The hysteretic behavior might deal with different reaction mechanisms during battery charge and discharge.

Redox reaction mechanism

In order to understand the reaction mechanism in the $(\text{Li}_2\text{Fe})\text{SO}$ cathode during charge and discharge including changes in the crystallographic and electronic structures, operando X-ray synchrotron diffraction (XRD) and X-ray absorption spectroscopy (XAS) as well as ex situ X-ray photoelectron (XPS) and Mössbauer spectroscopy techniques were applied. For operando XRD and XAS studies, a special set-up was developed at IFW Dresden together with Karlsruhe Institute of Technology (KIT), which allows simultaneous measurements of eight electrochemical cells (Fig.1).

According to operando XRD studies, the long-range atomic ordering has partly broken down already during the first Li extraction and following insertion, because main diffraction peaks are strongly broadened with reduced absolute intensity, which is due to the loss of crystallinity and introduction of atomic disorder on the local scale. Further, additional reflections appear at low diffraction angles, which might be either an unknown product from a reaction between the carbonate-containing electrolyte and cathode material, a second phase as a product of phase transformation, or as a result of a structural distortion providing superstructure reflections. The reinsertion of Lithium results in irreversible structural changes and an amorphization of the material after several cycles. Operando XAS data confirmed oxidation of Fe during Li-removal from $(\text{Li}_2\text{Fe})\text{SO}$. However, the spectroscopically determined Fe oxidation state remains slightly lower than the expected value, as estimated by the total charge in the electrochemical process. This discrepancy between XAS and electrochemical data might correspond to a partial, simultaneous oxidation of S^{2-} upon Li extraction. This suggestion was verified using XPS studies on $(\text{Li}_x\text{Fe})\text{SO}$ materials with different states of lithiation. In the composition range between $(\text{Li}_2\text{Fe})\text{SO}$ and $(\text{Li}_{1.5}\text{Fe})\text{SO}$ only S^{2-} was detected while further delithiation resulted in the coexistence of S^{2-} and S^0 species.

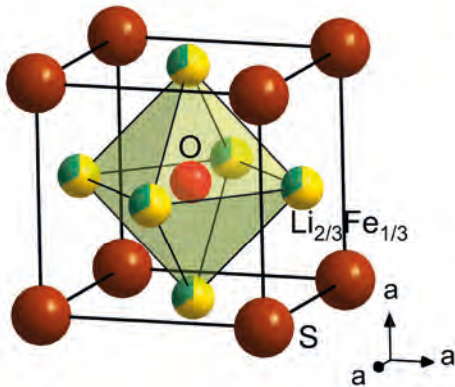


Abb. 2:
 Anti-Perovskit-
 Struktur von
 (Li₂Fe)SO.

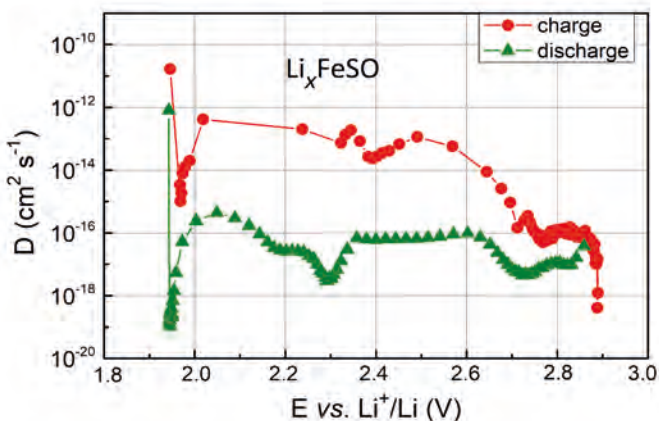
Fig. 2:
 Anti-perovskite
 structure of
 (Li₂Fe)SO.

Summary and strategies for improvement of battery performance

Based on comprehensive studies of the reaction mechanism, the main features of (Li₂Fe)SO as a cathode material in Li-ion batteries can be summarized as following: i) The material shows much more stable cycling life in the ether-based electrolyte commonly used in Li-S batteries, than in the carbonate-based LP30 which is used in Li-ion batteries. ii) The crystal structure of the material suffers under Li-removal and insertion. After several times charging and discharging of the battery, the material becomes almost amorphous. iii) At the beginning of the battery charging, Fe is oxidized as a consequence of the Li-removal. Further battery charging results in oxidation of both, Fe and S. Thus, a bi-functionality of the material with regard to participation of both, cationic and anionic parts, in the redox reaction mechanism, can be proposed.

Abb. 3: Lithium-Diffusionskoeffizient (D_{Li}) während des ersten Lade- und Entladezyklus.

Fig. 3: Lithium chemical diffusion coefficient (D_{Li}) during the first charging and discharging cycles.



Therefore, following strategies for stable, long-term cycle life of an anti-perovskite material in Li-ion batteries can be proposed: i) Optimization of the cation composition through partial substitution of Fe by other electrochemically active or inactive metals to enhance the structural stability. ii) Optimization of the anion composition via partial substitution of sulfur through other anions. iii) Optimization of the electrolyte composition, usage of solid-state electrolytes. The chemical flexibility of the anti-perovskites was already extended on the Mn- and Co-analogues [6]. Although (Li₂Co)SO and (Li₂Mn)SO materials themselves demonstrate lower specific capacities than (Li₂Fe)SO, they represent an outstanding chemical optimization potential for battery application, similar to the impact of transition metals Ni, Co and Mn on the electrochemical performance in well-known NMC cathodes for Li-ion batteries.

References

- [1] A. K. Padhi, K. S. Nanjundaswamy, J. B. Goodenough, *J. Electrochem. Soc.* 1997, 144, 1188–1194.
- [2] C. Daniel, J. O. Besenhard, Eds. *Handbook of Battery Materials*, 2nd ed.; Wiley-VCH: Weinheim, Germany, 2012.
- [3] Y. Shao-Horn, Q. C. Horn, *Electrochim. Acta* 2001, 46, 2613–2621.
- [4] K. T. Lai, I. Antonyshyn, Yu. Prots, M. Valldor, *J. Am. Chem. Soc.* 2017, 139, 9645–9649.
- [5] D. Mikhailova, L. Giebeler, S. Maletti, S. Oswald, A. Sarapulova, S. Indris, Z. Hu, J. Bednarcik, M. Valldor, *ACS Applied Energy Materials*, 2018, 1, 6593–6599.
- [6] K. T. Lai, I. Antonyshyn, Y. Prots, M. Valldor, *Inorg. Chem.* 2018, 57, 13296–13299.

Funding

European Union: ERDF-European Regional Development Fund.
 Free State of Saxony: 100350438 (LUKSIK).

Cooperations

KIT (Germany)
 TU Dresden (Germany)
 University of Oslo (Norway)
 DESY (Germany)
 ALBA (Spain)



Zahlen und Fakten 2019

Das IFW ist eines der größten Forschungsinstitute Sachsens und Mitglied der Leibniz-Gemeinschaft. Als Leibniz-Institut mit gesamtstaatlicher Bedeutung wird das IFW gleichermaßen vom Bund und dem Land Sachsen gefördert. Wir unterhalten enge Kooperationen mit Universitäten, anderen außeruniversitären Forschungseinrichtungen und Partnern aus der Industrie auf nationaler und internationaler Ebene.

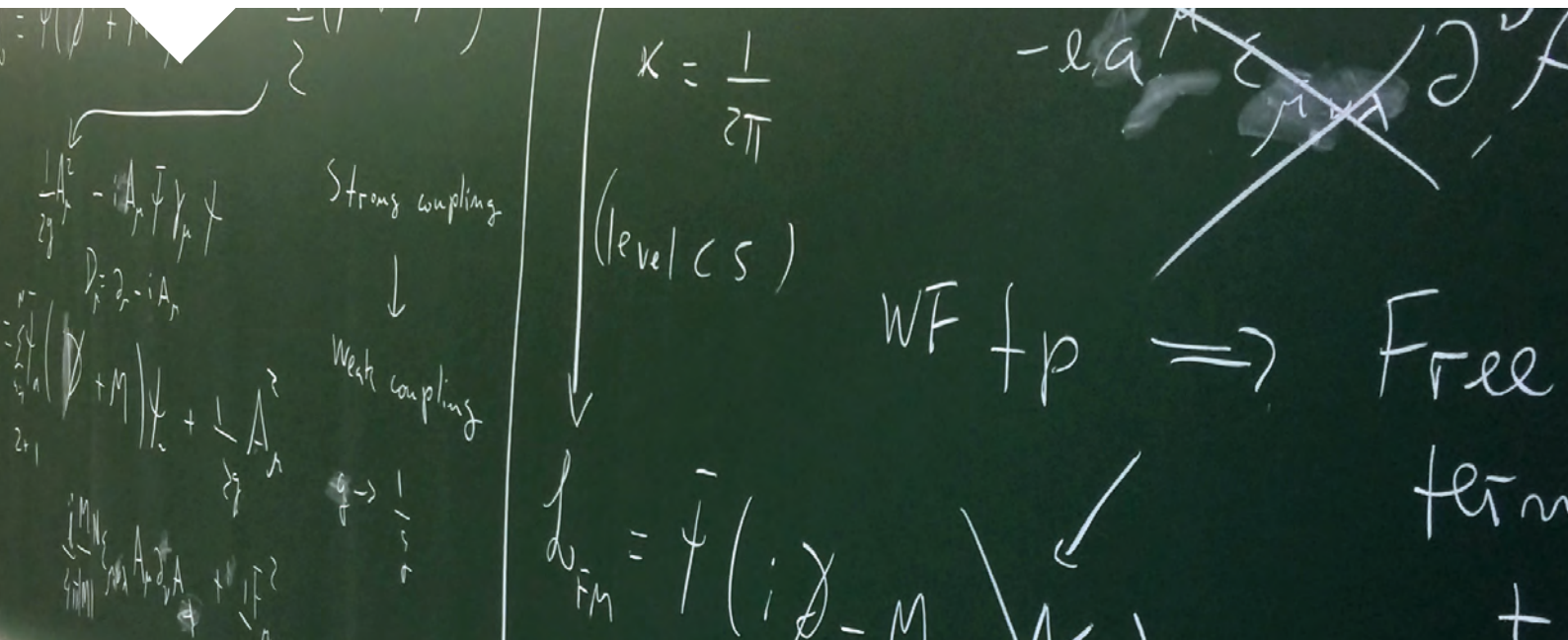
Unsere Aufgabe ist neben dem wissenschaftlichen Auftrag auch die Ausbildung von Nachwuchs im wissenschaftlichen, technischen und administrativen Bereich.

Sowohl Gleichberechtigung als auch Familienfreundlichkeit sind erklärte Ziele des IFW Dresden. Im Jahr 2019 lag der Frauenanteil in wissenschaftlichen Positionen bei 24 Prozent und der Anteil von Frauen in wissenschaftlichen Führungspositionen bei 27 Prozent. Das IFW unterstützt seine Beschäftigten dabei, Familienleben und berufliche Anforderungen in Einklang zu bringen und stellt sich regelmäßig dem Audit „berufundfamilie“.

Facts und Figures 2019

IFW is one of the largest research institutes in Saxony and a member of the Leibniz Association. As a Leibniz Institute of national importance, the IFW is supported by the federal government and the state of Saxony. We maintain national and international cooperations with universities, other research institutions and industrial partners. In addition to the scientific mission, our task is the training of the scientific, technical and administrative staff.

Equality and family friendliness are declared goals of IFW Dresden. In 2019, the proportion of women in scientific positions was 24 percent and the proportion of women in scientific management positions 27 percent. IFW supports its employees in reconciling family life and professional requirements and regularly faces up to the „berufundfamilie“ audit.



Finanzierung Financing

Institutionelle Förderung durch Bund und Länder (in Mio. EUR)/ Institutional funding support by the federal government and the federal states (in million EUR)	33,1
eingeworbene Drittmittel/ third party funding	9,3
<i>davon/ including:</i>	
DFG/ German Research Foundation	4,7
Freistaat Sachsen/ State of Saxony	0,9
EU-Programme/ EU-programs	1,4
Bund-Projekte/ Federal Government projects	1,3
Industrie/ industrial contact	0,4
Stiftungen und andere Geldgeber/ Foundations and other donors	0,6

Beschäftigte Personnel

Anzahl Beschäftigte gesamt/ Personnell total: 31.12.2019	602
<i>davon/ including:</i>	
Wissenschaftliches Personal/ scientific staff	314
<i>darunter DoktorandInnen/ including doctoral students</i>	102
Technisches Personal/ technical staff	125
Verwaltungspersonal/ administrative staff	43
StipendiatInnen/ scholarship recipients	44
GastwissenschaftlerInnen/ guest scientists ¹⁾	55
Auszubildende/ apprentices ²⁾	21
zusätzlich betreute Doktor- Diplom- u. Masterarbeiten/ supervised PhD's and undergraduate students without contract	20

¹⁾ Eingebunden in die IFW-Forschung, über Forschungsk Kooperationen finanziert / Integrated in the IFW research, financed by research cooperations

²⁾ 6 verschiedene Ausbildungsberufe sowie Studenten der Ausbildungsakademie / 6 different training occupations and students of the training academy

Kuratorium

Board of trustees

Dr. Babett Gläser

Sächsisches Staatsministerium für Wissenschaft
und Kunst, Saxonian Ministry of Science and Art
Vorsitzende / Chair

Dr. Peter Schroth

Bundesministerium für Bildung und Forschung,
Federal Ministry of Education and Research

Prof. Dr. Gerhard Rödel

Technische Universität Dresden

Prof. Dr. Manfred Hennecke

Berlin

Wissenschaftlicher Beirat

Scientific Advisory Board

Prof. Dr. Maria-Roser Valenti

Goethe-Universität Frankfurt am Main,
Germany
Vorsitzende / Chair

Prof. Dr. Mark Golden

Universiteit van Amsterdam, Netherlands
(from Oct. 1, 2019 on)
Stellvertretender Vorsitzender/ Deputy Chair

Prof. Dr. Robert H. Blick

Universität Hamburg, Germany

Prof. Dr. Sang-Wook Cheong

Rutgers, The State University of New Jersey, USA
(up to Sept. 30, 2019)

Prof. Dr. Andrey Chubukov

University of Minnesota, USA

Prof. Dr. Judith Driscoll

University of Cambridge, United Kingdom
(from Oct. 1, 2019 on)

Prof. Dr. Matthias Göken

Friedrich-Alexander-Universität
Erlangen-Nürnberg, Germany
(up to Sept. 30, 2019)

Prof. Dr. David Johnson

University of Oregon, USA

Prof. Dr. Heinz Neubert

Siemens AG, Germany

Prof. Dr. Nini Pryds

Danmarks Tekniske Universitet, Denmark

Prof. Dr. Roberto De Renzi

Università di Parma, Italy
(from Oct. 1, 2019 on)

Dr. Jüger Rapp

Robert Bosch GmbH, Germany

Prof. Dr. Roberta Sessoli

Università degli Studi di Firenze, Italy
(up to Sept. 30, 2019)

Prof. Dr. Artur Zrenner

Universität Paderborn, Germany
(from Oct. 1, 2019 on)

Publikationen Publications

Im Jahr 2019 haben IFW-Wissenschaftler 399 referierte Zeitschriftenartikel veröffentlicht, eine beträchtliche Anzahl von ihnen in sehr renommierten Zeitschriften.

In 2019, IFW scientists have published 399 refereed journal articles, a considerable number of them in high impact journals.

Eine ausführliche Publikationsliste ist auf unserer Homepage verfügbar:

A detailed list of publications is available on our homepage:

<https://www.ifw-dresden.de/research/publications>

Auszeichnungen Awards

Oliver G. Schmidt

Admission as a new member of the National Academy of Science and Engineering acadtech

Bernd Büchner, Oliver G. Schmidt, Jeroen van den Brink

Highly-Cited Researcher

Julia Linnemann, Alexander Funk, Yang Zhang, Andrei Pavlov, Yevhen Kushnirenko

Tschirnhaus-Medal of the IFW for excellent PhD theses

Andreas Winkler, Melanie Colditz, Stefanie Hartmann, Uhland Weißker

Science4Life Venture Cup innovation prize for promising projects in Life Sciences

Mariana Medina-Sanchez

Best oral presentation award for early career scientists of the 2nd International Conference on Micro/Nano Machines in Harbin, China, "Sperm-based Microbots towards in vivo assisted fertilization and drug delivery"

Josephine Zeisig, Julia Hufenbach, Uta Kühn, Alexander Fröhlich, Jonas Kimme und Verena Kräusel

Best Poster Award of the Materials Week Dresden 2019, awarded by Springer and by the German Society for Materials Science for the contribution "Neuartige drahtförmige Stahllegierungen zum Laserauftrag- und Reparaturschweißen von Werkstählen"

Berufungen Call on Professorships

Guodong Li	Chinese Academy of Sciences, Institute of Physics, Associated Professorship
Jeroen van den Brink	Universität Augsburg, W3 Professorship
Martin Valldor	University of Oslo, Associated Professorship
Christian Heß	Universität Wuppertal, W3 Professorship
Kornelius Nielsch	Universität Augsburg, W3 Professorship

Gemeinsame Berufungen mit dem IFW Joint appointments with IFW

Julia Kristin Hufenbach	Technische Universität Bergakademie Freiberg, Temporary Professorship
Anna Isaeva	Technische Universität Dresden, Junior Professorship

Anna Isaeva (links) wurde gemeinsam mit der TU Dresden auf eine Juniorprofessur berufen. Julia Kristin Hufenbach (rechts) übernahm eine befristete Professur nach Thüringer Modell an der TU Bergakademie Freiberg. *Fotos: Jürgen Lösel*

Anna Isaeva (left) was appointed to a junior professorship together with the TU Dresden. Julia Kristin Hufenbach was appointed to a temporary professorship together with the TU Bergakademie Freiberg in accordance with the Thuringian Model. *Photos: Jürgen Lösel*



Patente Patents

Zum 31. Dezember 2019 hielt das IFW 106 Patente in Deutschland und 88 internationale Patente.
By 31 December 2019, the IFW holds 106 patents in Germany and 88 international patents.

Erteilte Patente Patent grants

DE 10 2015 220 766.8 (11523 DE)

23.05.2019

Verfahren zur Herstellung eines umgeformten Körpers aus vollkristallinen, metastabilen Materialien und umgeformter Körper aus vollkristallinen, metastabilen Materialien

invented by Simon Pauly, Konrad Kosiba, Uta Kühn, Jürgen Eckert

DE 50 2015 009 812.0 (11402 DE)

EP 3 099 785 (11402 GB)

EP 15 703 510.6 (11402 EP)

31.07.2019

Verfahren zur Herstellung der Beweglichkeit von immobilen Zellen

invented by Oliver G. Schmidt

JP 2017-518591 (11414 JP)

11.03.2019

Batterieträger

invented by Markus Herklotz, Jonas Weiß, Lars Giebeler, Michael Knapp

US 15/423,297 (11529 US)

09.04.2019

Asymmetrischer optischer Resonator und optische Vorrichtung, die den asymmetrischen optischen Resonator aufweist

invented by Libo Ma, Oliver G. Schmidt

EP 3 293 290 (11609 FR)

EP 3 293 290 (11609 GB)

EP 3 293 290 (11609 IE)

EP 3 293 290 (11609 NL)

DE 50 2017 002 074.7 (11609 DE)

EP 17 190 645.6 (11609 EP)

21.08.2019

Elektrolyte für die elektrochemische Abscheidung von thermoelektrischen Materialien
invented by Nicolás Pérez Rodríguez, Heike Schlörb, Melanie Mohn, Tom Sieger

DE 60 2014 049 108.1 (11418 DE)

26.06.2019

Capacitor and Process for producing thereof
invented by Daniel Grimm, Oliver G. Schmidt, Ivoyl Koutsaroff, Shoichiro Suzuki, Koichi Banno

DE 10 2016 124 059.1 (11618 DE)

19.12.2019

Vorrichtung für die Mikrofluidik
invented by Andreas Winkler, Stefan Harazim

DE 10 2017 122 657.6 (11717 DE)

04.11.2019

Vorrichtung und Verfahren zur Bestimmung von Eigenschaften leitfähiger oder dielektrischer Schichten
invented by Günter Martin, Hagen Schmidt

DE 10 2018 200 483.8 (11707-F DE)

21.12.2019

Thermoelektrisches Material und Verfahren zur Herstellung eines thermoelektrischen Materials
invented by Gabi Schierning, Felix Thiel, Jochen Friedrich, Christian Reimann, Maximilian Beier

DE 60 2010 051 789.6 (11013 EP/DE)

EP 244 4985 (11013 EP/FR)

11.04.2019

Production method of rare earth magnet
invented by Noritsugu Sakuma, Hidefumi Kishimoto, Akira Kato, Tetsuya Shoji, Dominique Givord, Nora Dempsey, Thomas George Woodcock, Oliver Gutfleisch, Gino Hrkac, Thomas Schreth

DE 10 2012 221 408.9 (11226 DEM)

12.11.2019

Akustische Oberflächenwellenbauelemente mit Interdigitalwandlern und Verfahren zu ihrer Herstellung
invented by Siegfried Menzel, Jürgen Eckert, Henning Turnow

EP 3207552 (11426 EP)

23.01.2019

ZL 201580068012.0 (11426 CN)

13.08.2019

Kompakter Kondensator und Verfahren zu seiner Herstellung
invented by Oliver G. Schmidt

Patentanmeldungen

Priority patent applications

DE 10 2019 106 510.0 (11903 DE)

14.03.2019

Verfahren zur Bestimmung von Eigenschaften von Schichten in Schichtsystemen
invented by Günter Martin, Hagen Schmidt

DE 10 2019 110 748.2 (11906 DE)

25.04.2019

Einrichtung und Verfahren zum Sortieren und Trennen von in Fluiden dispergierten Mikropartikeln und/oder Zellen
invented by Andreas Winkler, Cynthia Richard, Melanie Colditz, Friedrich Striggow, Armaghan Fakhfour

DE 10 2019 116 526.1 (11823 DE)

18.06.2019

Verfahren und Vorrichtung zur Bestimmung der Position von Objekten
invented by Daniil Karnauschenko, Oliver G.

DE 10 2019 116 669.1 (11822 DE)

19.06.2019

Batterie-Teststand
invented by Lars Giebeler, Marek Ulbrich

DE 10 2019 131 153.5 (11921 DE)

19.11.2019

Verfahren zur Optimierung der additiven Herstellung von Bauteilen
invented by Konrad Kosiba

Doktorarbeiten PhD Theses

Cliò Agrapidis	Topologically non-trivial states in one- and quasi-one-dimensional frustrated spin systems, TU Dresden
Victoria Eckert	Wachstumsmechanismen und Oberflächeneigenschaften undotierter und N-dotierter Kohlenstoffnanoröhren, TU Dresden
Benjamin Escher	Einfluss struktureller Heterogenitäten auf die mechanischen Eigenschaften Cu-Zr-basierter metallischer Gläser, TU Dresden
Monica Fernandez Barcia	Sustainable synthesis of FeMn films and fabrication of Fe/Mn-based micromotors, TU Dresden
Alexander Funk	Magnetokalorische Regeneratoren aus $(\text{Mn,Fe})_2(\text{P,Si})$ - und $\text{La}(\text{Fe,Co,Si})_{13}$ -Legierungen, TU Dresden
Rasha Ghunaim	Development of intermetallic filled carbon nanotube sensors for hyperthermia applications, TU Dresden
Erik Haubold	Electronic structure of topological semimetals, TU Dresden
Margarita Iakovleva	Magnetic Resonance Spectroscopy on Low-dimensional and Frustrated Magnets, TU Dresden
Franziska Karnbach	Magnetfeldbasierte Steigerung der Wasserstoffproduktion während der Wasserelektrolyse, TU Dresden
Florian Kiebert	Flüssigkeits- und Partikelmanipulation in mikrofluidischen Oberflächenwellen-Systemen, TU Dresden



Yevhen Kushnirenko	Details of 3D electronic structure of some Fe-based superconductors and their superconducting order parameters, TU Dresden
Julia Linnemann	Elektrochemische Synthese und Umsetzung metallorganischer Ausgangsmaterialien und -beschichtungen für energietechnische Anwendungen, TU Dresden
Andrei Pavlov	Phonon-mediated Casimir effect, TU Dresden
Romy Reinhold	Binäre Kupfer- und Siliciumphosphide und deren Anwendung in elektrochemischen Energiespeichern, TU Dresden
Omar Oday Salman	Selective laser melting of 316L stainless steel and related composites: processing and properties, TU Dresden
Sebastian Schneider	Transmissionselektronenmikroskopische Vermessung nanoskopischer Spintexturen in dünnen Helimagneten, TU Dresden
Maik Scholz	Chemische und thermische Modifizierung von Garnen aus Kohlenstoffnanoröhren, TU Dresden
Pramote Thirathipviwat	Microstructure, lattice strain and mechanical properties of single phase multi-component alloys, TU Dresden
Lei Xu	Ab initio modeling of the electronic structure of d-metal systems and of resonant X-ray scattering responses, TU Dresden
Yang Zhang	Linear and nonlinear response in solids: A density functional based approach, TU Dresden

Diplom- und Masterarbeiten Diploma and Master Theses

Liu Chen	Self-assembly of 3D tubular aqueous bismuth micro-battery, TU Chemnitz
Melanie Colditz	Cell manipulation with acoustofluidics, TU Dresden
Louis-Philip Doctor	New Insight into electronic excitations in metal-phthalocyanines, TU Bergakademie Freiberg
Julia Erben	Herstellung von Titanoxid-Nanoröhrchen in fluoridfreien Elektrolyten, TU Bergakademie Freiberg
Silas Flöter	Disorder in Higher-Order Topological Insulators, TU Dresden

Samuel Froeschke	Synthese und Charakterisierung von WTe_2 -Nanoschichten auf verschiedenen Substraten, TU Bergakademie Freiberg
Max Georgi	Untersuchung der elektronischen Struktur von α -Ruthenium(III)-Chlorid bei Alkalimetallinterkalation mittels Photoelektronenspektroskopie, TU Dresden
Johanna Hartmann	Perzellulosen als Precursoren für sphärische Kohlenstoffpartikel als Elektrodenmaterialien in symmetrischen Superkondensatoren und Metall-Ionen-Batterien, TU Dresden
Florian Jürries	Untersuchung des Einflusses von Cu-Addition auf die Umformbarkeit, magnetischen Eigenschaften und das Gefüge von hartmagnetischen MnAl-C-Legierungen, TU Dresden
Narayan Kunchur	Magneto-transport in $MnBi_2Te_4$ and $MnBi_4Te_7$ nanostructures, TU Dresden/KU Leuven
Patrick Langhelm	Werkstoffentwicklung für den SLM-Prozess – Hochfeste Aluminiumlegierungen für die Automobilindustrie, TU Dresden
Klara Lünser	Einfluss von Gefüge und Orientierung auf den magnetokalorischen Effekt epitaktischer Ni-Mn-Ga-Co-Schichten, TU Dresden
Khan, Mishal	Preparation of shape-tailored porous Au nanowires based on electrodeposition of Au-Cu alloys with view to biosensor applications, TU Dresden
Ramasamy Murugesan	Electronic Structure of Cu ions with trigonal bipyramidal coordination in honeycomb $In_3Cu_2VO_9$, TU Dresden
Martin Otto	Gefügeanalyse der Legierung Ti-5553 hergestellt mittels Selektiven Laserschmelzens, TU Dresden
Qifeng Pan	Numerische Analyse von gekoppelten nichtlinearen Cantilever-Systemen für Sensoranwendungen, Univ. Stuttgart
Felix Pischel	Functionalization of SU8-Tubes for the penetration of cumulus cells by sperm-driven microswimmers, TU Dresden
Aniruddha S. Prasad	Simulation and experimental investigations on coupled micro- and nano-mechanical oscillating beams, TU Dresden/KU Leuven
Jesch, Rebekka	Herstellung und Untersuchung oberflächenmodifizierter Siliziumpartikel zur Anwendung als Anodenmaterial in Lithium-Batterien, TU Dresden
Daniel Scheffler	Herstellung und Charakterisierung von magnetischen MnAl Dünnschichten deponiert durch rf/dc Sputtern, TU Dresden

Alexander Stepanjuga Synthese und Charakterisierung von $(\text{Na,K})(\text{Li,Zn})\text{S}_2$ – Verbindungen,
HTW Dresden

Teresa Tschirner Crystal Hall Effect in RuO_2 , TU Dresden

Stipendien Scholarships

Im Jahr 2019 waren 59 StipendiatInnen am IFW tätig. Darunter waren 7 StipendiatInnen von der Alexander von Humboldt-Stiftung, 13 StipendiatInnen vom Deutschen Akademischen Austauschdienst DAAD und 19 StipendiatInnen vom China Scholarship Council.

In 2019, 59 scholarship holders worked at IFW. Among them were 7 fellows of the Alexander von Humboldt Foundation, 13 fellows of the German Academic Exchange Service DAAD and 19 fellows of the China Scholarship Council.

Wissenschaftliche Konferenzen Scientific Conferences

March 28-29 Joint workshop of BAM Berlin and IFW Dresden, IFW Dresden

March 28-29 International Workshop „Quantum Dynamics, Transport, and Exotic Orders: Strolling among Spins and Strong Correlations“, IFW Dresden

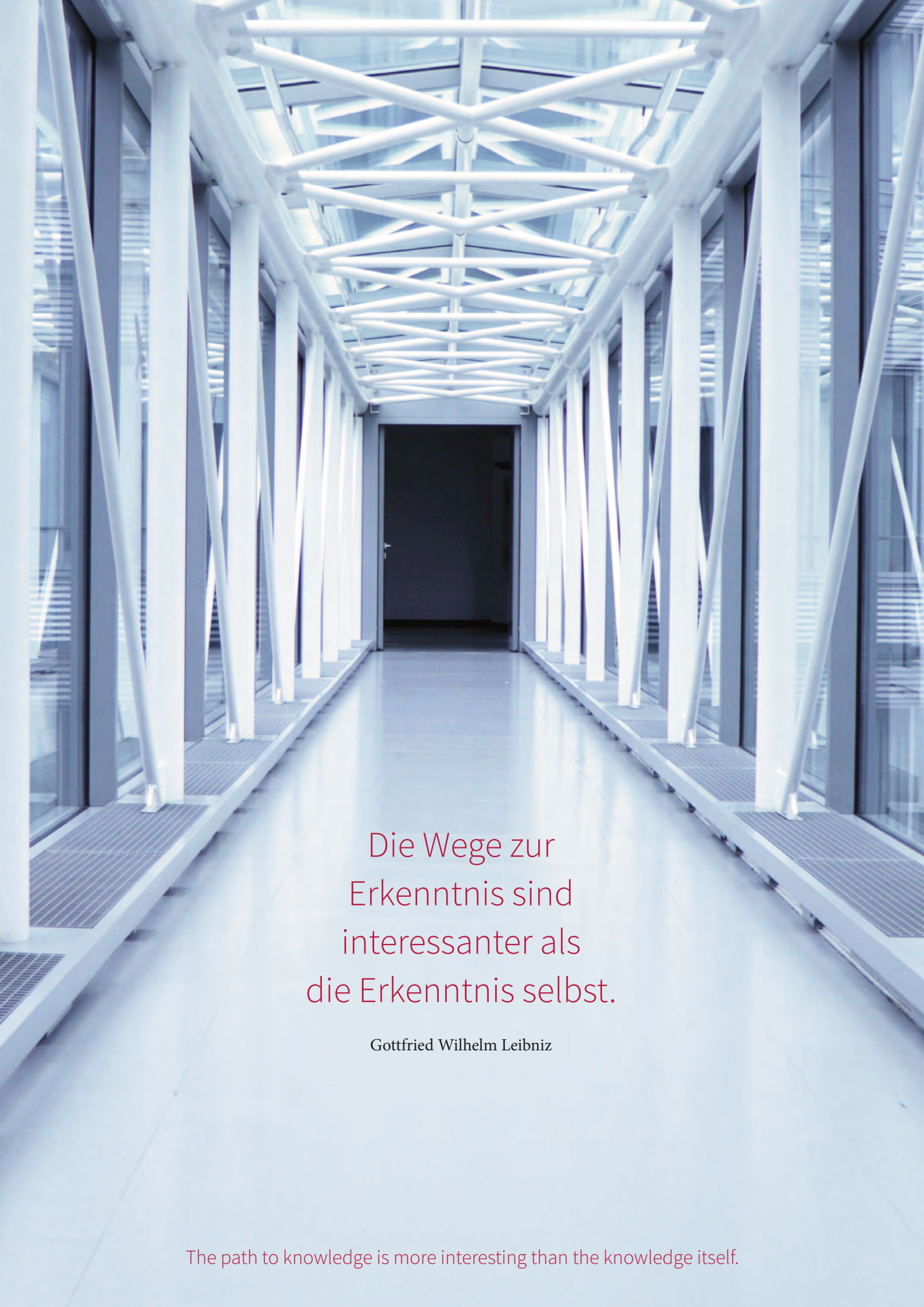
May 20-21 International Workshop „Topology meets materials – Weizmann meets Dresden“, IFW Dresden

September 13-20 Summer School Spectroelectrochemistry, IFW Dresden

September 15-20 ECASIA19: 18th European Conference on Applications of Surface and Interface Analysis

September 15-20 SAW Symposium, Westin Bellevue Dresden

September 25-27 Annual IFW Summer School for PhD students in Szczecin, Poland



Die Wege zur
Erkenntnis sind
interessanter als
die Erkenntnis selbst.

Gottfried Wilhelm Leibniz

The path to knowledge is more interesting than the knowledge itself.

Leibniz Institute for Solid State and Materials Research Dresden

Board of Trustees

Head: Dr. Babet Gläser, Sächsisches Staatsministerium für Wissenschaft, Kultur und Tourismus

Scientific Advisory Board

Head:
Prof. Dr. Maria-Rosler-Valenti,
J.-W. Goethe-Universität Frankfurt

Executive Board

Scientific Director
Prof. Dr. Bernd Büchner
Assistant: Dr. Carola Langer
Secr.: Katja Schmiedel

Administrative Director
Dr. Doreen Kirmse
Secr.: Franziska Böttger

Public Relation, Media
Dr. Carola Langer,
Patricia Bäuchler

Safety Officer
Uwe Schmiel

Knowledge and technology transfer
Dr. Uwe Siegel

Internal Auditor
Stefan Leipnitz

Controlling
Dirk Rehn

Institute for Solid State Research

Prof. Dr. Bernd Büchner
Secr.: Kerstin Höllerer,
Katja Schmiedel

Institute for Metallic Materials

Prof. Dr. Kornelius Nielsch
Secr.: Ines Firlle,
Agata Cervinska

Institute for Complex Materials

Prof. Dr. Bernd Büchner
(temp.)
Secr.: Brit Präbber-Wüstling

Institute for Integrative Nanosciences

Prof. Dr. Prof. h. c. Oliver G. Schmidt
Secr.: Kristina Krummer,
Martina Javorcka

Institute for Theoretical Solid State Physics

Prof. Dr. Jeroen van den Brink
Secr.: Grit Rötzer

Research Technology

Prof. Dr. Dirk Lindackers
Secr.: Nicole Büttner

Administration

Friederike Jaeger
Secr.: Katja Steinbrink

Surface dynamics
Dr. Hagen Schmidt

Transport and scanning probe microscopy
Dr. Christian Hemker-Heß¹

Dr. Joseph Dufouleur
Dr. Thomas Mühl

Thermoelectric materials and devices
Dr. Gabi Schierning¹

Quantum materials and devices
Dr. Andy Thomas

Functional magnetic films
Dr. Sebastian Fähler

Solidification processes and complex structures
Dr. Ivan Kaban

Magnetic composites and applications
Dr. Maria Krautz

Micro- and nanostructures
Dr. Thomas Gemming

Rolled-up photonics
Dr. Libo Ma

Integrated nanophotonics
Prof. Dr. Fei Ding¹

Micro- and nanobiomedical engineering
Dr. Mariana Medina-Sanchez¹

Theoretical solid state physics
Prof. Dr. Jeroen van den Brink

Quantum chemistry
Dr. Liviu Hozoi

Topological states of interacting matter
Dr. Ion Cosma Fulga⁵

Electrical engineering and electronics
Karsten Peukert

Mechanical engineering
Dr. Ralf Voigtländer

Information technologies
Thomas Fichte

Finances
Martina Schmidt

Human resources
Yvonne Messerschmidt

Purchase and disposal
Kristin Schwenske

Chemistry of nanomaterials
Dr. Alexey Popov¹

Dr. Silke Hampel
Dr. Yulia Krupskaya

Magnetic materials
Dr. Thomas G. Woodcock

Functional oxide layers and superconductors
Dr. Ruben Hühne

Nanoscale electrodeposition
Dr. Karin Leistner

Electrochemical energy storage
Dr. Daria Mikhailova

Alloy design and processing
Prof. Dr. Julia Hufenbach⁷

Dr. Uta Kühn

Compliant magneto-sensory systems
Dr. Daniil Karnausenko

Numerical solid state physics and simulation
PD Dr. Manuel Richter

Computational methods for correlated materials
Dr. Oleg Janson³

Library
Jana Sonnenstuhl

Facility Management
Werner Effenberg

Funding and Cooperation
Carsten Glück

Electrical engineering and electronics
Karsten Peukert

Mechanical engineering
Dr. Ralf Voigtländer

Information technologies
Thomas Fichte

Magnetic properties
Dr. Vladislav Kataev

Dr. Hans-Joachim Grafe
Dr. Anja Wolter-Giraud

Metal physics
Prof. Dr. Jens Freudenberger

Magnetic microstructures
Prof. Dr. Rudolf Schäfer

Electrochemical energy storage
Dr. Daria Mikhailova

Alloy design and processing
Prof. Dr. Julia Hufenbach⁷

Dr. Uta Kühn

Compliant magneto-sensory systems
Dr. Daniil Karnausenko

Numerical solid state physics and simulation
PD Dr. Manuel Richter

Computational methods for correlated materials
Dr. Oleg Janson³

Library
Jana Sonnenstuhl

Facility Management
Werner Effenberg

Funding and Cooperation
Carsten Glück

Electrical engineering and electronics
Karsten Peukert

Mechanical engineering
Dr. Ralf Voigtländer

Information technologies
Thomas Fichte

Synchrotron Methods
Dr. Sergey Borisenko
Dr. Alexander Fedorov⁴

Crystal growth and synthesis of inorganic materials
Dr. Sabine Würmehl
Dr. Saicharan Aswartham
Dr. Silvia Seiro
Prof. Dr. Anna Isaeva⁶

Topological Superconductivity in Complex Quantum Matter
Dr. Nicola Poccia

PPMS Measurement Lab
Dr. Nicolas Perez Rodriguez

Micro System Technology
Dr. Heiko Reith

Alloy design and processing
Prof. Dr. Julia Hufenbach⁷

Dr. Uta Kühn

Compliant magneto-sensory systems
Dr. Daniil Karnausenko

Numerical solid state physics and simulation
PD Dr. Manuel Richter

Computational methods for correlated materials
Dr. Oleg Janson³

Library
Jana Sonnenstuhl

Facility Management
Werner Effenberg

Funding and Cooperation
Carsten Glück

Electrical engineering and electronics
Karsten Peukert

Mechanical engineering
Dr. Ralf Voigtländer

Information technologies
Thomas Fichte

- ¹ ERC Group
- ² Emmy Noether Research Group
- ³ Leibniz Junior Research Group
- ⁴ Joint Junior Group with HZB
- ⁵ IFW Junior Research Group
- ⁶ Joint Junior Professorship with TU Dresden
- ⁷ Joint Professorship with TU Bergakademie Freiberg

Councils and Representatives

Labour Council
Head: Mario Bloeck

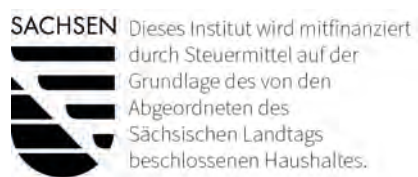
Equal Opportunities Officer
Dr. Anke Kirchner

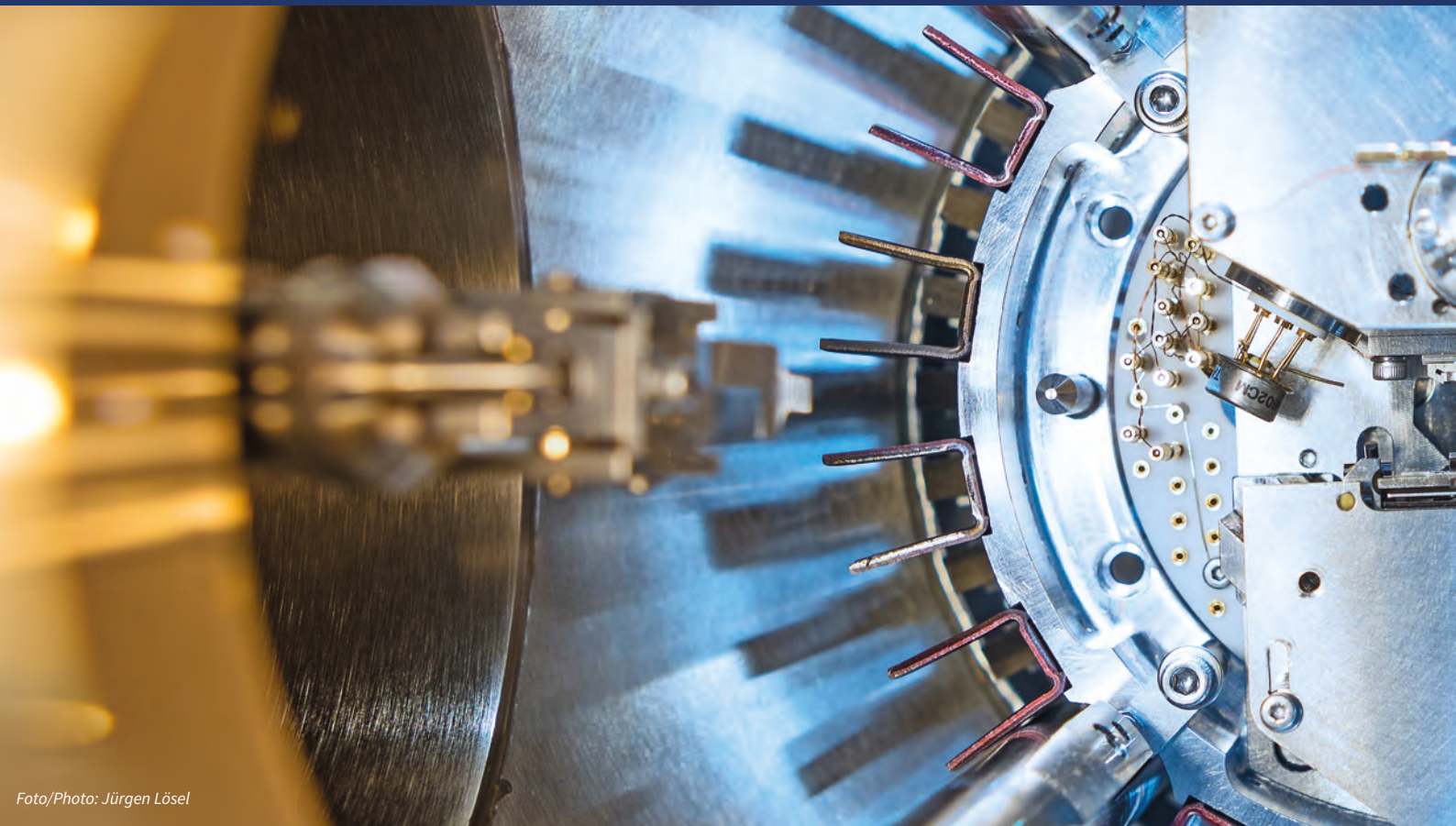
Representative for disabled employees
Dr. Hartmut Siegel

Ombudsperson
Prof. Dr. Rudolf Schäfer

Data Security Officer
Kristin Beyer

Scientific Technical Council
Head: Dr. Ulrich Rößler





Foto/Photo: Jürgen Lösel